A&A 672, A130 (2023)
https://doi.org/10.1051/0004-6361/202243435


Astronomy & Astrophysics

# Time variability of the core-shift effect in the blazar 3C 454.3⋆

Wara Chamani[1,2], Tuomas Savolainen[1,2,3], Eduardo Ros[3], Yuri Y. Kovalev[4,5,3], Kaj Wiik[6], Anne Lähteenmäki[1,2], Merja Tornikoski[1], and Joni Tammi[1]

[1] Aalto University Metsähovi Radio Observatory, Metsähovintie 114, 02540 Kylmälä, Finland
e-mail: wara.chamani@aalto.fi
[2] Aalto University Department of Electronics and Nanoengineering, PO Box 15500, 00076 Aalto, Finland
[3] Max-Planck-Institut für Radioastronomie, Auf dem Hügel 69, 53121 Bonn, Germany
[4] Lebedev Physical Institute of the Russian Academy of Sciences, Leninsky prospekt 53, 119991 Moscow, Russia
[5] Moscow Institute of Physics and Technology, Institutsky per. 9, Dolgoprudny, Moscow region 141700, Russia
[6] Department of Physics and Astronomy, 20014 University of Turku, Finland

Received 28 February 2022 / Accepted 25 November 2022

**ABSTRACT**

Measuring and inferring the key physical parameters of jets in active galactic nuclei (AGN) requires high-resolution very long baseline interferometry (VLBI) observations. Using VLBI to measure a core-shift effect is a common way of obtaining estimates of the jet magnetic field strength, a key parameter for understanding jet physics. The VLBI core is typically identified as the bright feature at the upstream end of the jet, and the position of this feature changes with the observed frequency, $r_{\rm core} \propto \nu^{-1/k_r}$. Due to the variable nature of AGN, flares can cause variability of the measured core shift. In this work, we investigated the time variability of the core-shift effect in the luminous blazar 3C 454.3. We employed a self-referencing analysis of multi-frequency (5, 8, 15, 22−24, and 43 GHz) Very Long Baseline Array (VLBA) data covering 19 epochs from 2005 to 2010. We found significant core-shift variability ranging from 0.27 to 0.86 milliarcsec between 5 GHz and 43 GHz. These results confirm the core-shift variability phenomenon observed previously. Furthermore, we also found time variability of the core-shift index, $k_r$, which was typically below one, with an average value of $0.85 \pm 0.08$ and a standard deviation of 0.30. Values of $k_r$ below one were found during flaring and quiescent states. Our results indicate that the commonly assumed conical jet shape and equipartition conditions do not always hold simultaneously. Even so, these conditions are typically assumed when deriving magnetic field strengths from core-shift measurements, which can lead to unreliable results if $k_r$ significantly deviates from unity. Therefore, it is necessary to verify that $k_r = 1$ actually holds before using core-shift measurements and the equipartition assumption to derive physical conditions in the jets. When $k_r = 1$ epochs are selected in the case of 3C 454.3, the magnetic field estimates are consistent, even though the core shift varies significantly with time. Subsequently, we estimated the magnetic flux in the jet of 3C 454.3 and found that the source is in the magnetically arrested disc state, which agrees with earlier studies. Finally, we found a good correlation of the core position with the core flux density, $r_{\rm core} \propto S_{\rm core}^{0.7}$, which is consistent with increased particle density during the flares.

**Key words.** galaxies: active – galaxies: jets – galaxies: magnetic fields – quasars: individual: 3C454.3 – techniques: high angular resolution

## 1. Introduction

The effect known as core shift is an observational feature of synchrotron-emitting relativistic jets in active galactic nuclei (AGN). Core shift is the change in the radio core's distance from the central engine as a function of frequency. The first observations of the phenomenon were reported by Marcaide & Shapiro (1984), and since then it has been detected often in multi-frequency very long baseline interferometry (VLBI) images of compact extragalactic sources (e.g. Kovalev et al. 2008; O'Sullivan & Gabuzda 2009; Sokolovsky et al. 2011; Hada et al. 2011; Pushkarev et al. 2012; Fromm et al. 2015; Lisakov et al. 2017). The physical nature of the VLBI core is still a matter of debate, and it has been suggested that at least at millimetre wavelengths it might be due to a standing shock in the jet (Marscher 2010). In such a case one would not expect to see a significant frequency dependence of the core position. On the other hand, following the prediction of Blandford & Königl (1979, hereafter BK79), the core is the region where the jet becomes self-absorbed at a given frequency $\nu_{\rm obs}$ (i.e. the optical depth to synchrotron self-absorption, $\tau$, becomes approximately one). In the BK79 model the core's position along the jet, $r_{\rm core}$, varies with frequency as $r_{\rm core} \propto \nu_{\rm obs}^{-1/k_r}$ because of the magnetic field strength and particle density gradients in the jet. The BK79 model assumes a freely expanding, supersonic, narrow, and conical jet with a constant half-opening angle, $\phi$, and with a constant Lorentz factor $\Gamma$. The magnetic field strength $B$ and particle number density $N$ within the radiating cores are assumed to be uniform and constant. Both decay with the distance $r$ along the jet as $B = B_1\,(r_1/r)^m$ and $N = N_1\,(r_1/r)^n$, where $B_1$ and $N_1$ are the values at the distance of $r_1 = 1$ pc from the apex of the jet. Assuming energy equipartition between particle and magnetic energy densities, the indices should be scaled such that $n = 2m$. Choosing $m = 1$ and $n = 2$ results in $k_r = 1$ irrespective of the optically thin spectral index of the emission (Königl 1981; Lobanov 1998). Based on these previous models, a recent study further showed that in microquasars with

⋆ VLBI maps (FITS) are only available at the CDS via anonymous ftp to cdsarc.cds.unistra.fr (130.79.128.5) or via https://cdsarc.cds.unistra.fr/viz-bin/cat/J/A+A/672/A130

moderately relativistic flow speeds and significant jet opening angles the core position can also vary with the inclination angle and different magnetic field configurations (Sharma et al. 2022).

Several studies have confirmed $r_{\rm core} \propto \nu_{\rm obs}^{-1}$ (Lobanov 1998; Hirotani 2005; O'Sullivan & Gabuzda 2009; Fromm et al. 2010, 2013b, 2015; Sokolovsky et al. 2011; Hada et al. 2011; Mohan et al. 2015; Lisakov et al. 2017; Pushkarev et al. 2018) and the amount of core shift together with the equipartition assumption has been frequently used to infer jet magnetic field strengths (e.g. Pushkarev et al. 2012; Voitsik et al. 2018; Plavin et al. 2019b, hereafter PL19; Chamani et al. 2021). However, there is very little knowledge of the stability of the index $k_r$ over time or how this affects the inferred magnetic field strength. Knowing the jet magnetic field strength is important since it is one of the key parameters to test the results from the general relativistic magnetohydrodynamic (GRMHD) simulations on formation and collimation of jets (e.g. Tchekhovskoy 2015, with references therein). For example, these works show that when enough magnetic flux is available for accretion, the magnetic flux surrounding the supermassive black hole may reach a saturation point and a magnetically arrested disc (MAD) develops (Narayan et al. 2003). MAD accretion behaves very differently from the standard weakly magnetized disc, and it is able to launch very powerful relativistic jets in simulations (Tchekhovskoy et al. 2011; McKinney et al. 2012). Zamaninasab et al. (2014) used core shift measurements to infer magnetic fluxes in 76 jets in blazars and radio galaxies from the MOJAVE survey, and they concluded that the high-power jets indeed appear to result from MAD accretion. Core-shift-inferred magnetic fields can therefore play a major role in our understanding of accretion and ejection in AGN. Therefore, it is essential to investigate how reliable these measurements are.

A number of previous works have reported core shift and magnetic field measurements in a diversity of sources (e.g. O'Sullivan & Gabuzda 2009; Sokolovsky et al. 2011; Pushkarev et al. 2012); however, these studies were limited to single-epoch observations. Recently, a compelling multi-epoch investigation of the core shift on an extensive AGN data set having more than ten observing epochs has been reported by PL19. Their results exhibit a significant variability of the core shift up to 1 mas for the frequency pair of 2 GHz and 8 GHz on timescales of years. Although PL19 results show for the first time substantial fluctuation of the core position, dedicated observations at three or more frequencies are necessary to understand the potential variability of the functional form of the core shift, which could provide information about deviations from the equipartition or effects of the propagating flares on the physical conditions in the jet. Ideally, such investigations should be done with multi-frequency and multi-epoch observations of a representative sample of sources. Examples of such monitoring efforts targeting individual sources include 3C 273 (Savolainen et al. 2008b), 3C 345 (Lobanov & Zensus 1999), CTA 102 (Fromm et al. 2013b), and PKS 2233-148 (Pushkarev et al. 2018).

Due to the variable nature of AGN, strong outbursts could potentially cause time variability of the core-shift effect and possibly disturb the relation $r_{\rm core} \propto \nu^{-1}$ (see e.g. Kovalev et al. 2008; Fromm et al. 2013b, 2015; Niinuma et al. 2015; Hodgson et al. 2017; Lisakov et al. 2017; PL19). Consequently, magnetic field strength estimations and astrometry could be significantly affected. Thus, because blazars are conspicuous flaring sources, they are attractive targets to study the variability of the core shift and explore the stability of the magnetic field strength.

An intriguing study case is the very luminous and variable flat-spectrum radio quasar 3C 454.3 (B 2251+158, 4C +15.76), also known as the *Crazy Diamond*, located at redshift $z = 0.859$ (Jackson & Browne 1991). Blazar 3C454.3 emits a powerful relativistic jet pointing towards us at a small viewing angle. It has been catalogued as one of the most luminous astronomical objects and the brightest extragalactic gamma-ray source. The source exhibits typical flat-spectrum radio-loud quasar (FSRQ) features, such as non-thermal emission and variability across the whole electromagnetic spectrum. Many multi-wavelength observing campaigns of 3C 454.3 ranging from radio to gamma rays have been performed over the years. The source started an extraordinary flaring behaviour in early 2005 with the first strong peak in 2006, the second peak in the mid-2008, and the largest peak in 2010, as seen in the Metsähovi Radio Observatory single-dish observations at 37 GHz (see Fig. 9) and in the 15 GHz Owens Valley Radio Telescope (OVRO) observations (see e.g. Sarkar et al. 2019). This period corresponds to the major multi-wavelength (radio, millimetre, optical, X-ray and gamma-ray) flaring events during 2005 and 2006 (e.g. Remillard 2005; Giommi et al. 2006; Villata et al. 2006; Pian et al. 2006; Jorstad et al. 2010), and in 2007−2010 (e.g. Ghisellini et al. 2007; Raiteri et al. 2008, 2011; Vercellone et al. 2009, 2010; Donnarumma et al. 2009; Abdo et al. 2009; Jorstad et al. 2010, 2013) with extraordinarily bright gamma-ray flares in early December 2009 (Bonnoli et al. 2011; Pacciani et al. 2010) and in November 2010 (Abdo et al. 2011). 3C 454.3 continuously flared until 2011, and then entered a quiescent state in 2012, which lasted until 2014. Since 2014, small flaring events have been registered although they are not strong compared to the period prior to 2012 (Sarkar et al. 2019).

Recent studies based on multi-frequency flux density monitoring observations and the motion of superluminal components observed in 3C 454.3 have suggested the existence of a supermassive binary black hole system in this source (Volvach et al. 2021; Qian et al. 2021). Volvach et al. (2021) performed harmonic analysis using radio, optical, and gamma-ray flux density monitoring covering a period from 1966 to 2020 to establish the precession and orbital periods for what they argue correspond to a close black hole binary system. They report a possible period of 14 yr based on the light curve analysis. In another study, a double precessing jet scenario has been proposed for 3C454.3, where two groups of superluminal knots are ejected at different directions that, according to the authors' model, originate from two different jets precessing with the same period of 10.5 yr (Qian et al. 2021, with references therein). The physical origin of the observed variability in 3C 454.3 might be explained in the context of the precessing jet scenario as suggested by Volvach et al. (2021) and Qian et al. (2021). However, other mechanisms, such as fluctuations in the magnetic field in the inner disc, variations in the accretion flow, or the development of shocks or instabilities in the jet can also be potential origins of its variability.

In view of its variable nature, 3C 454.3 is an excellent target for studying whether the core-shift effect is also variable in this source. Previously, Pushkarev et al. (2012) and Kutkin et al. (2014) reported core-shift measurements of the jet in 3C 454.3 at a total of three epochs, but only the measurement in Kutkin et al. (2014) had enough frequencies to measure $k_r$. Additionally, radio light curve-based core-shift estimations were reported by Mohan et al. (2015). However, these data were not enough to study the time variability of the core shift and $k_r$.

In this paper we present results from three multi-wavelength Very Long Baseline Array (VLBA) monitoring programmes of 3C 454.3 that we carried out between 2005 and 2010, as well as

archival VLBA data. With this rich data set, we aim to test how stable the core-shift magnitude, the $k_r$ index, and the inferred magnetic field strengths are over time in 3C 454.3. We measure the frequency-dependent shifts of the core position in a frequency range spanning from 5 GHz to 43 GHz along with the core spectrum and core-shift vector directions. We present a direct measurement of the time variability of the $k_r$ index for the first time. We study how the variable source flux density affects the core shift and investigate the role played by the flaring events. Using the core-shift measurements, the jet's magnetic field strength at 1 pc is estimated for $k_r = 1$ and $k_r \neq 1$ cases. We also test whether the source is in a MAD state during the observed epochs. Finally, we explore the connection of core-shift magnitude and $k_r$ with core flux densities, the relation of $k_r$ with the jet position angle, and the possible correlation of magnetic field strength at 1 pc with core-flux density when $k_r = 1$.

The paper is structured as follows. In Sect. 2 we describe the observations and data calibration; in Sect. 3 we describe the analysis method; and in Sect. 4 we present our results. The discussion and the summary are in Sects. 5 and 6, respectively. We adopt a cosmology with $\Omega_m = 0.27$, $\Omega_\Lambda = 0.73$ and $H_0 = 71\,\mathrm{km\,s^{-1}\,Mpc^{-1}}$ (Komatsu et al. 2009). The source is at a luminosity distance of 5.49 Gpc; at this distance the scale is 7.70 pc mas$^{-1}$. Throughout the paper the spectral index $\alpha$ is defined as $S_\nu \propto \nu^\alpha$, where $\nu$ is the observed frequency and $S_\nu$ is the flux density.

## 2. Observations and data calibration

### 2.1. Observations

#### 2.1.1. Very Long Baseline Array

We analysed a total of 19 epochs of VLBA data dating from 2005 to 2010 and comprising five different frequency bands: $C$ band (5 GHz), $X$ band (8 GHz), $K_U$ band (15 GHz; hereafter $U$ band), $K$ band (22−24 GHz), and $Q$ band (43 GHz). These observations include both our own multi-frequency monitoring programmes[1] and archival data[2]. Table 1 lists the data with all the epochs and frequencies used in this work. All ten VLBA antennas were scheduled at all the epochs, and any antennas that were taken out of the observation for any reason are given in the table.

The multi-frequency VLBA observations were quasi-simultaneous (i.e. all the bands were observed in every run). Individual 4−6 min scans at different bands were interleaved in order to maximize the $(u, v)$ coverage. The observing runs in the programmes BS157 and BW086 lasted for 10 h each and included CTA 102 and 1749+096 as calibrators for bandpass, polarization leakage, and absolute EVPA. In BS157 the total integration time per epoch on 3C 454.3 was 49 min at $C$, $X$, and $U$ bands; 68 min at $K$ band and; 89 min at $Q$ band. In BW086, more time was spent on CTA 102 and the total integration times on 3C 454.3 were 36 min at $C$, $X$, and $U$ bands; 40 min at $K$ band; and 54 min at $Q$ band. The recording was made with dual circular polarization, 4 × 8 MHz sub-bands (IFs) per polarization, and two-bit digitization, which gave a total recording rate of 256 Mbps. Standard frequency set-ups for continuum observations were used, except for the $X$ band, which had the sub-bands spread across the 500 MHz filter in order to facilitate a Faraday rotation measurement. The BS157 and BW086 programmes also included observations at 86 GHz, but since the data quality at this band is highly variable due to tropospheric phase fluctuations and antenna pointing issues, and since 86 GHz was not observed in S2087, we do not include these data in the current analysis.

In the programme S2087, 8 h observing sessions were used with BL Lac scheduled as a calibrator. The total integration times on 3C 454.3 ranged from 45 min at $C$ and $X$ bands to 82 min at $Q$ band. The recording set-up was again dual circular polarization, 4 × 8 MHz sub-bands per polarization, and two-bit digitization. The $K$-band centre frequency was moved to 23.8 GHz, away from the waterline, in order to improve the continuum sensitivity. Data from all three programmes were correlated at the VLBA correlator in Socorro.

Parts of the data from these three programmes have been published earlier: Zamaninasab et al. (2013) presented multi-frequency VLBA polarimetry analysis of 3C 454.3 based observations made on 2005 May 19 and 2009 September 22, and Fromm et al. (2013a,b, 2015) analysed the kinematics, spectra, and core-shift properties of the calibrator CTA 102 based on the data taken between 2005 May 19 and 2007 April 26.

**Table 1.** VLBA observations of 3C 454.3 used in this work.

| Epoch | Date | Frequency-bands (GHz) | Project code |
|---|---|---|---|
| 1 | 2005-05-19 | $C, X, U, K, Q$ | BS157A |
| 2 | 2005-07-14 | $C, X, U, K, Q$ | BS157B |
| 3 | 2005-09-01 | $C, X, U, K, Q$ | BS157C |
| 4 | 2005-12-04 [(1)] | $C, X, U, K, Q$ | BS157D |
| 5 | 2006-08-03 [(2)] | $C, X, U, K, Q$ | BW086A |
| 6 | 2006-10-02 [(3)] | $C, X, U, K, Q$ | BW086B |
| 7 | 2006-12-04 | $C, X, U, K, Q$ | BW086C |
| 8 | 2007-01-26 | $C, X, U, K, Q$ | BW086D |
| 9 | 2007-04-26 | $C, X, U, K, Q$ | BW086E |
| 10 | 2007-06-16 | $C, X, U, K, Q$ | BW086F |
| 11 | 2007-07-25 [(4)] | $C, X, U, K, Q$ | BW086G |
| 12 | 2007-09-13 [(5)] | $C, X, U, K, Q$ | BW086H |
| 13 | 2008-01-03 [(6)] | $C, X, U, K, Q$ | BW086I |
| 14 | 2008-12-07 | $C, X$ [(*)], $U, K$ [(*)], $Q$ | BO033 |
| 15 | 2009-09-22 | $C, X, U, K, Q$ | S2087BA |
| 16 | 2009-10-22 | $C, X, U, K, Q$ | S2087BB |
| 17 | 2009-12-03 | $C, X, U, K, Q$ | S2087BC |
| 18 | 2010-01-18 [(7)] | $C, X, U, K, Q$ | S2087BD |
| 19 | 2010-02-21 | $C, X, U, K, Q$ | S2087BE |

**Notes.** [(1)]Missing antenna(s): Brewster. [(2)]Missing antenna(s): Mauna Kea. [(3)]Missing antenna(s): Brewster missing for half the observation, due to a focus-rotation mount failure. [(4)]Missing antenna(s): Kitt Peak. [(5)]Missing antenna(s): Hancock and St. Croix. [(6)]Missing antenna(s): Hancock and St. Croix; Brewster missing for half the observation, due to snow problems. [(7)]Missing antenna(s): Hancock. [(*)]$X$-band is split into lower (Xl: 7.9 GHz) and higher (Xh: 8.9 GHz). [(**)]$K$-band is split into lower (Kl: 21.8 GHz) and higher (Kh: 24 GHz).

[1] The first of these programmes (BS157; PI T. Savolainen) was triggered by the major multi-wavelength flaring event in May 2005 (Villata et al. 2006). The second programme (BW086; PI K. Wiik) was a continuation of the monitoring started with BS157. The third programme (S2087; PI Y. Y. Kovalev) was triggered by the *Fermi*-LAT detected $\gamma$-ray flare in September 2009. The last monitoring also covered the large $\gamma$-ray outburst of December 2009 (Ackermann et al. 2010).

[2] Public data from the project BO033 (PI S. P. O'Sullivan) was downloaded from the NRAO archive.

#### 2.1.2. Metsähovi Radio Observatory total flux density monitoring

The 37 GHz observations were made with the 13.7 m diameter Metsähovi radio telescope. A typical integration time to obtain one flux density data point is between 1200 and 1400 s. The detection limit of the telescope at 37 GHz is of the order of 0.2 Jy under optimal conditions. Data points with a signal-to-noise ratio <4 are handled as non-detections.

The flux density scale is set by observations of DR 21. Sources NGC 7027, 3C 274 and 3C 84 are used as secondary calibrators. A detailed description of the data reduction and analysis is given in Teräsranta et al. (1998). The error estimate in the flux density includes the contribution from the measurement rms and the uncertainty of the absolute calibration.

In our study period from 2005 to 2010, 3C 454.3 went through multiple large outbursts which are clearly visible in the 37 GHz flux density curve shown in the top panel of Fig. 9. These outbursts peaked in early 2006, mid-2008, and early 2010. Furthermore, our VLBA observation epochs (indicated by red arrows) coincide with the different phases of these flares. These include the strong rising flare from 2005 May 19 to the short-lived plateau of 2005 December 04, and the transition from a quiescent phase from 2006 August 03 to the formation of the moderate flare in 2008 January 03. The post-flare of 2008 coincides with our VLBA data in 2008 December 07, and the rising part of the major flare in 2009−2010 includes the epochs from 2009 September 22 to 2010 February 21.

### 2.2. Calibration and imaging of the VLBA data

We calibrated the VLBA data using standard methods implemented in the Astronomical Image Processing System (AIPS) software package (Greisen 2003). The procedure followed that described in Lister et al. (2009) except that we typically did not use pulse calibration tones to align the phases across the IFs since the pulse calibration phases often showed unexpected jumps that may be related to the frequent band changes in our observing schedules. Instead, we performed fringe fitting of a single scan of a bright source, either a calibrator or the target itself, and used the results of the global solution to correct single-band delays and align the phases across the IFs. We also always carried out the full global fringe fitting of the whole observation solving for delays, rates, and phases with solution intervals roughly set according to the expected coherence times at the individual bands. Atmospheric opacity correction of the a priori visibility amplitudes was performed for the data taken at $U$, $K$ and $Q$ bands. We note that the MOJAVE team calibrated and imaged a significant fraction of our $U$-band observations as a part of their effort to image archival VLBA data in order to increase the temporal sampling of the MOJAVE programme sources (Lister et al. 2018). If already processed $U$-band data was available from the MOJAVE archive[3], it was used instead of re-doing the calibration.

Imaging (using the standard CLEAN algorithm) and self-calibration (of both amplitudes and phases) of the VLBA data sets were performed with the DIFMAP package (Shepherd 1997). After an initial round of imaging and self-calibration, any significant antenna-based gain errors were identified and a single correction factor per antenna per experiment was applied in AIPS, if necessary. Then a new round of imaging and self-calibration was performed in DIFMAP, this time normalizing the amplitude self-calibration solutions to unity in order to prevent the flux scale from wandering. The resulting amplitude calibration accuracy is estimated to be generally ∼5% at $C$, $X$, and $U$ bands and $\lesssim$10% at $K$ and $Q$ bands in accordance with previous studies (Savolainen et al. 2008a; Sokolovsky et al. 2011; Lister et al. 2018). We used multiple visibility weighting schemes in imaging, going from super-uniform to uniform and finally to natural weighting as the model improved. The final set of CLEAN images was produced with natural weighting; an example of a set of multi-frequency images at one epoch is shown in Fig. 1. The images for all the epochs are presented in Appendix E.

We note the presence of the arc-like structure ∼2 mas downstream of the core. This feature was previously reported by Britzen et al. (2013) and Zamaninasab et al. (2013). The latter authors modelled the structure as a shock wave and showed that the structure exhibits a frequency-stratification in its thickness that follows the expectation for a thin particle acceleration layer, such as a shock wave, from which the accelerated electrons are advected away, losing their energy to synchrotron radiation. The arc is visible in our VLBA images mostly at 15 GHz and 22−24 GHz (until late 2009). At 43 GHz, a partial arc, where the southern side is brighter than the northern one, is visible until mid-2007.

We note here that we dropped epoch 5 (2006 August 03) from further analysis because Mauna Kea, the antenna that gives the longest baselines, did not take part in the observation (see Table 1). However, the images are still presented in Appendix E. The core-shift measurement for epoch 13 (2008 January 03) is still presented but was dropped from the subsequent analysis. There are several missing antennas at this epoch (Hancock, St. Croix, Brewster partly), which results in a poor $(u, v)$ coverage and a degraded resolution such that the core cannot be well resolved at the low frequencies. This leads to ambiguities and a very large core-shift value that is unlikely to be real. Epochs 4, 6, 11, and 18 also had one failed antenna (at least partially) and epoch 12 had two failed antennas, but we kept these data in the analysis since their core-shift measurements did not indicate serious issues. However, one should keep in mind that the $(u, v)$ coverage is degraded at these epochs.

## 3. Data analysis

### 3.1. 2D cross-correlation of the images

In order to measure the core shift, it is necessary to first align the images made at different frequencies. This is non-trivial since the absolute source positions are lost in the phase self-calibration procedure during imaging. 3C 454.3 exhibits an extended parsec-scale jet structure at all the observed frequencies (Fig. 1). The extended structure allows us to align the images by matching the optically thin parts of the jets that are assumed to have frequency-independent structures. We do this by cross-correlating the optically thin jet regions in the CLEAN images at adjacent frequencies. The 2D cross-correlation technique has been widely used to align multi-frequency VLBI images (e.g. Walker et al. 2000; Kovalev et al. 2008; Croke & Gabuzda 2008; O'Sullivan & Gabuzda 2009; Hovatta et al. 2012; Pushkarev et al. 2012; Kutkin et al. 2014; Kravchenko et al. 2016; PL19; Chamani et al. 2021).

In order to apply the image cross-correlation analysis, we first created CLEAN images at the different frequency pairs with a pixel size of 1/20 of the minor axis of the beam of the higher frequency image. The pair of images were then convolved with

[3] https://www.cv.nrao.edu/MOJAVE/

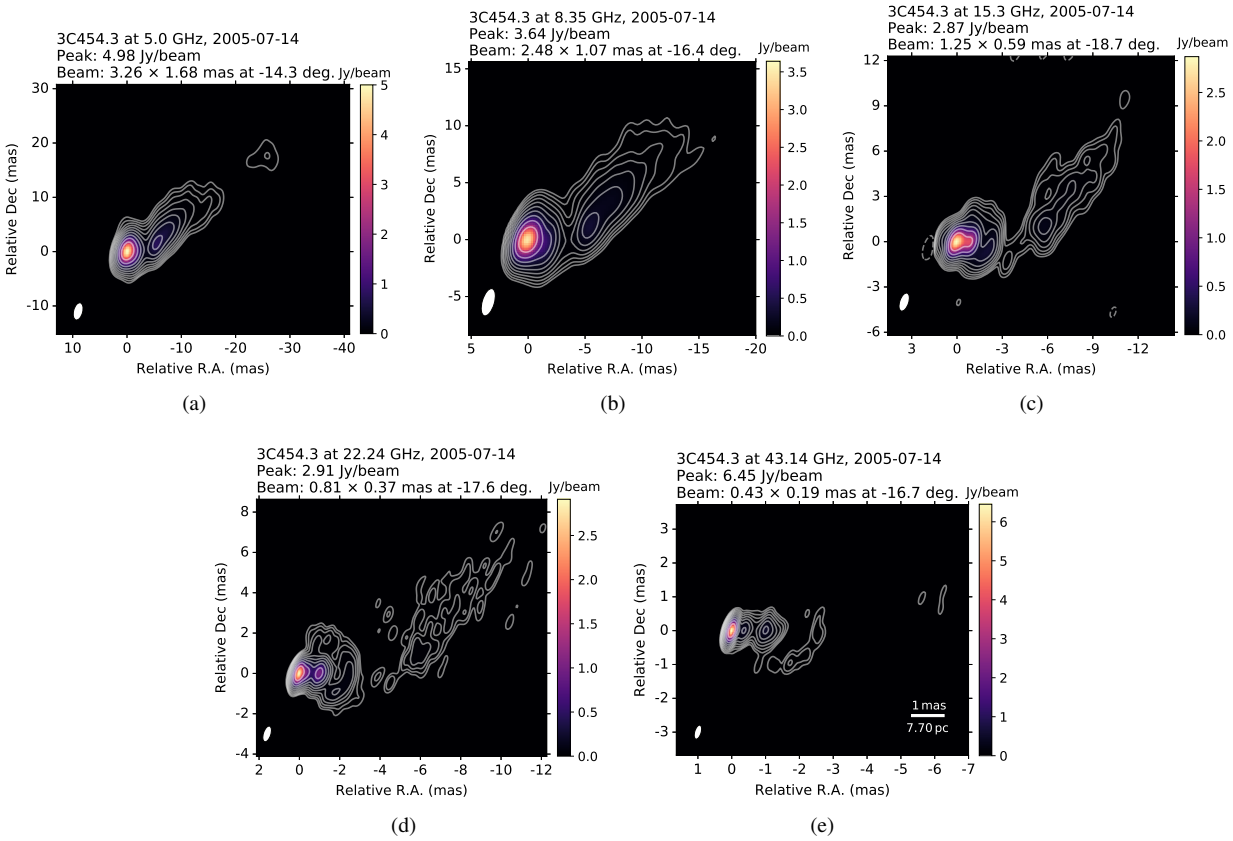


**Fig. 1.** CLEAN images of 3C 454.3 on 2005 July 14 of the following frequency bands: (a) $C$, (b) $X$, (c) $U$, (d) $K$ and (e) $Q$ with contours at −0.1%, 0.1%, 0.2%, 0.4%, 0.8%, 1.6%, 3.2%, 6.4%, 12.8%, 25.6%, and 51.2% of the peak intensity at each image. The interferometric beam (ellipse) is displayed in the bottom left corner of each image. The rms noise levels from the lowest to the highest frequency are 0.11, 0.20, 0.35, 0.30 and 0.38 mJy beam$^{-1}$.

the same restoring beam size (as the lower frequency image). Next, the image alignment was performed for adjacent pairs of frequencies (i.e. CX, XU, UK, KQ) using a similar procedure to that described in Pushkarev et al. (2012). Here, for example, the CX notation means that the alignment of the $C$-band image was done with respect to the $X$-band image. Finally, to obtain a statistical average of the image shift with associated uncertainty, we performed the alignments ten times per frequency pair, selecting slightly different optically thin features each time, similarly to the analysis in Chamani et al. (2021). The procedure involved five alignments with matched common $(u, v)$ range images and five full $(u, v)$ range images. The resulting spectral index maps have both the common and full $(u, v)$ range of a frequency pair. A common $(u, v)$ range means that the lower limit of the $(u, v)$ distance for both images is the lower limit of the high frequency, and the upper limit coincides with the upper limit of the low frequency. Spectral index maps with a common $(u, v)$ range should be used in any analysis of the extended, optically thin emission since the missing short $(u, v)$ spacings at the higher frequency can result in artificial steepening of the spectrum of the extended emission features. The common $(u, v)$ range spectral index images are displayed in Appendix F.

### 3.2. Visibility plane model fitting

In order to accurately measure the core position, we fitted simple models of the source structure directly to the visibilities. We used the (fully self-) calibrated visibility data and model-fitted the core with 2D Gaussian components consisting of circular components at each frequency. To model the core, we first removed the CLEAN components from the nuclear region in the jet (around the brightest pixel), leaving the extended emission unchanged. In general, the area removed was one-beam size for all frequencies; however, at the low frequencies ($C$, $X$ bands) the area had to be increased in order to obtain better Gaussian fits, an approach similar to that performed by Homan et al. (2021). The model fits were performed minimizing the reduced $\chi^2$ with a Levenberg-Marquardt non-linear least-squares fitting algorithm implemented in `DIFMAP` so that a value as close to one as possible was reached. Then we combined the core coordinates (from the map centre) with the image shifts measured by 2D cross-correlation to estimate the core-shift vectors by following the method described in Pushkarev et al. (2012). We calculated, in particular, the core-shift vectors for the adjacent frequency pairs: CX, XU, UK, and KQ.

A typical VLBI image often has the brightest feature at the upstream end of the jet. This structure is usually assumed to be the core of the jet; however, in 3C 454.3, at some epochs, the core region requires several components, reflecting a complex nuclear structure in this source. The emergence of such features was already found at 2.8 cm (10.7 GHz) in the 1980s by Pauliny-Toth et al. (1987). Their study suggests that the additional features near the core may be stationary shocks. Another alternative includes the possibility of blending the core with the jet (e.g. Kovalev et al. 2008; Sokolovsky et al. 2011; Algaba et al. 2019). Hence, the presence of several features can lead to the misidentification of the true core, and the identification of the core (i.e. $\tau = 1$ surface) is non-trivial. This

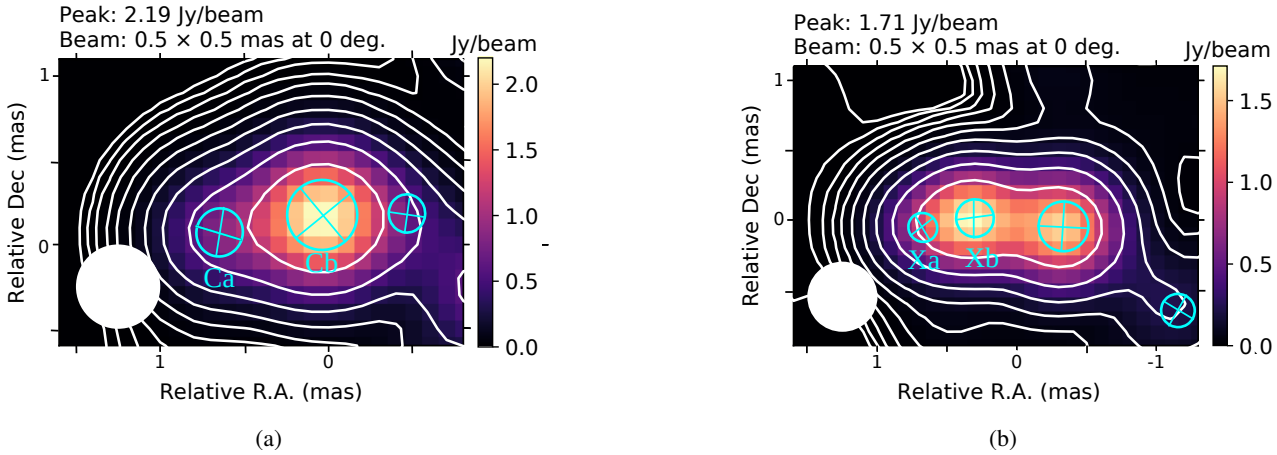


(a) (b)

**Fig. 2.** Super-resolved CLEAN images of 3C 454.3 on 2005 July 14 with contours at 0.1%, 0.2%, 0.4%, 0.8%, 1.6%, 3.2%, 6.4%, 12.8%, 25.6%, and 51.2% of the peak intensity at each image. The 2D Gaussian components in the core region are shown in cyan. (a) At the *C* band (5 GHz), the features are labelled 'Ca' for the upstream feature and 'Cb' for the downstream feature or bright component. (b) Similarly, at *X* band (8.4 GHz), the components are labelled 'Xa' and 'Xb'.

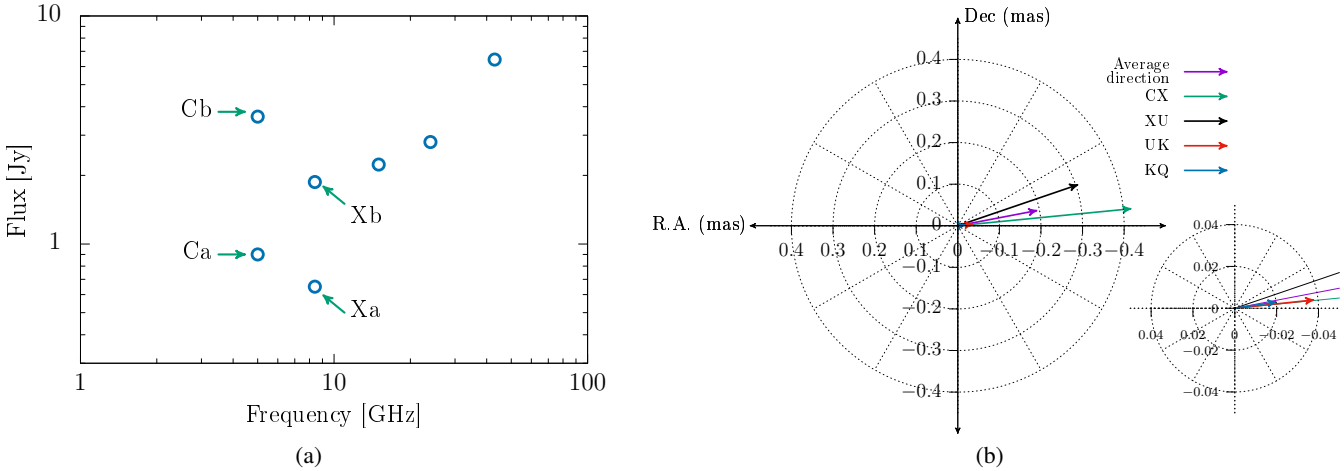


(a) (b)

**Fig. 3.** 2D-Gaussian components at low frequencies. (a) Radio spectrum (5 GHz to 43 GHz) of core and jet features in 3C 454.3 in 2005 July 14. The flux densities of the upstream components are labelled 'Ca' and 'Xa' and the downstream components 'Cb' and 'Xb'. (b) Core-shift vectors of each frequency pair and average vector direction in a polar grid. The dotted lines are given at intervals of 30°. In the bottom right corner is a zoomed-in image of the core-shift vector pairs for the high-frequency pairs. All vectors consistently point in the large-scale jet direction towards the west (see Fig. 1). The true cores are features Cb and Xb at the *C* and *X* bands, respectively, since they produce core-shift vectors whose direction is consistent with the jet direction. Comparisons of the core-shift vectors produced by the other *C* and *X* component choices are displayed in Appendix B.

turned out to be an issue at the two lowest frequencies (5 and 8 GHz). An example of this is displayed in Fig. 2, where a moderately bright emission feature is seen upstream of the brightest emission at the *C* and *X*-bands. The two components in the core region are labelled 'Ca' and 'Cb' at the *C* band and 'Xa' and 'Xb' at the *X* band. The flux of each component is labelled in the core spectrum displayed in Fig. 3a.

In order to correctly identify the core at each frequency, we calculate the CX and XU core-shift vectors by taking the following combinations: Ca/Xa, Ca/Xb, Cb/Xa, and Cb/Xb. In many cases it is expected that only one of the combinations will lead to both the CX and XU core-shift vectors pointing in the expected jet direction (towards the west) and resulting in a single power-law frequency dependence. For example, we found that the unique combination Cb-Xb leads to correct CX and XU core-shift directions in the 2005 July 14 epoch, as shown in Fig. 3b. The other combinations produce CX and/or XU core-shift vectors that do not align with the jet direction. These combinations are displayed in Appendix B. The correct combination is also verified by the resulting power-law fits. A fit is considered acceptable as long as the core shifts are not too large to look unrealistic (which can be driven by the wrong choice of the core at the low frequencies). Hence, this approach allows us to identify the most likely core component in each image.

Since the core identification plays a crucial role in accurate core-shift measurements and consequently the estimation of the core-shift index $k_r$, we employed the criteria described above as a sanity check for the observing epochs where the core identification at the low frequencies is unclear; these epochs are specified in Table A. The model fitting of the core for the *U*, *K* and *Q* bands, in general works well with one single circular Gaussian. However, an emerging new component was identified at the *Q* band in our data sets in 2009 and 2010. The ejection of a new emission feature is possibly related to the strong flaring event in 2009. Although we do not aim to study the jet kinematics of 3C 454.3 in this paper, we discuss this specific

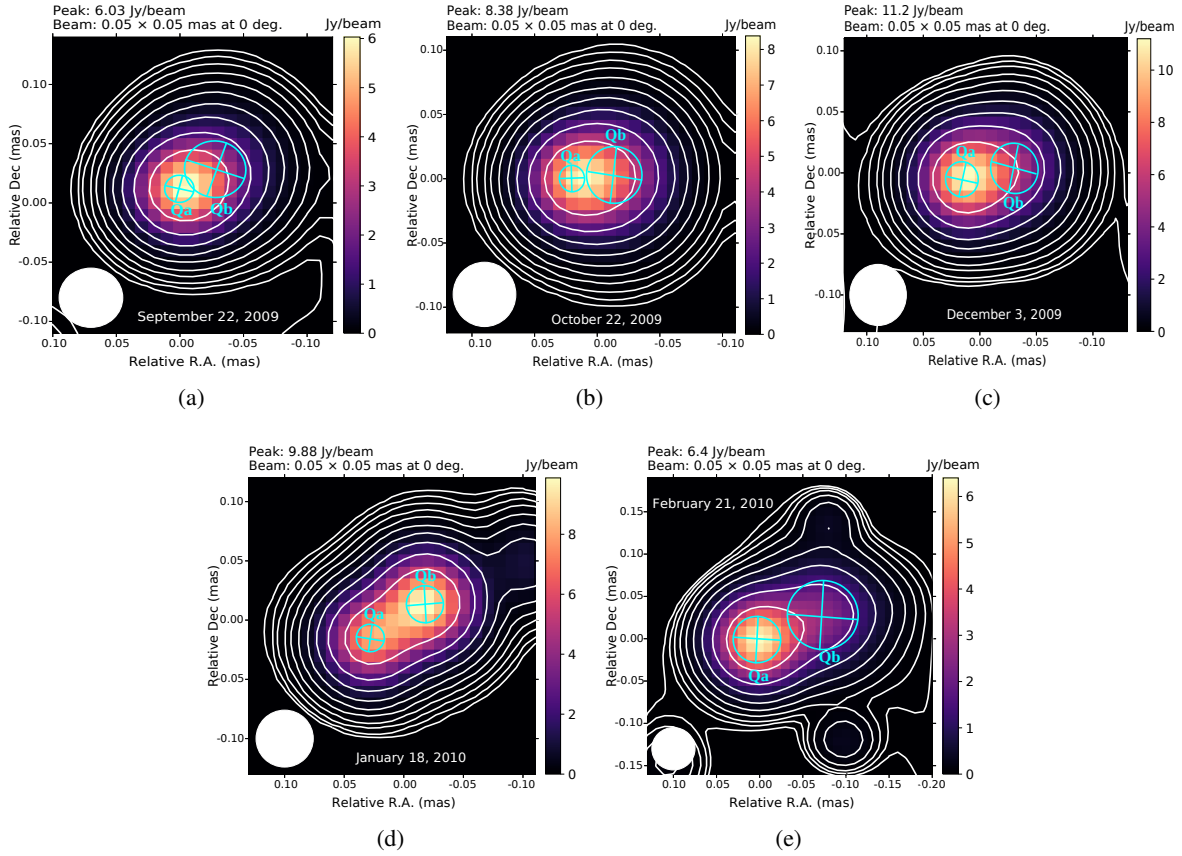


**Fig. 4.** Super-resolved images of 3C 454.3 at 43 GHz for five different epochs from 2009 to 2010. The contours are given at 0.1%, 0.2%, 0.4%, 0.8%, 1.6%, 3.2%, 6.4%, 12.8%, 25.6%, and 51.2% of the peak intensity at each image. Each map uses a circular convolving beam of 0.05 mas and the components are displayed in cyan. The restoring beam (circular) is displayed in the bottom left corner of each image. The rms noise level is in (a) 1.1, (b) 2.4, (c) 4.1, (d) 7.7, and (e) 2.9 mJy beam$^{-1}$. The core labelled 'Qa' and 'Qb' denotes a bright, recently ejected component that is moving downstream.

ejection in the following section, since it significantly affects the core-shift measurements.

### 3.3. Ejection of a moving feature downstream at 43 GHz in the period 2009–2010

In 2009–2010 the nuclear region at 43 GHz was modelled first with one circular Gaussian; however, the fit became better and more stable with two circular components, which indicated that an emission feature had been ejected from the core. Figure 4 shows the two resolved, bright components (in cyan). The core is labelled 'Qa' and the moving feature downstream 'Qb'. The feature follows an east−west trajectory. The flux density curves of each component are shown in Fig. 5. Since the core and the moving feature are so close to each other they can 'swap flux' in model fitting. This means that the flux ratio of the two components is uncertain, and the formal flux uncertainties of the fit (shown in Fig. 5) likely underestimate the errors. Finally, we note that the moving feature tracked from September 2009 to February 2010 may be cross-identified by the knot K09 in Jorstad et al. (2013).

Figure 6 displays the feature separation from the core as a function of time. The errors of the core separation are small since both components are very bright. The uncertainties in the component position were derived from Gaussian model fitting by moving the component by small amounts around the best-fit position, fixing the component position, and finding the set of remaining parameters that minimize the $\chi^2$. The errors are found

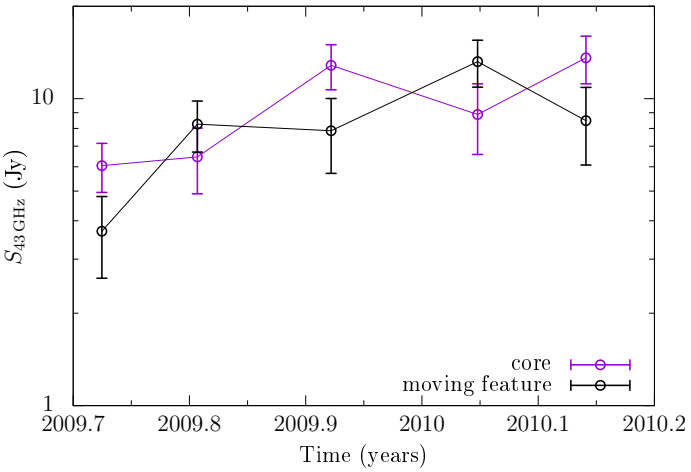


**Fig. 5.** Flux density at 43 GHz of the core and the moving feature downstream as a function of time. The error bars include the uncertainty in the flux scale which is ∼10%.

by requiring $\Delta\chi^2 = \chi^2 - \chi^2_{\mathrm{min}} < C^{\alpha}_{p}$, where $\chi^2_{\mathrm{min}}$ is the minimum $\chi^2$ corresponding to the best-fit model and $C^{\alpha}_{p}$ is the critical value of $\chi^2$ distribution for $p$ degrees of freedom and a significance level $\alpha$ (we use $\alpha = 0.32$ corresponding to $1\sigma$ errors; for details, see Chamani et al. 2021).

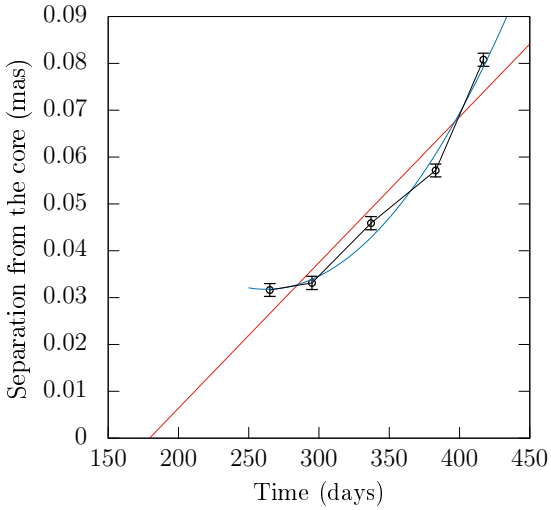


**Fig. 6.** Separation of the moving feature (see Fig. 4) from the core as a function of time at 43 GHz. The first day is counted from 2009 January 01. The black circles indicate the observations on 2009 September 22, 2009 October 22, 2009 December 03, 2010 January 18, and 2010 February 21. The red and blue curves indicate linear and accelerating fitting functions, respectively.

A linear function was fitted to the data to follow the trajectory of the moving feature. The fitting model gives $d = -(0.06 \pm 0.02) + (3 \pm 0.5) \times 10^{-4}\, t$, where $d$ is the separation (mas) from the core and $t$ the time (days from 2009 January 01). Hence, the feature has a proper motion of $(0.11 \pm 0.02)$ mas yr$^{-1}$ corresponding to an apparent superluminal speed of $\beta_{\rm app} = 5.0 \pm 1.0$. The new feature's extrapolated ejection time ($T_0$) is 179±66 days corresponding to 2009 June 28, or equivalently to 2009.49±0.18. On the other hand, fitting an accelerating model gives $d = (0.17 \pm 0.08) - (1 \pm 0.5) \times 10^{-3}\, t + (2 \pm 0.7) \times 10^{-6}\, t^2$, where the acceleration of the feature is $(0.26 \pm 0.09)$ mas yr$^{-2}$. We note that in Jorstad et al. (2013), the new component K09 is tracked only from January 2010 on, and it moves at $(0.21 \pm 0.02)$ mas yr$^{-1}$, corresponding to $\beta_{\rm app} = 9.6 \pm 0.6$ and $T_0 = 2009.86 \pm 0.05$ (using 24 epochs). In their study, they estimated two acceleration components both along and perpendicular to the jet given by $(0.10 \pm 0.01)$ and $(0.13 \pm 0.02)$ mas yr$^{-2}$, respectively. Additionally, the flux density of the moving feature in early 2010 is comparable to the flux density of K09 shown in Fig. 13 in Jorstad et al. (2013). The separation from the core is below 0.1 mas and is similar to our observed values. Hence, we conclude that K09 is likely the same feature we detected in late 2009 and early 2010. If this is the case, the moving feature has experienced acceleration, which can explain the factor of two difference in the average speeds.

## 4. Results

In previous sections we described our method to identify the core and the estimations of the core shifts for adjacent frequency pairs. Here we present and analyse the resulting core shifts.

### 4.1. Core-shift measurements and variability

We list in Table A.1 the core-shift vectors with components in right ascension (RA) and declination (Dec), as well as the core-shift absolute values and projected absolute values. The projected absolute values were obtained by projecting the core-shift vectors onto the average vector direction, as described in Sect. 4.1 in Chamani et al. (2021). This is done to diminish the effect of random errors on core-shift vector directions, and it is implicitly assumed that the jet is straight at any given epoch. The total positional uncertainties of the core shifts (for both coordinates) are estimated as

$$\Delta\theta_{\rm total,core-shift} = \sqrt{\Delta\theta^2_{\rm 2DCC} + \Delta\theta^2_{\rm core-position}}\,, \quad (1)$$

where $\Delta\theta_{\rm 2DCC}$ is the error obtained from the 2D image cross-correlation analysis, and $\Delta\theta_{\rm core-position}$ is the error of the core position obtained from the 2D Gaussian model fitting. For the latter we employed the same method as used by Chamani et al. (2021), and also described in Sect. 3.3.

By following the method and notation for the core identification described in the previous section (see Figs. 2 and 3), we present in Appendix D the core spectrum, the core-shift vectors, and the core-shift power-law fit for each epoch. Using the absolute (projected) core shifts in Appendix A we fitted the data with power-law curves using 43 GHz as the reference frequency,

$$\Delta r = a\,(\nu_{\rm GHz}^{-1/k_r} - 43^{-1/k_r}), \quad (2)$$

where $\Delta r$ represents the core shift in mas, $\nu$ is the observing frequency, $a$ is a fitting parameter, and $k_r$ is the core-shift power-law index. The fitting parameters are summarized in Table 2.

We found, in general, that all core-shift vectors point towards the west−north−west direction, which agrees well with the jet direction downstream of the 3C 454.3 jet. Changes in the direction towards the south-west are seen in some core-shift vectors, for instance in Figs. D.1, D.13–D.18. Major flaring events were registered for instance in May 2005 and from late 2009 to early 2010, which might have affected the direction of some core-shift vectors.

We note that the core shift at the $U$ band is off the fitting curve in the observation on 2008 December 07; thus, we dropped 15 GHz from the fit at this epoch. The data set without the $U$-band data point yields a better fit at this epoch (see Fig. D.13). A similar case is seen in the observation on 2009 September 22 (see Fig. D.14). Furthermore, the outburst starting in late 2009 appears to affect the core-shift measurements of the last five epochs. In these observations, the core-shift vectors changed the direction significantly towards the south−west, and the functional form of the core shift changed significantly with $k_r$, increasing to values above one, and the typical core-shift behaviour became distorted in some cases. This effect is evident on 2009 December 03, where the core-shift for the $K$ band increased by a factor of two from the previous epoch. As a consequence, the fit became poor, deviating greatly from a power law (see Fig. D.16c). Hence, we did not include this epoch for the further analysis described in the next subsections. Even though the core shifts are not greatly distorted on 2010 January 18 and 2010 February 21, the uncertainties are large and the fits exhibit considerable deviations from $k_r = 1$ (see Figs. D.17d and D.18d).

We plot the core-shift variability in Fig. 7. The plots show the absolute values of the XU and CQ core shifts as a function of time. For comparison, we included the XU core-shift values measured by Pushkarev et al. (2012). Their values lie well within the range of our measurements between 0.05 mas and 0.34 mas. The mean XU core shift is $0.14 \pm 0.02$ mas with a standard deviation, $\sigma$, of 0.09 mas. In order to test whether the XU core shift is variable given the measurement uncertainties, we set up a null hypothesis stating that the core shift does not vary and remains

**Table 2.** Core-shift power-law fit parameters.

| Epoch | Date | $k_r$ | $a$ |
|---|---|---|---|
| 1 | 2005-05-19 | $0.70 \pm 0.10$ | $2.6 \pm 1.1$ |
| 2 | 2005-07-14 | $0.45 \pm 0.05$ | $29.4 \pm 12.5$ |
| 3 | 2005-09-01 | $0.52 \pm 0.07$ | $19.6 \pm 9.2$ |
| 4 | 2005-12-04 | $0.70 \pm 0.10$ | $7.2 \pm 2.7$ |
| 6 | 2006-10-02 | $1.0 \pm 0.3$ | $1.7 \pm 0.8$ |
| 7 | 2006-12-04 | $0.67 \pm 0.07$ | $4.4 \pm 1.3$ |
| 8 | 2007-01-26 | $0.65 \pm 0.06$ | $3.8 \pm 1.1$ |
| 9 | 2007-04-26 | $0.80 \pm 0.10$ | $2.8 \pm 1.0$ |
| 10 | 2007-06-16 | $0.60 \pm 0.10$ | $5.9 \pm 2.5$ |
| 11 | 2007-07-25 | $0.69 \pm 0.05$ | $4.5 \pm 0.8$ |
| 12 | 2007-09-13 | $0.90 \pm 0.10$ | $4.2 \pm 0.8$ |
| 14 | 2008-12-07 | $1.4 \pm 0.4$ [(a)] | $1.7 \pm 0.6$ |
| | 2008-12-07 | $1.1 \pm 0.1$ [(b)] | $2.3 \pm 0.4$ |
| 15 | 2009-09-22 | $1.1 \pm 0.6$ [(c)] | $1.7 \pm 1.2$ |
| | 2009-09-22 | $0.8 \pm 0.3$ [(d)] | $2.4 \pm 1.7$ |
| 16 | 2009-10-22 | $1.1 \pm 0.3$ | $3.4 \pm 1.4$ |
| 17 | 2009-12-03 [(†)] | – | – |
| 18 | 2010-01-18 | $1.7 \pm 0.7$ | $1.6 \pm 0.5$ |
| 19 | 2010-02-21 | $1.3 \pm 0.3$ | $1.7 \pm 0.5$ |

**Notes.** $k_r$ is the core-shift index, $a$ is a fitting parameter. Rounded values are given here. The 13th observing epoch (2008-01-03) was dropped from the analysis. [(a)]Using all frequency bands, see D.13c. [(b)]Without the $U$ band, see Fig. D.13e. [(c)]Using all frequency bands, see D.14e. [(d)]Without the $U$ band, see Fig. D.14f. [(†)]No good power-law fit, see Fig. D.16d.

stable around the mean value and calculated the $\chi^2$ statistic,

$$\chi^2 = \sum_i^N \frac{\left(\Delta r_{(\nu_1\nu_2)i} - \overline{\Delta r_{\nu_1\nu_2}}\right)^2}{\sigma_i'^2}, \tag{3}$$

where $\Delta r_{(\nu_1\nu_2)i}$ represents the core shift of the $i$th observation between two frequencies, $\nu_1$ and $\nu_2$ ($\nu_2 > \nu_1$); $\sigma_i'$ is the core-shift error; $\overline{\Delta r_{\nu_1\nu_2}}$ is the mean core shift; and $N(= 17)$ is the number of observations. At the 99.9% confidence level for $N-1$ degrees of freedom (d.o.f.), $\chi^2_{\rm critical} = 39.25$ is the critical value for rejecting the null hypothesis. For XU core shift ($\Delta r_{\rm XU}$), $\chi^2$ results in 312.5, which is above the critical value, confirming that the XU core shift significantly varies with time.

A similar analysis was also performed for the CQ core shifts ($\Delta r_{\rm CQ}$; see Fig. 7b) where the mean value is $0.49 \pm 0.05$ mas with a standard deviation of 0.18 mas. The core shifts vary between 0.27 mas and 0.86 mas. There is one extreme core-shift value, $1.64 \pm 0.04$ mas, on 2008 January 03. Since this observation misses both St. Croix and Hancock for the whole observation, as well as Brewster for half of the observation, the resulting poor $(u, v)$ coverage makes this result suspect, and we drop it from our analysis and from Fig. 7. The $\chi^2$ test for the CQ core shift gives 279.02 (for $N = 17$), above the critical level. Thus, the CQ core shift also shows significant variability. Overall, the variability curves of both the XU and CQ core shifts exhibit similar trends, although there is no one-to-one correspondence.

Additionally, we studied the mean core-shift direction variability, which represents approximately the overall inner jet direction (PA) in the core region. The mean jet PA was measured by averaging the direction of the core-shift vectors of all frequency pairs. The PA variability plot is presented in Fig. 8. For the study period, the mean jet PA is $-80° \pm 3°$, $\sigma \sim 10.8$,

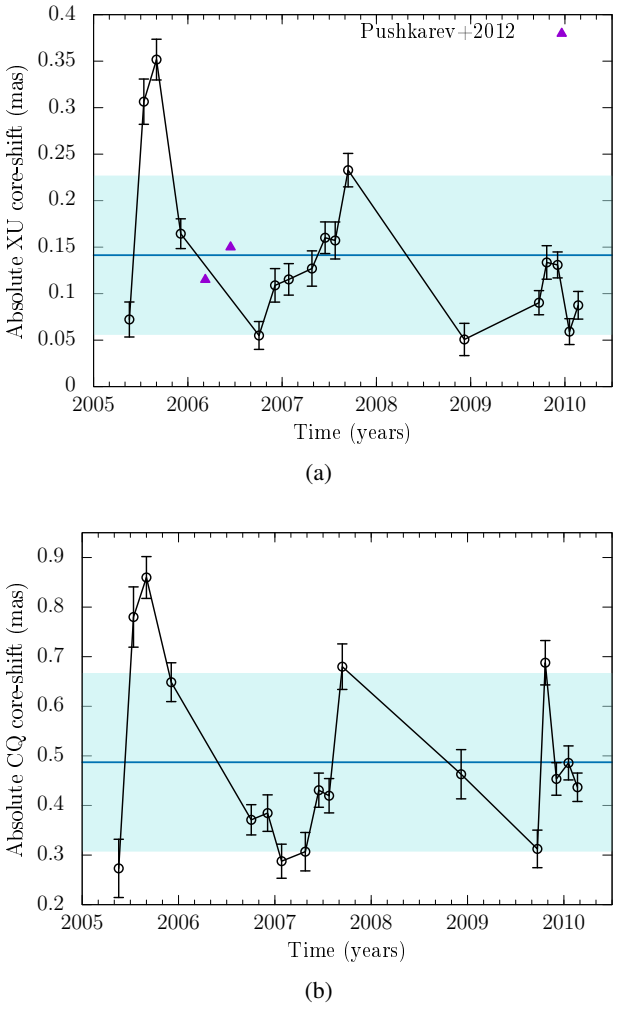


**Fig. 7.** Variability of the core shift in 3C 454.3. (a) Core shift between the $X$ (8 GHz) and $U$ (15 GHz) bands vs. time. The purple triangles represent the core shifts derived by Pushkarev et al. (2012). (b) Core shift between the $C$ (5 GHz) and $Q$ (43 GHz) bands vs. time. In both panels the mean value is represented by the blue line and $\pm\sigma$ is displayed by the shaded cyan background. The epoch 2008 January 03, which had three missing antennas, was dropped from this plot as an outlier with a CQ core shift of $1.64 \pm 0.04$ mas. Zero core shift physically means that the cores at two frequencies coincide at the same location.

$\chi^2 = 13.66$ (for $N = 17$). The last is below the critical value ($\chi^2_{\rm critical} = 39.25$) indicating no significant jet PA variability. That means that even if there is significant core-shift variability, the jet vector direction stayed relatively stable in our study period. While the changes in jet PA are not statistically significant, it is interesting to note an increasing trend in the PA from mid-2005 to early 2006, corresponding to a major millimetre wavelength flare, and then more or less stable PA from late 2006 to late 2007. Possibly related to the strong outburst, PA decreased to lower values from late 2009 to early 2010.

### 4.2. Variability of the core-shift index $k_r$

Core-shift indices $k_r$ are listed in Table 2, and the variability plot of $k_r$ is displayed in the bottom panel of Fig. 9. For comparison, we included the result obtained by Kutkin et al. (2014) for a single observation. We find that $k_r$ varies in the range $0.45 < k_r < 1.7$, with an average value of $0.85 \pm 0.08$ and

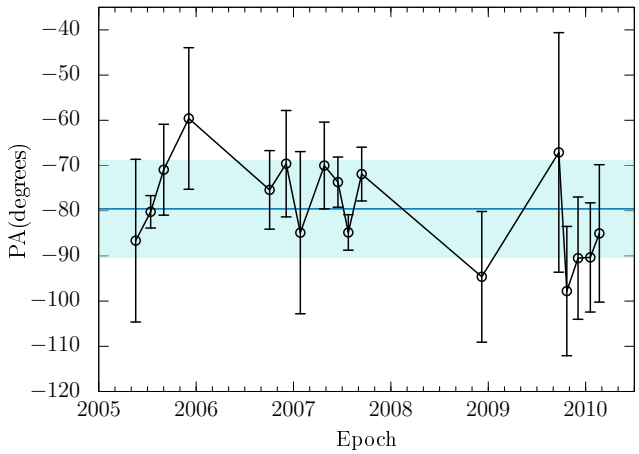


**Fig. 8.** Time variability of the jet position angle (PA) from the model fitting to the core. The PA values (black open circles) represent the average PA per epoch using all core-shift vectors per frequency pair (CX, XU, UK, KQ). The blue line is the mean PA for the whole data set. The area in light cyan represents $\pm 1\sigma$.

with a standard deviation $\sigma = 0.30$. We note that we dropped the observation on 2009 December 03 since the fitting result gives an unreasonably large $k_r$ value that is due to the ongoing flare significantly increasing the KQ core-shift value, while the lower frequencies are not affected (see Fig. D.16d). It is important to point out that $k_r$ indices in the period of 2009 to 2010 have large uncertainties due to the strong flare affecting the core-shift measurements (see Figs. D.14–D.18). It appears that the flare increases the distance between the 24 and 43 GHz cores. This may be due to several reasons, including increased particle density and/or magnetic field strength due to the flare that increases the synchrotron opacity and moves the 24 GHz core downstream. It is also possible that the blending of the newly ejected component with the core at 24 GHz drags the apparent core position downstream. In any case, the power-law dependences measured during this period are disrupted by the flare and the measured $k_r$ values are affected.

Similarly to the variability test of the core shift, we set up a null hypothesis that $k_r = 1$ and does not vary over time. We also included in the analysis the result from (Kutkin et al. 2014). The chi-square test resulted in $\chi^2 = 146.50$, which is above the critical value (for $N = 17$). If we exclude the epochs from 2009 to 2010, the mean of $k_r$ is $0.74 \pm 0.05$ with $\sigma = 0.18$, and $\chi^2 = 67.16$, which is still above the corresponding critical value of $\chi^2_{\rm critical} = 32.91$ (12 d.o.f.). Hence we reject the null hypothesis and conclude that $k_r$ is indeed also a variable parameter. These results could indicate that the jet in 3C 454.3 does not always stay in equipartition or does not follow the classical Blandford & Königl jet model. The last explanation also includes the possibility that the core is not strictly a $\tau = 1$ surface at our highest observing frequencies during the strong flares.

The variability plot of $k_r$ is displayed in the bottom panel of Fig. 9; $k_r$ indices below 1 can occur either during flaring (2005 to 2006) or quiescent episodes (2007). These results indicate that the jet in 3C 454.3 cannot be described with the ideal BK79 model with equipartition and conical jet assumptions even during the quiescent period. On the other hand, $k_r$ values close to one within the uncertainties are found in a quiescent state (late 2006 and late 2007), post-flare (December 2008), and during flaring periods (late 2009 to early 2010).

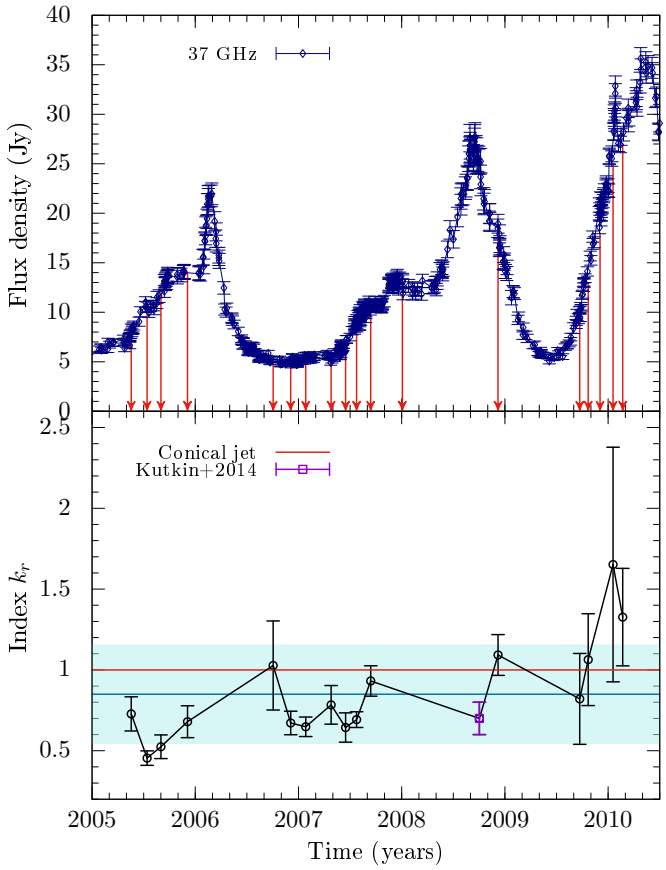


**Fig. 9.** Comparisons of the source activity and the core-shift index. Top: Total flux density at 37 GHz for 3C 454.3 observed at the Metsähovi Radio Observatory. The red arrows show the time correspondence with our VLBA observations. Bottom: Core-shift power-law $k_r$ index vs. time. The measured $k_r$ values are represented as black open circles. The purple square, $0.7 \pm 0.1$, represents the value obtained by Kutkin et al. (2014). The observation epoch on 2009 December 03 is not included. The blue dashed line shows the mean for the whole data set. The area in cyan represents $\pm 1\sigma$. The red line represents the ideal BK79 conical jet with $k_r = 1$.

### 4.3. Core position

The core position or distance from the central engine, $r_{\rm core}$, at frequency $\nu$ is given by

$$r_{\rm core}(\nu_{\rm GHz}) = \frac{\Omega_{r\nu}}{\nu_{\rm GHz}^{1/k_r} \sin\theta} [\rm pc], \tag{4}$$

where $\Omega_{r\nu}$ is the core offset; $\theta$ is the source's viewing angle, which is a fixed constant parameter here (Lobanov 1998); $\Omega_{r\nu}$ is formulated as

$$\Omega_{r\nu} = 4.85 \cdot 10^{-9} \frac{\Delta r_{\nu_1\nu_2} D_L}{(1+z)^2} \frac{\nu_1^{1/k_r} \nu_2^{1/k_r}}{\nu_2^{1/k_r} - \nu_1^{1/k_r}} [\rm pc\,GHz^{1/k_r}], \tag{5}$$

where $D_L$ denotes the luminosity distance; $\Delta r_{\nu_1\nu_2}$ is the core shift measured in mas at two frequencies, and $z$ is the redshift.

To measure $r_{\rm core}$ at each frequency, we employed the mean value of $\Omega_{r\nu}$ per epoch given by $(\Omega_{r,\rm CX} + \Omega_{r,\rm XU} + \Omega_{r,\rm UK} + \Omega_{r,\rm KQ} + \Omega_{r,\rm CQ} + \Omega_{r,\rm XQ} + \Omega_{r,\rm UQ})/7$. The uncertainties of $r_{\rm core}$ were obtained via error propagation of Eq. (5), and the details are presented in Appendix C. We use $r_{\rm core}$ for a further analysis presented in Sect. 4.5.

**Table 3.** Physical properties of 3C 454.3.

| Name | Parameter | Value |
|---|---|---|
| Redshift [(a)] | $z$ | 0.859 |
| Luminosity distance [(b)] | $D_{\rm L}$ | 5.49 Gpc |
| Doppler factor [(c)] | $\delta$ | 24.6 ± 4.5 |
| Lorentz factor [(c)] | $\Gamma$ | 15.6 ± 2.2 |
| Viewing angle [(c)] | $\theta$ | 1.3° ± 1.2° |
| Half-opening angle [(c)] | $\theta_{\rm j}$ | 0.8° ± 0.2° |
| Black hole mass [(d)] | $M_{\rm BH}$ | $4.9 \times 10^8\ M_\odot$ |
| Accretion disc luminosity [(d)] | $L_{\rm acc}$ | $7.2 \times 10^{46}$ erg s$^{-1}$ |

**Notes.** [(a)]Observed by Sargent et al. (1988), Jackson & Browne (1991). [(b)]Using the online calculator of Wright (2006). [(c)]Global jet parameters adopted from Jorstad et al. (2005). We assumed that parameters remain constant during the period 2005–2010. [(d)]Values adopted from Zamaninasab et al. (2014, with references therein).

### 4.4. Magnetic field parameters

The magnetic field at 1 pc from the jet apex, $B_{\rm 1pc}$, can be estimated from the measured core shift as long as the energy equipartition between the magnetic field and radiating particles at the radio core holds (Lobanov 1998; Hirotani 2005). The expression for $B_{\rm 1pc}$ used in several previous works (e.g. Hirotani 2005; O'Sullivan & Gabuzda 2009; Zamaninasab et al. 2014) misses one $(1 + z)$ term, as shown by Zdziarski et al. (2015). We take into account this factor and use the corrected version,

$$B_{\rm 1pc} \approx 0.025 \left[ \frac{\sigma_{\rm rel}\, \Omega_{r\nu}^{3k_r}\, (1+z)^3}{\delta^2\, \theta_{\rm j}\, \sin^{3k_r-1}\theta} \right]^{\frac{1}{4}} \ [\rm G], \tag{6}$$

where $\sigma_{\rm rel}$ is the ratio of magnetic to particle energy densities and is taken as unity, $\delta$ is the Doppler factor, and $\theta_{\rm j}$ is the jet's half opening angle. The physical properties of 3C 454.3 relevant for the magnetic field parameter estimations are summarized in Table 3. We adopted from Jorstad et al. (2005) the average values for $\delta$, $\Gamma$, and $\theta$. We note that Jorstad et al. (2010, 2013) obtained $\delta$, $\Gamma$, and $\theta$ for several ejected components named K1, K2, K3, K09, and K10. Jorstad et al. (2010) shows that K1, K2, and K3 were ejected in 2005.5, 2007.49, and 2007.93, respectively. Component K09 (described in Sect. 3.3) was ejected in mid-2009, and K10 appeared to be ejected at the end of 2010 according to Jorstad et al. (2013). Components K1, K2, and K09 have measured $\delta$, $\Gamma$, and $\theta$ values, which are similar and in good agreement with the parameter values measured by Jorstad et al. (2005). Since these appear to be relatively stable at least for our period of study, we kept them as constants. Component K3 has a significantly higher Lorentz factor and a smaller viewing angle, and consequently significantly higher $\delta$. However, we consider K3 here as a likely outlier since it faded away much closer to the core (<0.2 mas; Jorstad et al. 2013) compared to the other components.

To estimate $B_{\rm 1pc}$, we employ the CQ core shift per epoch together with the $k_r$ measurements. The uncertainties on $B_{\rm 1pc}$ are evaluated by error-propagating Eq. (6) and taking into account the uncertainties on $\delta$, $\theta$, and $\theta_{\rm j}$ (see Appendix C). The $B_{\rm 1pc}$ values as a function of time are shown in Fig. 10. The results show an evident discrepancy in $B_{\rm 1pc}$, meaning that there is up to an order of magnitude difference in $B_{\rm 1pc}$ between $k_r = 1$ and $k_r \neq 1$. Furthermore, $B_{\rm 1pc}$ varies more than two orders of magnitude when $k_r \neq 1$. These results suggest that reliable $B_{\rm 1pc}$ estimations can be obtained only as long as $k_r = 1$, which is understandable remembering the assumptions underlying Eq. (6) (i.e. an ideal Blandford & Königl conical jet and equipartition). If we cannot reasonably assume that these hold, then the resulting $B_{\rm 1pc}$ values are suspect.

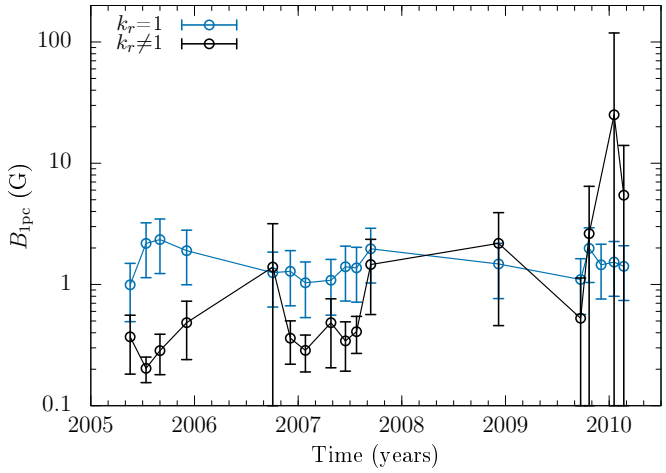


**Fig. 10.** Magnetic field $B_{\rm 1pc}$ at one parsec by employing the CQ core shift pair. We use here the (projected) core shift absolute values. The blue open circles represent the results assuming $k_r = 1$. The black open circles represent the results using measured $k_r$ values.

**Table 4.** $B_{\rm 1pc}$ values using $k_r = 1$.

| Epoch | $B_{\rm 1pc}$(G) |
|---|---|
| 2006-10-02 | 1.3 ± 0.6 |
| 2007-09-13 | 2.0 ± 0.9 |
| 2008-12-07 | 1.5 ± 0.7 |
| 2009-10-22 | 2.0 ± 0.9 |

**Notes.** The epochs selected have measured $k_r$ indices near one.

We assume the $B_{\rm 1pc}$ estimations to be more reliable when our measured $k_r$ indices are near one and consistent within the error bars. From our results shown in Fig. 10, only four observations satisfy this condition. Thus, using $k_r = 1$, the magnetic fields for the four epochs are displayed in Table 4. In this table, the weighted mean $B_{\rm 1pc}$ is (1.5 ± 0.4) G, which is comparable with the value of 1.1 G obtained by Pushkarev et al. (2012). We note that Hu et al. (2021) made recent estimations of the magnetic field in 3C 454.3 based on the spectral fitting of six SEDs with a one-zone leptonic jet model concentrated around the time of the strong gamma-ray flares in 2009. For the two epochs, they can constrain the distance of the emission region from the central engine. They obtain 0.7−1.0 G at the distance of 0.3−0.4 pc, which means that their inferred magnetic field strength is smaller by a factor of about five compared to what is expected based on our results if the magnetic field strength scales as $r^{-1}$.

We further use the observations listed in Table 4 to estimate the jet's magnetic flux in 3C 454.3. We examined whether the magnetic flux value is consistent with the source having developed a magnetically arrested disc (MAD). We adopted the formula for jet magnetic flux derived by Zdziarski et al. (2015), who considered the observed condition of $\Gamma\theta_{\rm j} \sim 0.1$ and $\Gamma\theta \neq 1$ for blazars and radio galaxies, respectively, instead of $\Gamma\theta_{\rm j} = 1$ assumed in the original Zamaninasab et al. (2014) paper. The updated formula for the magnetic flux used by

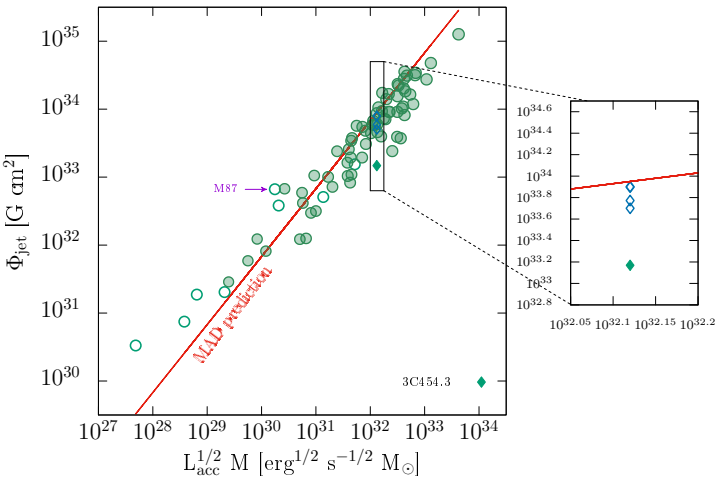


**Fig. 11.** Measured $\Phi_{jet}$ vs. $L_{acc}^{1/2}$M for radio galaxies (open circles) and blazars (filled circles) shown in green. The plot is adapted from Zamaninasab et al. (2014), and it uses the corrections from Zdziarski et al. (2015; see also Chamani et al. 2021). The blazar 3C 454.3 is marked with the green diamond. The plot on the right zooms in on the values only for 3C 454.3 for four epochs. The light blue diamonds represent the $\Phi_{jet}$ values using $B_{1pc}$ with measured CQ core shifts and with $k_r = 1$. If 3C 454.3 harbours a maximally rotating ($a = 1$) black hole, then the source appears to remain near the magnetically arrested disc state in the four observing epochs.

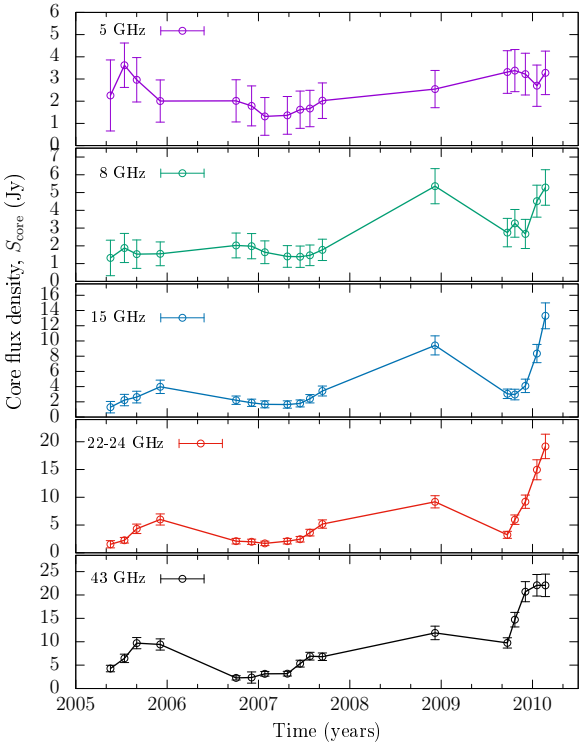


**Fig. 12.** VLBA core flux density of 3C 454.3 at 5, 8, 15, 22–24, and 43 GHz estimated from Gaussian model fitting (see Sect. 3.2). The error bars include the uncertainty on the flux scale, which is 10%.

Chamani et al. (2021) is

$$\Phi_{jet} = 8 \times 10^{33} f(a) [1 + \sigma]^{1/2} \left[\frac{M_{BH}}{10^9 M_\odot}\right] \left[\frac{B_{1pc}}{G}\right] \quad [G\,cm^2], \quad (7)$$

with $a$ the black hole (BH) spin and $f(a) = \frac{1+(1-a^2)^{1/2}}{a}$. Assuming that 3C 454.3 hosts a fast spinning BH ($a = 1$), $f(a) = 1$. Setting the jet magnetization parameter as $\sigma = (\Gamma\theta_j)^2$, the $\Phi_{jet}$ values are readily obtained. We compare the measured $\Phi_{jet}$ values with the predicted magnetic flux threading the BH, $\Phi_{BH}$, at the magnetically arrested disc (MAD) state,

$$\Phi_{BH} = 2.4 \times 10^{34} \left[\frac{\eta}{0.4}\right]^{-1/2} \left[\frac{M_{BH}}{10^9 M_\odot}\right] \left[\frac{L_{acc}}{1.26 \times 10^{47}\,erg\,s^{-1}}\right]^{1/2} \quad (8)$$

given in units of G cm$^2$ (e.g. Tchekhovskoy et al. 2011; Zamaninasab et al. 2014). The parameters $\eta$ and $L_{acc}$ respectively indicate the radiative efficiency of the accretion disc and the accretion disc luminosity.

Figure 11 displays the $\Phi_{jet}$ values for 3C 454.3 for the four epochs that have $k_r = 1$. The plot of the jet's magnetic flux as a function of the accretion luminosity and BH mass was adapted from Zamaninasab et al. (2014) (who assumed $\Gamma\theta_j = 1$). We used the corrections given for radio galaxies ($\Gamma\theta_j \neq 1$) and blazars ($\Gamma\theta_j = 0.13$) presented in Chamani et al. (2021). Our result appears to be very close to the predicted MAD limit, even closer than the measurement given in Zamaninasab et al. (2014).

### 4.5. Light curves and correlation analysis

The long-term light curve of 3C 454.3 at 37 GHz obtained from the Metsähovi Radio Observatory is displayed in Fig. 9. In this period, three remarkable flux density peaks were observed, and they are linked to major gamma-ray flare events such as the one observed on 2009 December 02 (Pacciani et al. 2010).

The core flux density at each frequency as a function of time is shown in Fig. 12. At 43 GHz the core flux density from 2009 to 2010 corresponds to the sum of flux densities of the components Qa and Qb. Due to opacity effects, the 2009 flare starts at 43 GHz and then progresses to lower frequencies; no flux density increase is seen at 5 GHz yet. The first three VLBA observations in 2005 at 22 and 43 GHz bands coincide well with the rising side of the flux at 37 GHz, whereas our last observing epoch in 2005 coincides with the short-lived plateau at 37 GHz. All multi-frequency core flux density observations from mid-2006 to mid-2007 coincide with the low state at 37 GHz. After that, the core flux density increases moderately until January 2008. The last observation in December 2008 coincides with the declining or post-flare phase at 37 GHz. Finally, the last five observations at the 8, 15, 24, and 43 GHz bands from September 2009 to February 2010 coincide with the sudden increase in flux density at 37 GHz. The peak in the 43 GHz core flux density closely matches the 37 GHz peak in January 2010.

To understand the influence of flares on the core shift effect, we explored the possible dependence of the core shift (between a pair of frequencies), $\Delta r_{\nu_1\nu_2}$, the core position, $r_{core}$, with the core flux density, $S_{core}$, and with the total flux density, $S_{MRO}$, at 37 GHz. We calculated Spearman's rank correlation coefficient ($\rho$) and the $p$-value in R; $p$-values below 0.05 are taken as possible correlations and those below 0.01 as correlations (all shown in boldface in Table 5). We also include Pearson's correlation coefficient to evaluate the strength of the possible linear correlations. For the core shift versus core flux density correlations, we used a generic fitting function of the form $\Delta r_{\nu_1\nu_2} \propto S_{core}^t$, where $t$ is the power-law index.

In Figs. 13–17 we present scatter-plots of $\Delta r_{\nu_1\nu_2} - S_{core}$ at each frequency. The scatter-plots are given for the following relationships: $\Delta r_{CX} - S_{core}$ at 5 GHz and 8 GHz, $\Delta r_{XU} - S_{core}$

**Table 5.** Spearman's rank and Pearson correlation coefficients.

| Relations | Spearman | | Pearson | Fitting function |
|---|---|---|---|---|
| | Correlation coefficient ($\rho$) | $p$-value | Correlation coefficient ($r$) | Power-law |
| $\Delta r_{CX} - S_{\rm core}$ at 5 GHz | 0.37 | 0.14 | | |
| $\Delta r_{CX} - S_{\rm core}$ at 8 GHz | 0.19 | 0.46 | | |
| $\Delta r_{XU} - S_{\rm core}$ at 8 GHz | −0.48 | **0.05** | -0.46 | $(0.24 \pm 0.06)\, S_{\rm core}^{-0.7\pm0.3}$ |
| $\Delta r_{XU} - S_{\rm core}$ at 15 GHz | −0.12 | 0.66 | | |
| $\Delta r_{UK} - S_{\rm core}$ at 15 GHz | 0.59 | **0.01** | 0.37 | $(0.05 \pm 0.01)\, S_{\rm core}^{0.3\pm0.2}$ |
| $\Delta r_{UK} - S_{\rm core}$ at 22−24 GHz | 0.60 | **0.01** | 0.40 | $(0.05 \pm 0.01)\, S_{\rm core}^{0.3\pm0.2}$ |
| $\Delta r_{KQ} - S_{\rm core}$ at 22−24 GHz | 0.77 | **0.0003** | 0.60 | $(0.02 \pm 0.01)\, S_{\rm core}^{0.7\pm0.2}$ |
| $\Delta r_{KQ} - S_{\rm core}$ at 43 GHz | 0.64 | **0.006** | 0.71 | $(0.010 \pm 0.004)\, S_{\rm core}^{0.7\pm0.2}$ |
| $\Delta r_{CQ} - S_{\rm MRO}$ at 37 GHz | 0.63 | **0.008** | 0.22 | $(0.3 \pm 0.1)\, S_{\rm core}^{0.2\pm0.2}$ |
| $\Delta r_{CQ} - S_{\rm core}$ at 43 GHz | 0.52 | **0.03** | 0.23 | $(0.35 \pm 0.09)\, S_{\rm core}^{0.1\pm0.1}$ |
| $r_{\rm core} - S_{\rm core}$ at 5 GHz | 0.40 | 0.12 | | |
| $r_{\rm core} - S_{\rm core}$ at 8 GHz | 0.61 | **0.02** $^{(*)}$ | 0.75 | $(58.3 \pm 9.3)\, S_{\rm core}^{0.6\pm0.2}$ |
| $r_{\rm core} - S_{\rm core}$ at 15 GHz | 0.84 | **0.0003** | 0.71 | $(19.3 \pm 2.8)\, S_{\rm core}^{0.6\pm0.1}$ |
| $r_{\rm core} - S_{\rm core}$ at 22−24 GHz | 0.74 | **0.001** | 0.77 | $(7.9 \pm 1.7)\, S_{\rm core}^{0.8\pm0.2}$ |
| $r_{\rm core} - S_{\rm core}$ at 43 GHz | 0.49 | **0.05** | 0.77 | $(2.1 \pm 2.0)\, S_{\rm core}^{0.5\pm0.5}$ |
| $k_r - S_{\rm core}$ at 5 GHz | 0.28 | 0.30 | | |
| $k_r - S_{\rm core}$ at 8 GHz | 0.67 | **0.006** | 0.80 | $(0.55 \pm 0.05)\, S_{\rm core}^{0.5\pm0.1}$<br>$(0.5 \pm 0.1)+(0.15 \pm 0.03)\, S_{\rm core}$ |
| $k_r - S_{\rm core}$ at 15 GHz | 0.44 | 0.12 | 0.74 | |
| $k_r - S_{\rm core}$ at 22−24 GHz | 0.56 | **0.03** | 0.81 | $(0.48 \pm 0.06)\, S_{\rm core}^{0.3\pm0.1}$<br>$(0.6 \pm 0.1)+(0.04 \pm 0.01)\, S_{\rm core}$ |
| $k_r - S_{\rm MRO}$ at 37 GHz | 0.50 | **0.05** | 0.77 | $(0.39 \pm 0.08)\, S_{\rm core}^{0.30\pm0.09}$ $^{(\dagger)}$<br>$(0.5 \pm 0.1)+(0.03 \pm 0.01)\, S_{\rm core}$ |
| $k_r - S_{\rm core}$ at 43 GHz | 0.52 | **0.04** | 0.76 | $(0.52 \pm 0.09)\, S_{\rm core}^{0.21\pm0.09}$ $^{(\dagger)}$<br>$(0.5 \pm 0.1)+(0.04 \pm 0.01)\, S_{\rm core}$ |
| PA − $k_r$ | −0.42 | 0.11 | | |
| Correlations with $B_{\rm 1pc}$ values assuming $k_r$=1 | | | | |
| $B_{\rm CQ,1pc} - S_{\rm core}$ at 5 GHz | 0.54 | **0.03** | 0.47 | |
| $B_{\rm CQ,1pc} - S_{\rm core}$ at 8 GHz | 0.29 | 0.26 | | |
| $B_{\rm CQ,1pc} - S_{\rm core}$ at 15 GHz | 0.56 | **0.02** | 0.05 | |
| $B_{\rm CQ,1pc} - S_{\rm core}$ at 22−24 GHz | 0.61 | **0.01** | 0.12 | |
| $B_{\rm CQ,1pc} - S_{\rm core}$ at 43 GHz | 0.52 | **0.03** | 0.23 | |
| $B_{\rm CQ,1pc} - S_{\rm MRO}$ at 37 GHz | 0.63 | **0.008** | 0.24 | |

**Notes.** Power-law fits are given only for the relations with $p$-values < 0.05. Additional linear fits are provided for the $k_r - S_{\rm core}$ relationship. $^{(*)}$Excluding the data point of 37 pc. $^{(\dagger)}$The fits do not include the data at $k_r = 0.45$ and $k_r = 0.52$. These are taken as outliers in the scatter plots. By including these points, the power-law fits become much less steep with indices: 0.05 ± 0.18 at 37 GHz and 0.04 ± 0.14 at 43 GHz.

at 8 GHz and 15 GHz, $\Delta r_{\rm UK} - S_{\rm core}$ at 15 GHz and 22−24 GHz, and $\Delta r_{\rm KQ} - S_{\rm core}$ at 22−24 GHz and 43 GHz. With regard to $\Delta r_{\rm CX} - S_{\rm core}$ no correlations were found. A negative but weak correlation was obtained for $\Delta r_{\rm XU} - S_{\rm core}$ at 8 GHz, but not at 15 GHz. Positive and moderate correlations were found for $\Delta r_{\rm UK} - S_{\rm core}$ at 15 GHz and 22−24 GHz. A strong correlation was found at the higher frequencies for $\Delta r_{\rm KQ} - S_{\rm core}$ at 22−24 GHz with a power-law index $t = 0.7 \pm 0.2$. A moderate correlation at 43 GHz was also found, although the correlation is less robust than at 22−24 GHz. Additionally, we searched for possible correlations of the full CQ core shift with the core flux at 43 GHz and at 37 GHz. The results suggest possible correlations, although there is not a clear monotonic relationship between the two variables, as seen in Fig. 17.

Figure 18 displays the scatter-plots of the core positions as a function of the core flux at different frequencies, $r_{\rm core}$–$S_{\rm core}$. As is evident from the plots, there is no correlation between the variables at 5 GHz, but there are moderate to strong positive correlations at all the other frequencies. Taking only the strongest correlations at 8, 15, and 22−24 GHz, the fitted power laws have indices from 0.6 to 0.8 with an average of 0.7. This indicates that the core position appears to follow approximately $r_{\rm core} \propto S^{2/3}$

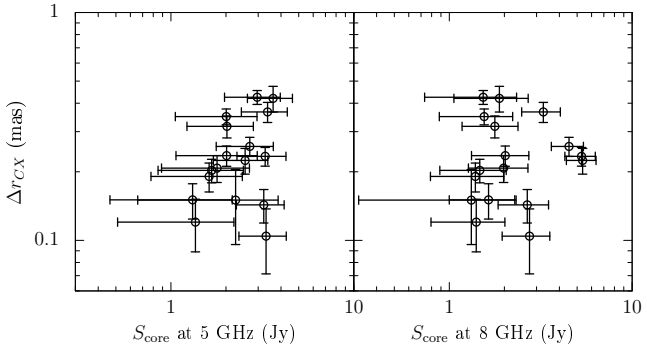


**Fig. 13.** CX core shifts vs core flux density at different frequencies. No correlations are found with the core flux at 5 and 8 GHz.

as expected in the BK79 model if the flares are mainly due to increased particle density (Lobanov 1998; Kovalev et al. 2008). We discuss this in Sect. 5.1.

We also searched for correlations between the index $k_r$ and the core flux density, $k_r - S_{\rm core}$, at all the VLBA frequencies and at 37 GHz, as shown in Fig. 19. A significant correlation was

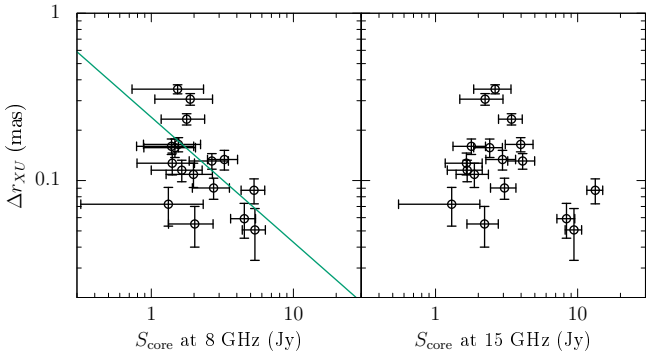


**Fig. 14.** XU core shifts vs. core flux density at different frequencies. A negative correlation with the core flux at 8 GHz is found, but not at 15 GHz. The green line indicates a power-law fit; see Table 5 for further details.

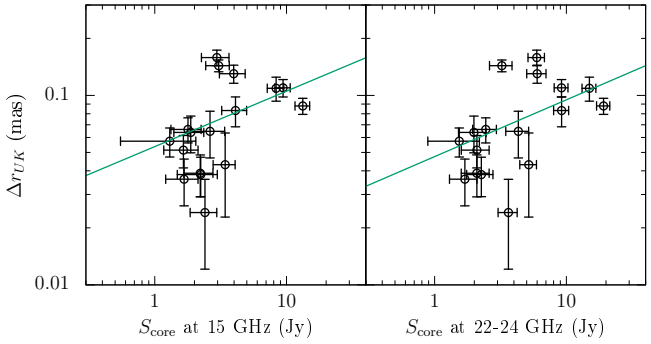


**Fig. 15.** UK core shifts vs. core flux density at different frequencies. Positive correlations are found at 15 and 22−24 GHz. The green line indicates a power-law fit; see Table 5 for further details.

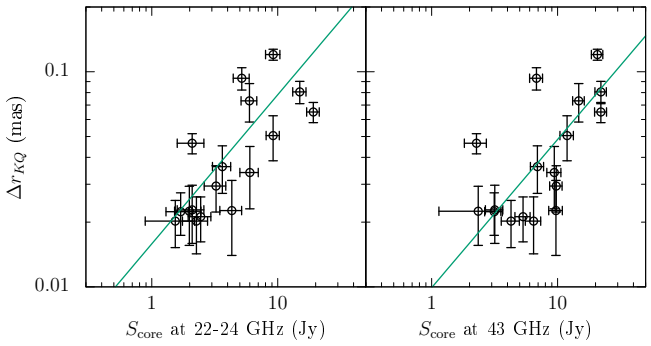


**Fig. 16.** KQ core shifts vs. core flux density at different frequencies. Positive correlations are found at 22−24 and 43 GHz. The green line indicates a power-law fit; see Table 5 for further details.

found at 8 GHz. Possible correlations were found at 22−24, 37, and 43 GHz. In all the cases, the fitted power-law indices are in the range from 0.2 to 0.5 (see Table 5), and the Pearson correlation coefficients are high; therefore, we also fitted the data with a linear function. This interesting new finding may be driven by the flaring behaviour, which is further discussed in Sect. 5.1.

In addition, correlations of index $k_r$ with jet PA have also been investigated. The scatter plot is displayed in Fig. 20. Although the scatter plot appears to show hints of a negative trend for $k_r$ with the PA, there is no statistically significant correlation. Furthermore, correlation studies of jet PA and flux density have also been considered. Still, we have not found evident correlations for the PA − $S_{\rm core}$, PA − $S_{\rm MRO}$ at 37 GHz and PA − $\Delta r$ relationships. In general, the data appears scattered and disordered. A monotonic function cannot describe the relations.

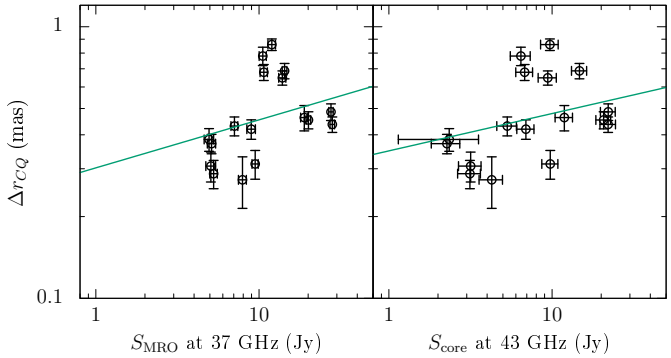


**Fig. 17.** Full CQ core shifts vs. MRO 37 GHz flux density and core flux density at 43 GHz at different frequencies. Positive correlations are found at both frequencies. The green line indicates a power-law fit; see Table 5 for further details.

Finally, for curiosity, we searched for possible correlations of $B_{\rm 1pc}$ with the core flux density and MRO 37 GHz flux density assuming entirely $k_r = 1$. The results show positive Spearman correlation coefficients, although the data do not follow strong monotonic relationships, as seen in the scatter plots of Fig. 21. It is evident from these plots that the $B_{\rm 1pc}$ values are relatively stable at all frequencies. Since we used $k_r = 1$, and the same $\delta$, $\theta$, and $\theta_j$ at all the epochs, $B_{\rm 1pc}$ depends only on $\Omega_{r\nu}$, which in turn depends on $r_{\rm core}$. Hence, the $B_{\rm 1pc} - S_{\rm core}$ correlation is a direct consequence of the $r_{\rm core} - S_{\rm core}$ correlation.

## 5. Discussion

### 5.1. Core shift and flares

In our search for correlations between core shift and core flux density, we found that $r_{\rm core}$ depends approximately on $S_{\rm core}^{0.7}$. This relationship closely matches the theoretical prediction by BK79 that the observed radius, $r_{\rm max,ob}$, where the maximum brightness temperature is achieved, scales with the synchrotron luminosity, $L_{\rm s}$, as $r_{\rm max,ob} \propto L_{\rm s}^{2/3} \propto L_{\rm s}^{0.7}$ and consequently has the same dependence on flux density.

The connection between the core position and core flux density during jet flares has been previously investigated by PL19. They use a phenomenological model of the form $r_{\rm core} = bS_{\rm core}^{K_{\rm rS}}$ and independent of any physical assumptions model the core-shift variability at 2.3/8.4 GHz in a sample of 40 AGN. Using a general time-dependent model, they determine $K_{\rm rS} = 0.28 \pm 0.05$ for the whole sample. Our results show a mean $K_{\rm rS} = 0.7$ for $r_{\rm core} \propto S_{\rm core}^{K_{\rm rS}}$, which differs significantly from the results in PL19. On the other hand, our $\Delta r$ shows a weaker dependence on $S_{\rm core}$ with $K_{\rm rS} = 0.3 \pm 0.2$ at 15 and 22−24 GHz and even a negative $K_{\rm rS}$ at 8 GHz (see Table 5). This discrepancy may be related to (i) varying $k_r$ in our case, (ii) lower observing frequencies used in PL19, or (iii) 3C 454.3 possibly having a behaviour that differs significantly from a typical AGN.

As pointed out by PL19, and references therein, the physical mechanisms producing variations of core flux density can be associated with variations in particle density, magnetic field strength or bulk Doppler factor as $S_{\rm core} \propto N_{\rm core}\, B_{\rm core}^{1-\alpha}\, \delta^{3-\alpha}$, where $\alpha$ is the optically thin spectral index. Thus, flares and consequently core position variations can be due to variations in any of these parameters. PL19 list four basic scenarios for the flares: (i) Flaring emission is in equipartition (i.e. $N_{\rm core} \propto B_{\rm core}^2$)

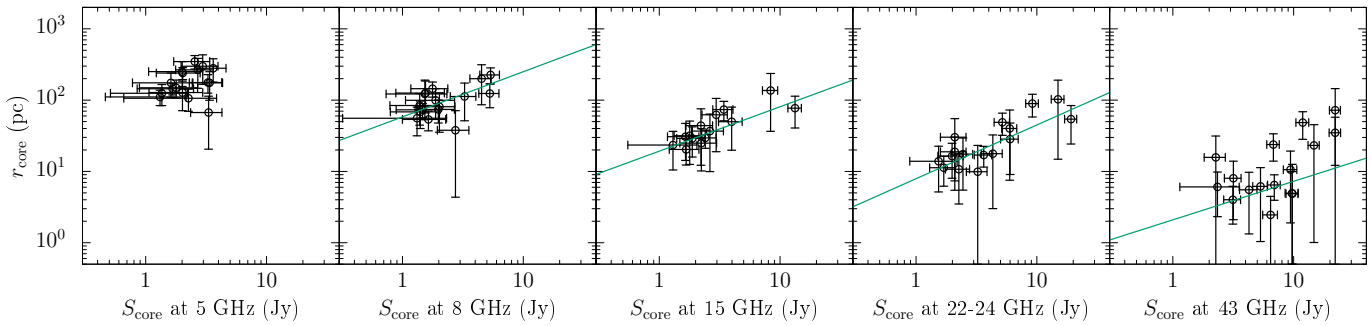


**Fig. 18.** Core position vs. core flux density at different frequencies. Positive correlations are found at 8, 15, 22−24, 43 GHz. The green line indicates a power-law fit; see Table 5 for further details.

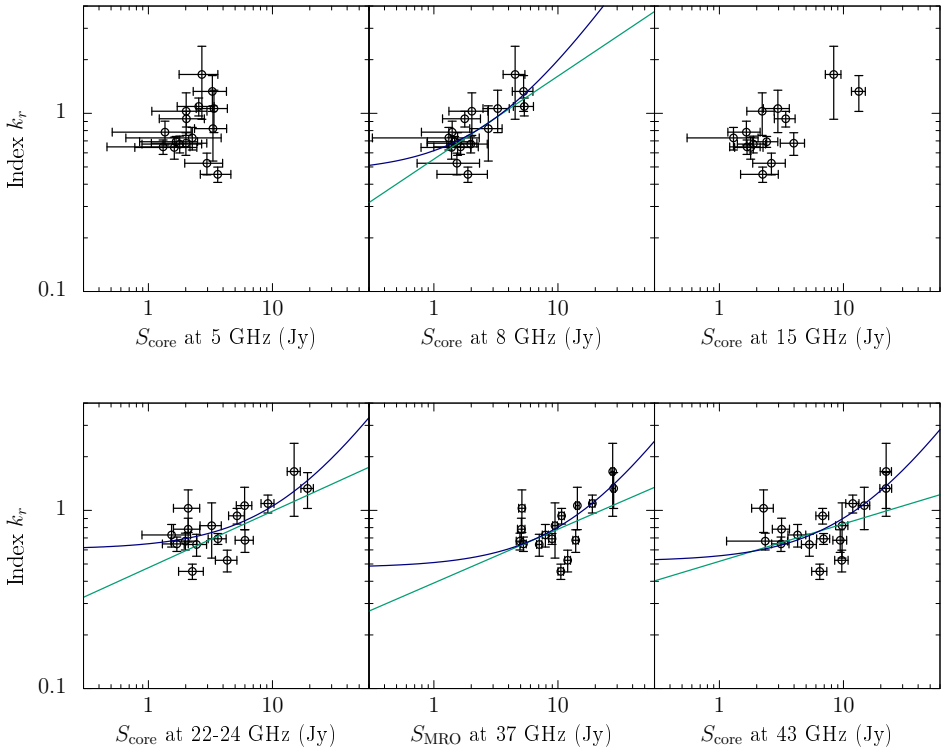


**Fig. 19.** Core-shift index $k_r$ vs. flux density at each frequency. No evident correlation is found at 5 and 15 GHz. Positive and moderate correlations were found at 8, 22−24, 37, and 43 GHz, respectively. Power-law fits are shown with the green line, and linear fits with a blue line. It appears that the $k_r$ index increases modestly when the core flux rises. All fitting parameters are displayed in Table 5.

while $\delta$ is constant; (ii) Flares are mainly due to particle density variability; (iii) Flares are mainly due to variations in magnetic field strength; and (iv) Flares are due to variations in the jet Doppler factor. The fact that $k_r \neq 1$ in 3C 454.3 for most of the observing epochs, also outside of the flaring periods, indicates that the source is unlikely to be in equipartition, making scenario (i) also unlikely. Scenario (ii) is perhaps the simplest case matching our observed relationship $r_{\rm core} \propto S_{\rm core}^{0.7}$ since it gives $r_{\rm core} \propto N_{\rm core}^{2/3} \propto S_{\rm core}^{2/3}$. Scenario (iii) cannot be ruled out. Scenario (iv) appears unlikely since, considering that in blazars in general (Savolainen et al. 2002), and in 3C 454.3 in particular (Jorstad et al. 2010, 2013) the flares are connected to travelling disturbances in the VLBI jet, it is likely that changes in the jet Doppler factor alone do not produce them. Furthermore, $r_{\rm core} \propto \Gamma^{-4/3}\beta^{-2/3}\delta^{2/3}\sin^{-1/3}\theta\, S_{\rm core}^{2/3}$ in BK79, and thus one would expect $K_{\rm rS}$ to differ from 2/3 in scenario (iv). In a general case, both $N_{\rm core}$ and $B_{\rm core}$ likely vary simultaneously (e.g. Niinuma et al. 2015), but results from PL19 and, for example, from Lobanov & Zensus (1999) suggest that variations in $N_{\rm core}$ dominate the flaring behaviour.

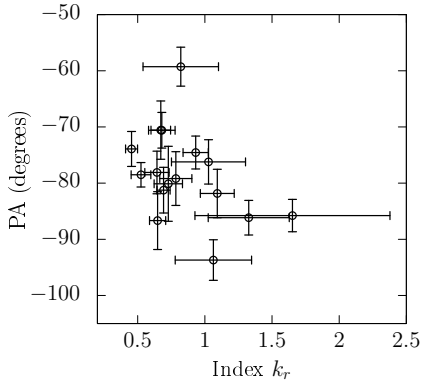


**Fig. 20.** Jet position angle (PA) vs. index $k_r$. The correlation between the variables is very weak, although the negative trend suggests that when $k_r > 1$ the PA values decrease.

### 5.2. Frequency dependence of the core shift

We found that most of the time, the frequency dependence of the core position does not follow $\nu_{\rm obs}^{-1}$ in 3C 454.3. Instead, the

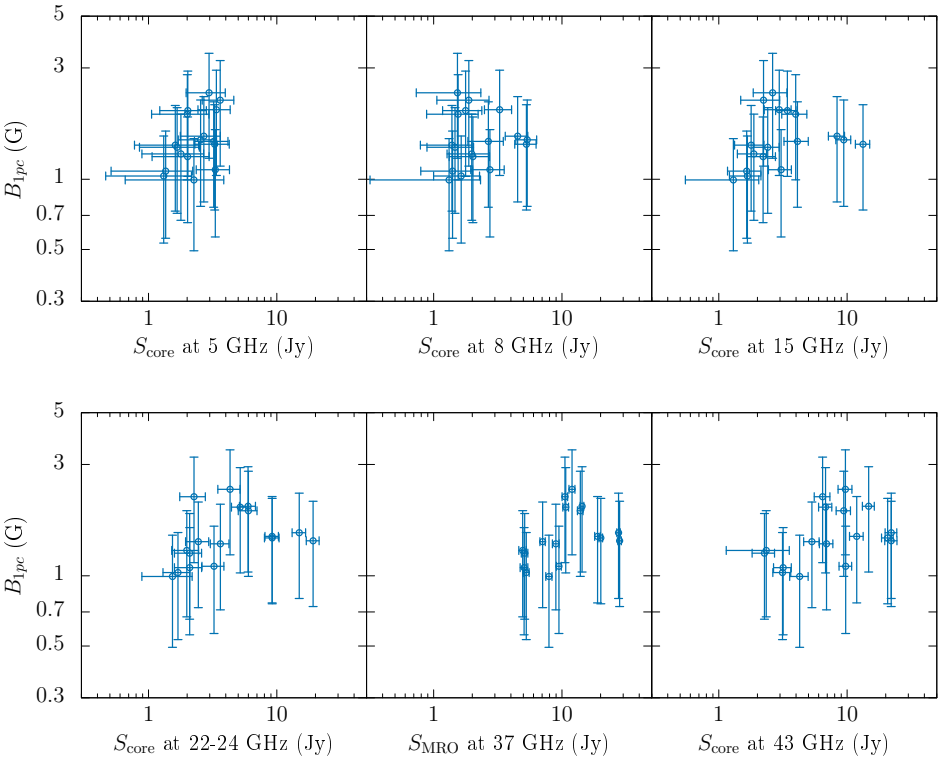


**Fig. 21.** $B_{\rm 1pc}$ as a function of the core flux density. The results are displayed assuming $k_r = 1$ and using CQ core shifts.

index $k_r$ was found to be a variable parameter in the period of our study. We have demonstrated here the variability of $k_r$ by direct measurements using multi-epoch quasi-simultaneous multi-band VLBI data for the first time. Frequency dependence with $k_r < 1$ values were found during flaring and quiescent states. This would mean that either energy equipartition or conical shape assumptions do not always hold or the jet cannot be described by the BK79 model. For a BK79 jet, we might assume that $k_r$ should be close to one and stable in quiescent states. During flaring episodes, the parsec-scale jet would temporarily become particle-dominated and deviation from equipartition would be natural, implying a consequent deviation from $k_r = 1$. This, however, does not seem to be the case in 3C 454.3. Instead, it appears that $k_r$ is *typically* below one in this source.

We note that, in general, core shift and core position measurements can be positively biased due to the use of a Gaussian template, which is only a crude model for the actual jet brightness distribution, and consequently bias the $\nu^{-1/k_r}$ dependence when $k_r \neq 1$ as shown by Pashchenko et al. (2020). Their results show that this bias leads to observed $k_r$ values closer to one than the true $k_r$. Hence, the deviation of $k_r$ from one in 3C 454.3 can be even larger than is observed here.

We note that the large uncertainties of $k_r$ from 2009 to 2010 were produced by the strong flares that disrupted the core-shift effect. The ejection of a new moving feature at 43 GHz led to ambivalence in measuring the $k_r$ parameter, judging by the results demonstrated in Figs. D.14–D.18. In these strong flaring epochs, the core-shift data are not always compatible with a single power-law dependence, which supports the findings of Kutkin et al. (2019) and PL19.

We found a significant correlation of $k_r$ with the core flux density, $S_{\rm core}$, as shown in Fig. 19. The figure shows that the index $k_r$ tends to become larger when the flux density is higher. This effect appears to be steeper and pronounced at 8 GHz ($k_r - S_{\rm core}^{0.5}$) and less pronounced from 22–24 to 43 GHz where the power-law indices range from 0.2 to 0.3. This would mean that dependence of the core position on frequency ($\nu^{-1/k_r}$) is less steep when flux density is higher. This could be explained by the fact that flares start at high frequencies, affecting the core shift first at the high-frequency end of the spectrum and later at the low frequencies. Furthermore, if the KQ core shift first increases due to a higher particle density while the lower frequency core position remains the same (since the flare has not yet propagated there), this could make $k_r$ look larger. For example, Fig. D.16 shows a situation in which the shift between 24 GHz and 43 GHz is suddenly very large during the rising part of a large flare. This effect agrees well with the flaring jet model presented by PL19. More observations are necessary to closely follow changes in the core position at different frequencies and, consequently, $k_r$ during pre-flare, peak, and post-flare, and also extensive observations during quiescent states. Furthermore, it is important to note that the increase in $k_r$ with flux density has also been observed in 3C 345 at 14.5 GHz for a few observing epochs (Kudryavtseva et al. 2011).

### 5.3. Consequences to the magnetic field estimation

Significant deviations of $k_r$ from one imply that this parameter can also be variable in other radio sources. This should be considered when measuring magnetic field strengths using just a pair of frequencies and assuming a priori $k_r = 1$. In general, having three or more frequencies in core-shift measurements in order to verify the $k_r = 1$ condition is important if these measurements are used to calculate magnetic field strengths. Furthermore, making the measurements outside of flaring periods is likely to yield 'undisturbed' core-shift measurements.

A key problem found in this study is the large differences in $B_{\rm 1pc}$ with $k_r = 1$ and $k_r \neq 1$. Using the same formula for both cases indicates that the current expression for $B_{\rm 1pc}$ is not applicable and fails for high or low $k_r$ values. This is not surprising since the deviations from $k_r = 1$ indicate that one of the assumptions used to derive $B_{\rm 1pc}$ does not hold. The expression

for $B_{1\mathrm{pc}}$ in equipartition with a conical jet holds strictly as long as $k_r$ is near one. When $k_r = 1$ epochs are selected, the magnetic field estimates are quite consistent, even though the amount of core shift varies significantly with time.

Since the equipartition expression for $B_{1\mathrm{pc}}$ does not hold when measured $k_r$ is different from one, we should consider measuring the magnetic field strength by incorporating the core flux density in the core-shift measurements, as done by Zdziarski et al. (2015), or by measuring the synchrotron self-absorption turnover frequency and turnover flux density of a resolved jet (Marscher 1983; Savolainen et al. 2008a). In both cases, we can estimate the magnetic field strength without assuming equipartition. The known downside of these approaches is the high sensitivity of the derived magnetic field values to the accuracy of the measured quantities. In 3C 454.3, the core spectrum is inverted in nearly all observations, which in most cases does not constrain well the turnover frequency (see the results in Appendix D).

### 5.4. Consequences to astrometry and geodetic VLBI

High-accuracy astrometric VLBI measurements of extragalactic radio sources are the basis of the International Celestial Reference Frame (ICRF). In its third realization (ICRF3; Charlot et al. 2020) and in the independently produced Radio Fundamental Catalog (RFC[4]), the absolute source positions are measured at submilliarcsecond accuracy. Together with other space geodetic techniques, VLBI is also essential for realizing the International Terrestrial Reference Frame (ITRF) and obtaining the full set of Earth Orientation Parameters that provide a link between the ITRF and the ICRF (e.g. Petrov et al. 2009). In astrometric and geodetic VLBI observations, core shift adds another frequency-dependent phase term (Kovalev et al. 2008) that behaves like an extra path through a dispersive medium. Porcas (2009) showed that if $k_r = 1$, the contribution of the core shift to the measured *group delays* is, in fact, zero, and the source coordinates derived from the group delays refer to the jet base, a fiducial point upstream of the core. If $k_r \neq 1$, this is not the case, and the core-shift-induced group delays are non-zero. On the other hand, the coordinates measured from the single-band *phase delays* refer to the position of the radio emission at the given observing band and always depend on the core shift.

As PL19 point out, the core shift *variability* can affect the astrometric measurements using the group delays, even if formally $k_r = 1$ and strong flares can disrupt any regular frequency dependence of $k_r$. Our results further show that in 3C 454.3 $k_r \neq 1$ even during quiescent periods (i.e. the core shift can affect the measured group delays even outside of the flaring periods in this source). Therefore, unless 3C 454.3 is an exceptional case, knowing the core shift, including the actual $k_r$, is important for improving the accuracy of VLBI astrometry. The significant core-shift variability observed here and in PL19 indicates that ideally, the core shift in the ICRF3 defining sources should be regularly monitored.

Several studies have established that systematic effects due to the non-point-like structure of extragalactic radio sources are currently the major source of errors in geodetic VLBI measurements (e.g. Xu et al. 2017, 2021a; Anderson & Xu 2018; Bolotin et al. 2019). With the advent of the new broad-band (four 512 MHz wide bands over 2−14 GHz) observing system known as VGOS (VLBI Global Observing System; Niell et al. 2018), the source structure effects now dominate the thermal errors by about an order of magnitude and are of the same order or larger than the errors due to uncertainties in the atmospheric modelling (Xu et al. 2021a). VGOS has an ambitious goal of 1 mm accuracy for the station positions on the ground, which translates to ∼30 μas accuracy of the source positions in the sky. Therefore, it is clear that accurate modelling of the time and frequency-dependent source structure is crucial for VGOS. This has led to active efforts to remove the source structure effects by imaging the geodetic VLBI data at the four bands of the VGOS (Xu et al. 2021c). In order to use these images to correct the visibility data, it is necessary to align them accurately, which amounts to determining the core-shift effect. Our results presented in this paper directly demonstrate the variability of the magnitude of the core shift that was shown in PL19 and the variability of $k_r$ which PL19 deduced from a model analysis of two-frequency core-shift time series. The former means that core shift should also be regularly monitored for the geodetic VLBI purposes, and preferably at more than two frequencies. The latter should be taken into account when attempting, for example, to fit the core shift to the geodetic VLBI measurements: an a priori assumption of $k_r = 1$ may not always hold.

Finally, we comment on the offsets between the optical and radio positions of AGN. The European Space Agency's astrometry mission *Gaia* has recently provided submilliarcsecond positions in optical band (Gaia Collaboration 2021) for well over a billion celestial sources with a limiting magnitude of $G \approx 21$. While a good overall agreement exists between the ICRF3 and RFC radio positions and the *Gaia* optical positions, statistically significant offsets are seen for about 10% of the matching AGN (e.g. Petrov & Kovalev 2017a,b; Gaia Collaboration 2018; Petrov et al. 2019). Kovalev et al. (2017) found that the significant VLBI-*Gaia* offsets are preferentially parallel to the direction of the radio jet. This result was later confirmed and studied by Plavin et al. (2019a), Kovalev et al. (2020), and Xu et al. (2021b), among others. The offsets, therefore, constitute a genuine astrophysical effect and core shift; the source structure can also contribute to this effect, at least in some cases (Petrov & Kovalev 2017b). If $k_r \neq 1$, as we report here for 3C 454.3, the radio source position derived from the group delays does not correspond to the jet base, and one can have an offset from the nucleus-dominated optical position. On the other hand, if the optical emission is dominated by the jet, offsets are also expected for the $k_r = 1$ case, but in the opposite direction (Kovalev et al. 2017; Plavin et al. 2019a). Knowing both the amount of the core shift as well as its time and frequency dependence is useful for interpreting the offsets and highlights the importance of such measurements.

## 6. Summary and conclusions

The core-shift effect has been broadly used for a variety of studies which include jet geometry (e.g. Pushkarev et al. 2018), astrometry, and estimation of particle densities, magnetic field strengths, and magnetic fluxes in a broad range of AGN (e.g. Pushkarev et al. 2012; Zamaninasab et al. 2014; PL19). These studies have been made possible by employing the VLBI technique that allows the highest angular resolution measurements. Identifying the surface where the opacity is near unity is essential for locating the core and measuring the core shift.

We studied the time variability of the core-shift effect in the jet of 3C 454.3 by analysing multi-epoch and multi-frequency VLBA data from 2005 to 2010 (19 epochs). Core-shift measurements were performed for the following adjacent frequency bands: CX (5 GHz and 8 GHz), XU (8 GHz and 15 GHz), UK

[4] http://astrogeo.org/rfc/

(15 GHz and 22−24 GHz), KQ (22−24 GHz and 43 GHz). These data allowed us to examine the time variability of the core shift and core-shift index, $k_r$, for the first time. The current study found significant variability of the core shift from 0.27 mas up to 0.86 mas for the frequencies between 5 and 43 GHz.

Investigation of the variable nature of the core-shift effect was carried out previously by PL19, who found significant core-shift variability in a sample of 40 sources (not including 3C 454.3), although only between two frequencies, 2 GHz and 8 GHz. In this paper we confirm the time variability of the core-shift effect found by PL19 and present for the first time direct evidence of the variability of the index $k_r$. We found significant deviations from the ideal Blandford & Königl conical jet in equipartition ($k_r = 1$). The full range of measured $k_r$ values goes from 0.45 to 1.7. The large values are, however, related to the flaring period in 2009−2010 and have large uncertainties. Typically $k_r$ was below one with a mean value of $k_r = 0.85 \pm 0.08$ for the entire study period.

The disorder of the core shifts in the observations from late 2009 to the beginning of 2010 is attributable to the strong outbursts that took place in that period (Pacciani et al. 2010). Such a substantial variability of the core shift connected with nuclear flares was also observed by PL19. In addition to this, the emergence of a new moving feature detected at 43 GHz has also shifted the core position, hampering the accurate localization of the core. These disturbances introduce additional shifts at the high frequencies, hindering accurate estimations of the $k_r$ indices. The nuclear region model fitting at 43 GHz revealed that the new feature was moving in the direction of the jet at an apparent speed of $\beta_{\rm app} = 5.0 \pm 1.0$ from 2009 September 22 to 2010 February 21.

Using core-shift measurements and the expression for the magnetic field strength at one parsec in equipartition, we estimated $B_{\rm 1pc}$ when $k_r = 1$ and $k_r \neq 1$. The results showed significant discrepancies, which highlights the importance of first observationally validating the equipartition assumption before using the core-shift measurements to obtain magnetic field strength estimates. Thus, $B_{\rm 1pc}$ values were calculated only for the observations when $k_r$ was close to one, leading to $B_{\rm 1pc}$ values that ranged from 1.3 G to 2.0 G. Subsequently, we estimated the magnetic flux of 3C 454.3. We found that the source was in the MAD state, which agrees with Zamaninasab et al. (2014).

To identify a link between the core-shift effect and outbursts, we searched for correlations between the core shift, core flux density, and the 37 GHz total flux density from single-dish observations. We generally encountered a good correlation of the UK core shift with the core flux density at 15 and 22−24 GHz and the KQ core shift with the core flux density at 22−24 and 43 GHz. A good correlation was also found for the full CQ core shift with the single-dish flux density at 37 GHz and core flux density at 43 GHz. The relationships follow a generic power law as $\Delta r_{\nu_1\nu_2} \propto S^t_{\rm core}$, with $t$ ranging from 0.1 to 0.7. A large index of 0.7 was found for the high-frequency pair, KQ. Hence, there seems to be a tendency of increasing dependence between core shift and flux density. The relationship becomes steeper for the higher frequency pair, which suggests that strong flares increase the core shift at high frequencies.

We also found correlations between the core position (at a given frequency) and the core flux, $r_{\rm core} - S_{\rm core}$. At most frequencies except at 5 GHz, there are moderate to strong positive correlations between the variables. The data can be fitted well by a power law with indices ranging from 0.6 to 0.8 (for 8, 15 and 22−24 GHz) and with a mean of 0.7. This matches closely the $r_{\rm core} \propto S^{2/3}_{\rm core}$ relationship predicted for a Blandford & Königl type jet when flares are due to changes in particle density (or magnetic field strength).

An interesting finding is the correlation of the $k_r$ index with core flux density: $k_r$ tends to increase as the source flares. This would mean that extreme and drastic outbursts in 3C 454.3 tend to increase the core shift at the high frequencies. On the other hand, we did not find any evident correlation between the jet PA and $k_r$.

The present study suggests that full multi-frequency core-shift measurements should be carried out to measure $k_r$ before assuming a priori anything about equipartition for the calculation of $B_{\rm 1pc}$, for example, since deviations from $k_r = 1$ indicate that the assumptions of Eq. (6) may not hold, and this can affect the jet's magnetic field strength calculations.

*Acknowledgements.* We thank Ming H. Xu for useful discussions regarding the astrometric aspects of the core-shift effect. This work was partly supported by the Academy of Finland under the project "Physics of Black Hole Powered Jets" (numbers 274477, 284495, and 312496) and the project "NT-VGOS" (number 315721). YYK is supported in the framework of the State project "Science" by the Ministry of Science and Higher Education of the Russian Federation under contract 075-15-2020-778. The Very Long Baseline Array and the National Radio Astronomy Observatory are facilities of the National Science Foundation operated under a cooperative agreement by Associated Universities, Inc. This work made use of the Swinburne University of Technology software correlator (Deller et al. 2011), developed as part of the Australian Major National Research Facilities Programme and operated under licence. This paper has made use of data from the MOJAVE database that is maintained by the MOJAVE team (Lister et al. 2018) and data obtained at Metsähovi Radio Observatory, operated by Aalto University in Finland.

## References

Abdo, A. A., Ackermann, M., Ajello, M., et al. 2009, ApJ, 699, 817
Abdo, A. A., Ackermann, M., Ajello, M., et al. 2011, ApJ, 733, L26
Ackermann, M., Ajello, M., Baldini, L., et al. 2010, ApJ, 721, 1383
Algaba, J.-C., Hodgson, J., Kang, S.-C., et al. 2019, J. Korean Astron. Soc., 52, 31
Anderson, J. M., & Xu, M. H. 2018, J. Geophys. Res. (Solid Earth), 123, 10162
Blandford, R. D., & Königl, A. 1979, ApJ, 232, 34
Bolotin, S., Baver, K., Bolotina, O., et al. 2019, in Proceedings of the 24th European VLBI Group for Geodesy and Astrometry Working Meeting, eds. R. Haas, S. Garcia-Espada, & J. A. López Fernández, 24, 224
Bonnoli, G., Ghisellini, G., Foschini, L., Tavecchio, F., & Ghirlanda, G. 2011, MNRAS, 410, 368
Britzen, S., Qian, S.-J., Witzel, A., et al. 2013, A&A, 557, A37
Chamani, W., Savolainen, T., Hada, K., & Xu, M. H. 2021, A&A, 652, A14
Charlot, P., Jacobs, C. S., Gordon, D., et al. 2020, A&A, 644, A159
Croke, S. M., & Gabuzda, D. C. 2008, MNRAS, 386, 619
Deller, A. T., Brisken, W. F., Phillips, C. J., et al. 2011, PASP, 123, 275
Donnarumma, I., Pucella, G., Vittorini, V., et al. 2009, ApJ, 707, 1115
Fromm, C. M., Ros, E., Savolainen, T., et al. 2010, in Fermi meets Jansky - AGN in Radio and Gamma Rays. Proceedings of a Workshop held 21–23 June 2010 at the Max-Planck-Institut f. Radioastronomie, Bonn, Germany, eds. T. Savolainen, R. W. Porcas, J. A. Zensus, et al. (Bonn: Max-Planck-Institut for Radioastronomie)
Fromm, C. M., Ros, E., Perucho, M., et al. 2013a, A&A, 551, A32
Fromm, C. M., Ros, E., Perucho, M., et al. 2013b, A&A, 557, A105
Fromm, C. M., Perucho, M., Ros, E., Savolainen, T., & Zensus, J. A. 2015, A&A, 576, A43
Gaia Collaboration (Mignard, F., et al.) 2018, A&A, 616, A14
Gaia Collaboration (Brown, A. G. A., et al.) 2021, A&A, 649, A1
Ghisellini, G., Foschini, L., Tavecchio, F., & Pian, E. 2007, MNRAS, 382, L82
Giommi, P., Blustin, A. J., Capalbi, M., et al. 2006, A&A, 456, 911
Greisen, E. W. 2003, Astrophys. Space Sci. Lib., 285, 109
Hada, K., Doi, A., Kino, M., et al. 2011, Nature, 477, 185
Hirotani, K. 2005, ApJ, 619, 73
Hodgson, J. A., Krichbaum, T. P., Marscher, A. P., et al. 2017, A&A, 597, A80
Homan, D. C., Cohen, M. H., Hovatta, T., et al. 2021, ApJ, 923, 67
Hovatta, T., Lister, M. L., Aller, M. F., et al. 2012, AJ, 144, 105
Hu, W., Yan, D., & Hu, Q. 2021, MNRAS, 503, 2523
Jackson, N., & Browne, I. W. A. 1991, MNRAS, 250, 414
Jorstad, S. G., Marscher, A. P., Lister, M. L., et al. 2005, AJ, 130, 1418

Jorstad, S. G., Marscher, A. P., Larionov, V. M., et al. 2010, ApJ, 715, 362
Jorstad, S. G., Marscher, A. P., Smith, P. S., et al. 2013, ApJ, 773, 147
Komatsu, E., Dunkley, J., Nolta, M. R., et al. 2009, ApJS, 180, 330
Königl, A. 1981, ApJ, 243, 700
Kovalev, Y. Y., Lobanov, A. P., Pushkarev, A. B., & Zensus, J. A. 2008, A&A, 483, 759
Kovalev, Y. Y., Petrov, L., & Plavin, A. V. 2017, A&A, 598, L1
Kovalev, Y. Y., Zobnina, D. I., Plavin, A. V., & Blinov, D. 2020, MNRAS, 493, L54
Kravchenko, E. V., Kovalev, Y. Y., Hovatta, T., & Ramakrishnan, V. 2016, MNRAS, 462, 2747
Kudryavtseva, N. A., Gabuzda, D. C., Aller, M. F., & Aller, H. D. 2011, MNRAS, 415, 1631
Kutkin, A. M., Sokolovsky, K. V., Lisakov, M. M., et al. 2014, MNRAS, 437, 3396
Kutkin, A. M., Pashchenko, I. N., Sokolovsky, K. V., et al. 2019, MNRAS, 486, 430
Lisakov, M. M., Kovalev, Y. Y., Savolainen, T., Hovatta, T., & Kutkin, A. M. 2017, MNRAS, 468, 4478
Lister, M. L., Aller, H. D., Aller, M. F., et al. 2009, AJ, 137, 3718
Lister, M. L., Aller, M. F., Aller, H. D., et al. 2018, ApJS, 234, 12
Lobanov, A. P. 1998, A&A, 330, 79
Lobanov, A. P., & Zensus, J. A. 1999, ApJ, 521, 509
Marcaide, J. M., & Shapiro, I. I. 1984, ApJ, 276, 56
Marscher, A. P. 1983, ApJ, 264, 296
Marscher, A. 2010, in The Jet Paradigm: From Microquasars to Quasars, ed. T. Belloni (Berlin, Heidelberg: Springer), 173
McKinney, J. C., Tchekhovskoy, A., & Blandford, R. D. 2012, MNRAS, 423, 3083
Mohan, P., Agarwal, A., Mangalam, A., et al. 2015, MNRAS, 452, 2004
Narayan, R., Igumenshchev, I. V., & Abramowicz, M. A. 2003, PASJ, 55, L69
Niell, A., Barrett, J., Burns, A., et al. 2018, Radio Sci., 53, 1269
Niinuma, K., Kino, M., Doi, A., et al. 2015, ApJ, 807, L14
O'Sullivan, S. P., & Gabuzda, D. C. 2009, MNRAS, 400, 26
Pacciani, L., Vittorini, V., Tavani, M., et al. 2010, ApJ, 716, L170
Pashchenko, I. N., Plavin, A. V., Kutkin, A. M., & Kovalev, Y. Y. 2020, MNRAS, 499, 4515
Pauliny-Toth, I. I. K., Porcas, R. W., Zensus, J. A., et al. 1987, Nature, 328, 778
Petrov, L., & Kovalev, Y. Y. 2017a, MNRAS, 467, L71
Petrov, L., & Kovalev, Y. Y. 2017b, MNRAS, 471, 3775
Petrov, L., Gordon, D., Gipson, J., et al. 2009, J. Geodesy, 83, 859
Petrov, L., Kovalev, Y. Y., & Plavin, A. V. 2019, MNRAS, 482, 3023
Pian, E., Foschini, L., Beckmann, V., et al. 2006, A&A, 449, L21
Plavin, A. V., Kovalev, Y. Y., & Petrov, L. Y. 2019a, ApJ, 871, 143
Plavin, A. V., Kovalev, Y. Y., Pushkarev, A. B., & Lobanov, A. P. 2019b, MNRAS, 485, 1822
Porcas, R. W. 2009, A&A, 505, L1
Pushkarev, A. B., Hovatta, T., Kovalev, Y. Y., et al. 2012, A&A, 545, A113
Pushkarev, A. B., Butuzova, M. S., Kovalev, Y. Y., & Hovatta, T. 2018, MNRAS, 482, 2336
Qian, S. J., Britzen, S., Krichbaum, T. P., & Witzel, A. 2021, A&A, 653, A7
Raiteri, C. M., Villata, M., Larionov, V. M., et al. 2008, A&A, 491, 755
Raiteri, C. M., Villata, M., Aller, M. F., et al. 2011, A&A, 534, A87
Remillard, R. 2005, ATel, 484, 1
Sargent, W. L. W., Steidel, C. C., & Boksenberg, A. 1988, ApJ, 334, 22
Sarkar, A., Chitnis, V. R., Gupta, A. C., et al. 2019, ApJ, 887, 185
Savolainen, T., Wiik, K., Valtaoja, E., Jorstad, S. G., & Marscher, A. P. 2002, A&A, 394, 851
Savolainen, T., Wiik, K., Valtaoja, E., & Tornikoski, M. 2008a, ASP Conf. Ser., 386, 451
Savolainen, T., Wiik, K., Valtaoja, E., & Tornikoski, M. 2008b, The role of VLBI in the Golden Age for Radio Astronomy, 9, 9
Sharma, R., Massi, H., & Torricelli-Ciamponi, G. 2022, A&A, 660, A58
Shepherd, M. C. 1997, ASP Conf. Ser., 125, 77
Sokolovsky, K. V., Kovalev, Y. Y., Pushkarev, A. B., & Lobanov, A. P. 2011, A&A, 532, A38
Tchekhovskoy, A. 2015, Astrophys. Space Sci. Lib., 414, 45
Tchekhovskoy, A., Narayan, R., & McKinney, J. C. 2011, MNRAS, 418, L79
Teräsranta, H., Tornikoski, M., Mujunen, A., et al. 1998, A&AS, 132, 305
Vercellone, S., Chen, A. W., Vittorini, V., et al. 2009, ApJ, 690, 1018
Vercellone, S., D'Ammando, F., Vittorini, V., et al. 2010, ApJ, 712, 405
Villata, M., Raiteri, C. M., Balonek, T. J., et al. 2006, A&A, 453, 817
Voitsik, P. A., Pushkarev, A. B., Kovalev, Y. Y., et al. 2018, Astron. Rep., 62, 787
Volvach, A. E., Volvach, L. N., & Larionov, M. G. 2021, A&A, 648, A27
Walker, R. C., Dhawan, V., Romney, J. D., Kellermann, K. I., & Vermeulen, R. C. 2000, ApJ, 530, 233
Wright, E. L. 2006, PASP, 118, 1711
Xu, M. H., Heinkelmann, R., Anderson, J. M., et al. 2017, J. Geodesy, 91, 767
Xu, M. H., Anderson, J. M., Heinkelmann, R., et al. 2021a, J. Geodesy, 95, 51
Xu, M. H., Lunz, S., Anderson, J. M., et al. 2021b, A&A, 647, A189
Xu, M. H., Savolainen, T., Zubko, N., et al. 2021c, J. Geophys. Res. (Solid Earth), 126, e21238
Zamaninasab, M., Savolainen, T., Clausen-Brown, E., et al. 2013, MNRAS, 436, 3341
Zamaninasab, M., Clausen-Brown, E., Savolainen, T., & Tchekhovskoy, A. 2014, Nature, 510, 126
Zdziarski, A. A., Sikora, M., Pjanka, P., & Tchekhovskoy, A. 2015, MNRAS, 451, 927

## Appendix A: Core-shift magnitudes

**Table A.1.** Core-shift values per epoch and frequency pair.

| Date | Frequency pair | R.A. (mas) | Dec (mas) | Absolute values (mas) | Projected absolute values (mas) |
|---|---|---|---|---|---|
| 2005-05-19[a] | CX | −0.15 ± 0.06 | 0.03 ± 0.07 | 0.15 ± 0.06 | 0.15 ± 0.06 |
| | XU | −0.06 ± 0.02 | −0.04 ± 0.02 | 0.07 ± 0.02 | 0.06 ± 0.03 |
| | UK | −0.04 ± 0.01 | 0.04 ± 0.01 | 0.06 ± 0.01 | 0.05 ± 0.02 |
| | KQ | −0.020 ± 0.005 | −0.003 ± 0.005 | 0.020 ± 0.005 | 0.020 ± 0.005 |
| | CQ | −0.27 ± 0.06 | 0.03 ± 0.07 | 0.27 ± 0.06 | 0.27 ± 0.06 |
| 2005-07-14[a] | CX | −0.42 ± 0.06 | 0.04 ± 0.07 | 0.42 ± 0.06 | 0.42 ± 0.06 |
| | XU | −0.29 ± 0.03 | 0.10 ± 0.02 | 0.31 ± 0.03 | 0.30 ± 0.03 |
| | UK | −0.04 ± 0.01 | 0.004 ± 0.009 | 0.04 ± 0.01 | 0.04 ± 0.01 |
| | KQ | −0.020 ± 0.006 | 0.003 ± 0.005 | 0.020 ± 0.006 | 0.020 ± 0.006 |
| | CQ | −0.77 ± 0.06 | 0.15 ± 0.07 | 0.78 ± 0.06 | 0.78 ± 0.06 |
| 2005-09-01[a] | CX | −0.41 ± 0.03 | 0.10 ± 0.03 | 0.42 ± 0.03 | 0.42 ± 0.03 |
| | XU | −0.35 ± 0.02 | 0.06 ± 0.02 | 0.35 ± 0.02 | 0.35 ± 0.02 |
| | UK | −0.06 ± 0.02 | 0.01 ± 0.01 | 0.06 ± 0.02 | 0.06 ± 0.02 |
| | KQ | −0.02 ± 0.01 | 0.02 ± 0.01 | 0.02 ± 0.01 | 0.02 ± 0.01 |
| | CQ | −0.84 ± 0.04 | 0.18 ± 0.04 | 0.86 ± 0.04 | 0.86 ± 0.04 |
| 2005-12-04[b] | CX | −0.34 ± 0.03 | 0.07 ± 0.03 | 0.35 ± 0.03 | 0.35 ± 0.03 |
| | XU | −0.16 ± 0.02 | 0.01 ± 0.02 | 0.16 ± 0.02 | 0.16 ± 0.02 |
| | UK | −0.09 ± 0.02 | 0.09 ± 0.01 | 0.13 ± 0.02 | 0.12 ± 0.02 |
| | KQ | −0.02 ± 0.02 | 0.03 ± 0.01 | 0.03 ± 0.01 | 0.02 ± 0.02 |
| | CQ | −0.62 ± 0.04 | 0.20 ± 0.04 | 0.65 ± 0.04 | 0.65 ± 0.04 |
| 2006-10-02[b] | CX | −0.23 ± 0.03 | 0.07 ± 0.03 | 0.24 ± 0.03 | 0.24 ± 0.03 |
| | XU | −0.06 ± 0.02 | −0.001 ± 0.017 | 0.06 ± 0.02 | 0.05 ± 0.02 |
| | UK | −0.03 ± 0.01 | 0.02 ± 0.01 | 0.04 ± 0.01 | 0.04 ± 0.01 |
| | KQ | −0.046 ± 0.005 | 0.007 ± 0.005 | 0.046 ± 0.005 | 0.046 ± 0.005 |
| | CQ | −0.36 ± 0.03 | 0.09 ± 0.03 | 0.37 ± 0.03 | 0.37 ± 0.03 |
| 2006-12-04 | CX | −0.19 ± 0.03 | 0.09 ± 0.03 | 0.21 ± 0.03 | 0.21 ± 0.03 |
| | XU | −0.11 ± 0.02 | −0.01 ± 0.02 | 0.11 ± 0.02 | 0.10 ± 0.02 |
| | UK | −0.05 ± 0.02 | 0.04 ± 0.02 | 0.06 ± 0.02 | 0.06 ± 0.02 |
| | KQ | −0.021 ± 0.007 | 0.008 ± 0.006 | 0.02 ± 0.01 | 0.02 ± 0.01 |
| | CQ | −0.36 ± 0.04 | 0.13 ± 0.04 | 0.38 ± 0.04 | 0.38 ± 0.04 |
| 2007-01-26[b] | CX | −0.11 ± 0.03 | 0.11 ± 0.03 | 0.15 ± 0.03 | 0.13 ± 0.03 |
| | XU | −0.11 ± 0.02 | −0.02 ± 0.02 | 0.12 ± 0.02 | 0.10 ± 0.02 |
| | UK | −0.04 ± 0.01 | 0.01 ± 0.01 | 0.04 ± 0.01 | 0.04 ± 0.01 |
| | KQ | −0.020 ± 0.005 | −0.010 ± 0.005 | 0.022 ± 0.005 | 0.016 ± 0.005 |
| | CQ | −0.28 ± 0.04 | 0.08 ± 0.03 | 0.29 ± 0.04 | 0.29 ± 0.04 |
| 2007-04-26[b] | CX | −0.09 ± 0.03 | 0.08 ± 0.03 | 0.12 ± 0.03 | 0.11 ± 0.04 |
| | XU | −0.13 ± 0.02 | −0.001 ± 0.014 | 0.13 ± 0.02 | 0.12 ± 0.02 |
| | UK | −0.05 ± 0.01 | 0.02 ± 0.01 | 0.05 ± 0.01 | 0.05 ± 0.01 |
| | KQ | −0.022 ± 0.007 | 0.006 ± 0.005 | 0.023 ± 0.007 | 0.023 ± 0.007 |
| | CQ | −0.29 ± 0.04 | 0.10 ± 0.04 | 0.31 ± 0.04 | 0.31 ± 0.04 |
| 2007-06-16 | CX | −0.18 ± 0.03 | 0.08 ± 0.03 | 0.19 ± 0.03 | 0.19 ± 0.03 |
| | XU | −0.16 ± 0.02 | 0.006 ± 0.015 | 0.16 ± 0.02 | 0.16 ± 0.02 |
| | UK | −0.06 ± 0.01 | 0.02 ± 0.01 | 0.07 ± 0.01 | 0.07 ± 0.01 |
| | KQ | −0.020 ± 0.005 | 0.007 ± 0.005 | 0.021 ± 0.005 | 0.021 ± 0.005 |
| | CQ | −0.42 ± 0.04 | 0.11 ± 0.03 | 0.43 ± 0.04 | 0.43 ± 0.04 |
| 2007-07-25[b] | CX | −0.20 ± 0.03 | 0.03 ± 0.03 | 0.20 ± 0.03 | 0.20 ± 0.03 |
| | XU | −0.16 ± 0.02 | 0.03 ± 0.02 | 0.16 ± 0.02 | 0.16 ± 0.02 |
| | UK | −0.02 ± 0.01 | −0.002 ± 0.008 | 0.02 ± 0.01 | 0.02 ± 0.01 |
| | KQ | −0.04 ± 0.01 | 0.004 ± 0.011 | 0.04 ± 0.01 | 0.04 ± 0.01 |
| | CQ | −0.42 ± 0.04 | 0.06 ± 0.03 | 0.42 ± 0.04 | 0.42 ± 0.04 |
| 2007-09-13[b] | CX | −0.31 ± 0.04 | 0.06 ± 0.04 | 0.32 ± 0.04 | 0.32 ± 0.04 |
| | XU | −0.23 ± 0.02 | 0.04 ± 0.02 | 0.23 ± 0.02 | 0.23 ± 0.02 |
| | UK | −0.04 ± 0.02 | 0.02 ± 0.02 | 0.04 ± 0.02 | 0.04 ± 0.02 |
| | KQ | −0.08 ± 0.01 | 0.05 ± 0.01 | 0.09 ± 0.01 | 0.09 ± 0.01 |
| | CQ | −0.66 ± 0.05 | 0.16 ± 0.04 | 0.68 ± 0.05 | 0.68 ± 0.05 |
| 2008-01-03[b] | CX | −0.92 ± 0.03 | 0.21 ± 0.04 | 0.94 ± 0.03 | 0.92 ± 0.04 |
| | XU | −0.26 ± 0.02 | 0.18 ± 0.03 | 0.32 ± 0.02 | 0.32 ± 0.03 |
| | UK | −0.13 ± 0.01 | 0.14 ± 0.02 | 0.19 ± 0.02 | 0.18 ± 0.01 |
| | KQ | −0.15 ± 0.01 | 0.21 ± 0.02 | 0.26 ± 0.02 | 0.23 ± 0.01 |
| | CQ | −1.47 ± 0.04 | 0.74 ± 0.05 | 1.64 ± 0.04 | 1.64 ± 0.05 |
| 2008-12-07 | CXl | −0.22 ± 0.03 | −0.01 ± 0.03 | 0.22 ± 0.03 | 0.22 ± 0.03 |
| | XlXh | −0.05 ± 0.03 | 0.007 ± 0.026 | 0.05 ± 0.03 | 0.05 ± 0.03 |
| | XhU | −0.02 ± 0.03 | −0.05 ± 0.02 | 0.05 ± 0.02 | 0.02 ± 0.03 |
| | UKl | −0.11 ± 0.01 | 0.05 ± 0.02 | 0.12 ± 0.01 | 0.10 ± 0.01 |
| | KlKh | −0.02 ± 0.01 | 0.001 ± 0.010 | 0.02 ± 0.01 | 0.02 ± 0.01 |
| | KhQ | −0.05 ± 0.01 | 0.007 ± 0.008 | 0.05 ± 0.01 | 0.05 ± 0.01 |
| | CQ | −0.46 ± 0.05 | 0.002 ± 0.046 | 0.46 ± 0.05 | 0.46 ± 0.05 |
| 2009-09-22 | CX | −0.10 ± 0.03 | −0.03 ± 0.05 | 0.10 ± 0.04 | 0.09 ± 0.03 |
| | XU | −0.09 ± 0.02 | −0.02 ± 0.02 | 0.09 ± 0.02 | 0.08 ± 0.02 |

**Table A.1.** continued.

| Date | Frequency pair | R.A. (mas) | Dec (mas) | Absolute values (mas) | Projected absolute values (mas) |
|---|---|---|---|---|---|
| | UK | −0.11 ± 0.01 | 0.09 ± 0.01 | 0.14 ± 0.01 | 0.13 ± 0.02 |
| | KQ | −0.005 ± 0.011 | 0.029 ± 0.007 | 0.029 ± 0.007 | 0.01 ± 0.01 |
| | CQ | −0.30 ± 0.04 | 0.07 ± 0.05 | 0.31 ± 0.04 | 0.31 ± 0.04 |
| 2009-10-22 | CX | −0.34 ± 0.04 | 0.13 ± 0.06 | 0.37 ± 0.04 | 0.35 ± 0.04 |
| | XU | −0.13 ± 0.02 | −0.05 ± 0.02 | 0.13 ± 0.02 | 0.12 ± 0.02 |
| | UK | −0.16 ± 0.02 | 0.01 ± 0.02 | 0.16 ± 0.02 | 0.16 ± 0.02 |
| | KQ | −0.06 ± 0.02 | −0.04 ± 0.01 | 0.07 ± 0.02 | 0.06 ± 0.02 |
| | CQ | −0.69 ± 0.05 | 0.05 ± 0.06 | 0.69 ± 0.05 | 0.69 ± 0.05 |
| 2009-12-03 | CX | −0.13 ± 0.03 | −0.05 ± 0.03 | 0.14 ± 0.03 | 0.14 ± 0.03 |
| | XU | −0.13 ± 0.02 | −0.02 ± 0.02 | 0.13 ± 0.02 | 0.13 ± 0.02 |
| | UK | −0.07 ± 0.02 | 0.05 ± 0.01 | 0.08 ± 0.02 | 0.07 ± 0.02 |
| | KQ | −0.120 ± 0.007 | −0.007 ± 0.018 | 0.120 ± 0.007 | 0.120 ± 0.007 |
| | CQ | −0.45 ± 0.03 | −0.04 ± 0.04 | 0.45 ± 0.03 | 0.45 ± 0.04 |
| 2010-01-18[b] | CX | −0.25 ± 0.03 | −0.08 ± 0.03 | 0.26 ± 0.03 | 0.25 ± 0.03 |
| | XU | −0.06 ± 0.02 | −0.02 ± 0.02 | 0.06 ± 0.02 | 0.06 ± 0.02 |
| | UK | −0.11 ± 0.02 | 0.021 ± 0.009 | 0.11 ± 0.02 | 0.10 ± 0.02 |
| | KQ | −0.07 ± 0.01 | 0.032 ± 0.007 | 0.08 ± 0.01 | 0.07 ± 0.01 |
| | CQ | −0.48 ± 0.04 | −0.04 ± 0.03 | 0.49 ± 0.04 | 0.49 ± 0.04 |
| 2010-02-21[b] | CX | −0.21 ± 0.03 | −0.09 ± 0.03 | 0.23 ± 0.03 | 0.22 ± 0.03 |
| | XU | −0.09 ± 0.02 | −0.02 ± 0.01 | 0.09 ± 0.02 | 0.09 ± 0.02 |
| | UK | −0.075 ± 0.008 | 0.05 ± 0.01 | 0.09 ± 0.01 | 0.07 ± 0.01 |
| | KQ | −0.060 ± 0.007 | 0.025 ± 0.007 | 0.065 ± 0.007 | 0.058 ± 0.007 |
| | CQ | −0.44 ± 0.03 | −0.04 ± 0.03 | 0.44 ± 0.03 | 0.44 ± 0.03 |

**Notes.** the nuclear region at the Q band can be model fitted by two components where a bright moving feature has been identified at all epochs in the period 2009-2010. [a]The nuclear region at both C and X bands can be fitted with two components. [b]Only the C band can be fitted with two components.

## Appendix B: Core-shift pair vector choice

As described in Figure 3 we show in Figure B.1 a comparison of the core-shift vectors produced by the other choices. The optimal core choice at the C and X bands is the pair: Cb-Xb. This leads both CX and XU core-shift vectors to point in the jet direction (towards the west), as already demonstrated in Figure 3b.

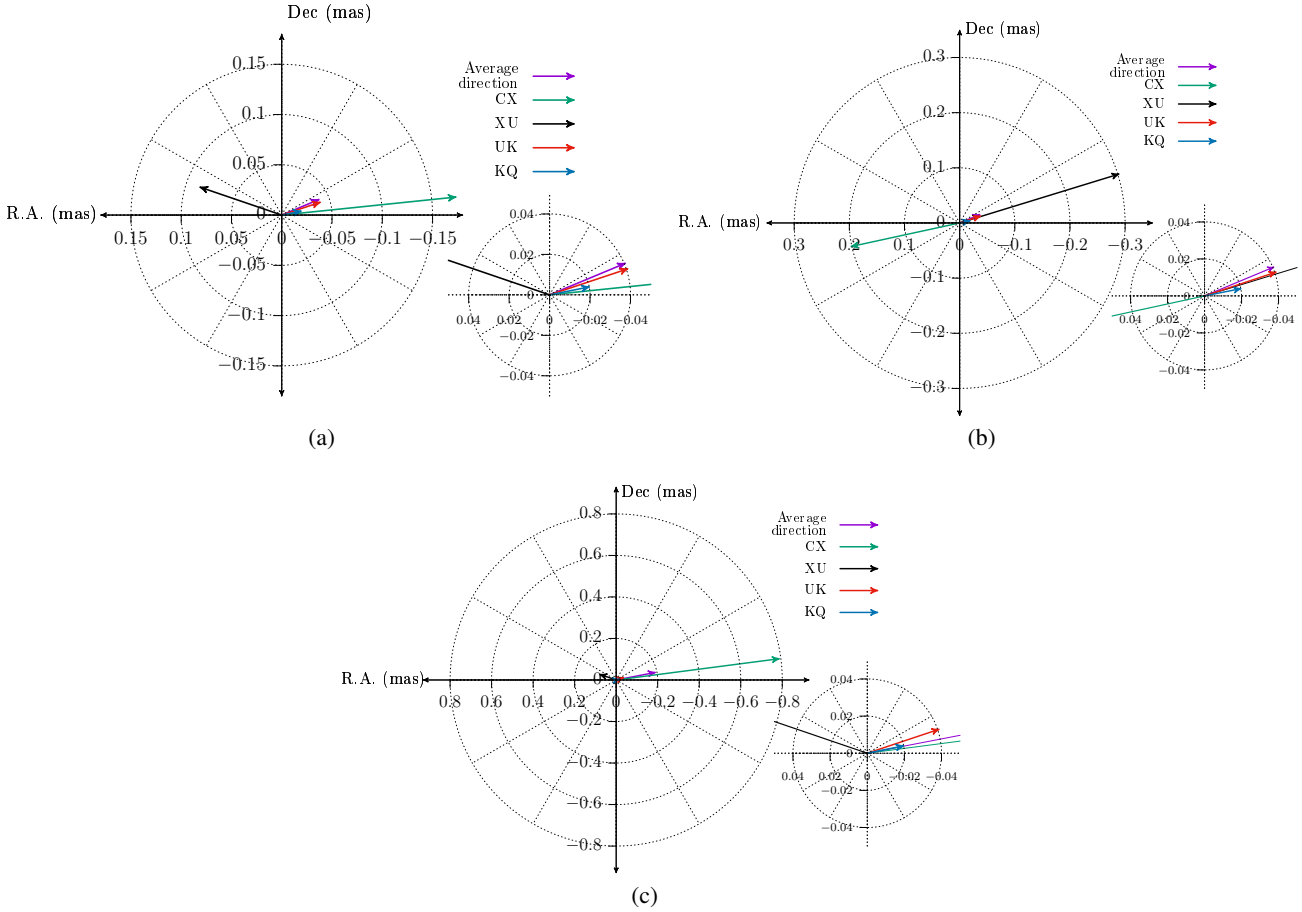


**Fig. B.1.** Core-shift vector directions by combining the alternative options for the core at the low-frequency C−X bands. These are a) Ca−Xa, b) Ca−Xb, and c) Cb−Xa. In all options, at least one vector points in the opposite direction, contrary to the jet direction that is towards the west.

## Appendix C: Parameter uncertainties

### C.1. Uncertainty of $\Omega_{r\nu}$

The uncertainty of $\Omega_{r\nu}$, denoted by $\Delta\Omega_{r\nu}$ is obtained by propagating uncertainty in Equation 5 with both $\Delta r_{\nu_1\nu_2}$ and $k_r$ as variable parameters. For simplification purposes, we set here $\Delta r_{\nu_1\nu_2} = l$ and the uncertainty of $\Delta r_{\nu_1\nu_2} = \Delta l$. The uncertainty of index $k_r$ is $\Delta k_r$. The expression for $\Delta\Omega_{r\nu}$ is given as

$$\Delta\Omega_{r\nu} = \sqrt{\left(\frac{\partial\Omega}{\partial l}\cdot\Delta l\right)^2 + \left(\frac{\partial\Omega}{\partial k_r}\cdot\Delta k_r\right)^2}, \tag{C.1}$$

where

$$\frac{\partial\Omega_{r\nu}}{\partial l} = \frac{\Omega_{r\nu}}{l}, \tag{C.2}$$

and

$$\frac{\partial\Omega_{r\nu}}{\partial k_r} = \Omega_{r\nu}\frac{\left(\nu_1^{1/k_r}\ln(\nu_2) - \nu_2^{1/k_r}\ln(\nu_1)\right)}{k_r^2(\nu_2^{1/k_r} - \nu_1^{1/k_r})}. \tag{C.3}$$

Plugging C.2 and C.3 into C.1, the uncertainty of $\Omega_{r\nu}$ is given by

$$\Delta\Omega_{r\nu} = \Omega_{r\nu}\sqrt{\left(\frac{\Delta l}{l}\right)^2 + \left(\frac{\nu_1^{1/k_r}\ln(\nu_2) - \nu_2^{1/k_r}\ln(\nu_1)}{k_r^2(\nu_2^{1/k_r} - \nu_1^{1/k_r})}\cdot\Delta k_r\right)^2}. \tag{C.4}$$

Equation C.4 is a generic formula to estimate the uncertainties in $\Omega_{r\nu}$ for each frequency pair: $\Delta\Omega_{CX}$, $\Delta\Omega_{XU}$, $\Delta\Omega_{UK}$ and $\Delta\Omega_{KQ}$.

### C.2. Uncertainty of $r_{\rm core}$

The uncertainty of $r_{\rm core}$ is denoted by $\Delta r_{\rm core}$. The measured uncertainties are propagated in Equation 4 having $\Omega_{r\nu}$ and $k_r$ as variable parameters. We note that $\Omega_{r\nu}$ is an average-mean value per epoch; therefore, the expression for $\Delta r_{\rm core}$ is

$$\Delta r_{\rm core} = \sqrt{\left(\frac{\partial r_{\rm core}}{\partial\Omega_{r\nu}}\cdot\Delta\Omega_{r\nu}\right)^2 + \left(\frac{\partial r_{\rm core}}{\partial k_r}\cdot\Delta k_r\right)^2}, \tag{C.5}$$

with

$$\frac{\partial r_{\rm core}}{\partial\Omega_{r\nu}} = \frac{r_{\rm core}}{\Omega_{r\nu}}, \tag{C.6}$$

and

$$\frac{\partial r_{\rm core}}{\partial k_r} = r_{\rm core}\frac{\ln(\nu)}{k_r^2}. \tag{C.7}$$

Plugging C.6 and C.7 into C.5, the uncertainty of $r_{\rm core}$ is given by

$$\Delta r_{\rm core} = r_{\rm core}\sqrt{\left(\frac{\Delta\Omega_{r\nu}}{\Omega_{r\nu}}\right)^2 + \left(\frac{\ln(\nu)}{k_r^2}\Delta k_r\right)^2}. \tag{C.8}$$

### C.3. Uncertainty of $B_{\rm 1pc}$

The uncertainty of $B_{\rm 1pc}$ is denoted by $\Delta B_{\rm 1pc}$. The measured uncertainties are propagated in Equation 6 with respect to the CQ core shift, $\Delta r_{CQ}$, $\delta$, $\theta_{\rm j}$, $\theta$, and $k_r$. Below $M = 4.85\cdot10^{-9}\,D_L/(1+z)^2$. Inserting equation 5 into equation 6, the formula for $B_{\rm 1pc}$ transforms to

$$B_{\rm 1pc} \approx 0.025\left[\frac{\sigma_{\rm rel}\,(1+z)^3}{\delta^2\,\theta_{\rm j}\sin^{3k_r-1}\theta}\,\nu_1^3\nu_2^3\left(\frac{M\Delta r_{CQ}}{\nu_2^{1/k_r} - \nu_1^{1/k_r}}\right)^{3k_r}\right]^{\frac{1}{4}}\,[\rm G]. \tag{C.9}$$

For simplification purposes, we set here $\Delta r_{CQ} = A$ and the uncertainty of the CQ core shift as $\Delta A$. The error of $B_{\rm 1pc}$ is denoted by $\Delta B_{\rm 1pc}$ and is obtained as

$$\begin{aligned}\Delta B_{\rm 1pc} =& \left[\left(\frac{\partial B_{\rm 1pc}}{\partial A}\cdot\Delta A\right)^2 + \left(\frac{\partial B_{\rm 1pc}}{\partial\delta}\cdot\Delta\delta\right)^2 + \left(\frac{\partial B_{\rm 1pc}}{\partial\theta_{\rm j}}\cdot\Delta\theta_{\rm j}\right)^2\right.\\ &\left. + \left(\frac{\partial B_{\rm 1pc}}{\partial\theta}\cdot\Delta\theta\right)^2 + \left(\frac{\partial B_{\rm 1pc}}{\partial k_r}\cdot\Delta k_r\right)^2\right]^{1/2},\end{aligned} \tag{C.10}$$

where

$$\frac{\partial B_{\rm 1pc}}{\partial A} = \frac{3}{4}k_r\frac{B_{\rm 1pc}}{\Delta A}, \tag{C.11}$$

$$\frac{\partial B_{\rm 1pc}}{\partial\delta} = -\frac{1}{2}\frac{B_{\rm 1pc}}{\delta}, \tag{C.12}$$

$$\frac{\partial B_{\rm 1pc}}{\partial\theta_{\rm j}} = -\frac{1}{4}\frac{B_{\rm 1pc}}{\theta_{\rm j}}, \tag{C.13}$$

$$\frac{\partial B_{\rm 1pc}}{\partial\theta} = -\frac{1}{4}(3k_r - 1)\frac{\cos\theta}{\sin\theta}B_{\rm 1pc}, \tag{C.14}$$

$$\begin{aligned}\frac{\partial B_{\rm 1pc}}{\partial k_r} =& \frac{3}{4}\frac{1}{k_r}B_{\rm 1pc}\frac{1}{\nu_2^{1/k_r} - \nu_1^{1/k_r}}\\ &\left[k_r(\nu_2^{1/k_r} - \nu_1^{1/k_r})\left(\ln\left(\frac{MA}{\nu_2^{1/kr} - \nu_1^{1/k_r}}\right) - \ln(\sin\theta)\right)\right.\\ &\left. + \nu_2^{1/k_r}\ln(\nu_2) - \nu_1^{1/k_r}\ln(\nu_1)\right]\end{aligned} \tag{C.15}$$

Finally, plugging all the partial derivatives into C.10, the error of $B_{\rm 1pc}$ is readily obtained.

## Appendix D: Core spectrum, core-shift vectors, and power-law fits

The main results of the core-shift analysis for individual epochs (listed in Table 1) are shown in Figures D.1–D.18. The results for each epoch include the core spectrum, the core-shift vectors in polar coordinates, and the core-shift power-law fit. Projected values of the core shifts onto the average direction are used. All fitting parameters are summarized in Table 2.

We note that we still present the core-shift analysis for the observation on 2008 January 03 (epoch 13, Figure D.12) as a demonstration of the case when large core shifts are measured due to lack of resolution. Furthermore, as emphasized in the main text, this observation was not included in the variability analysis.

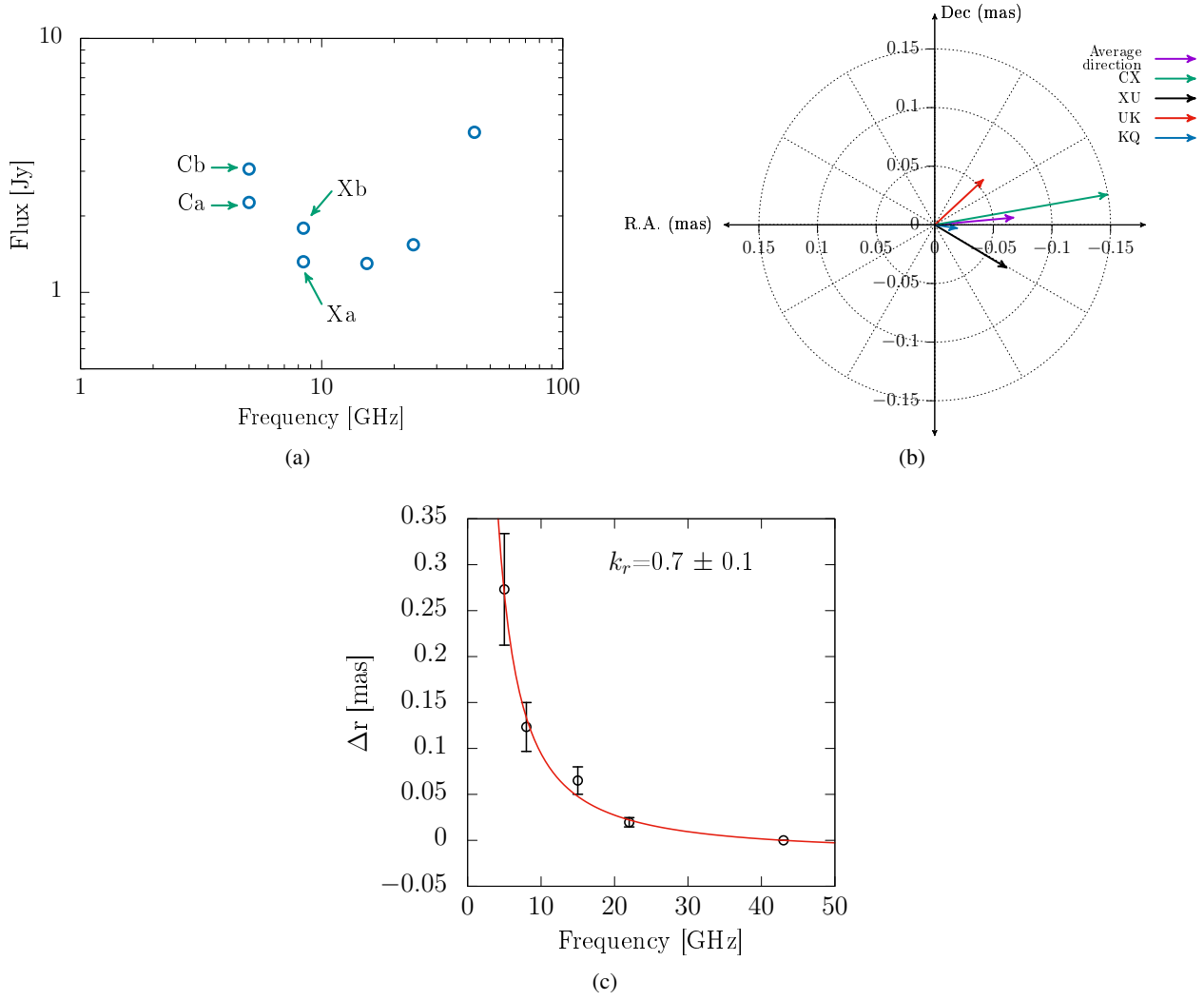


**Fig. D.1.** Epoch 1, 2005 May 19. (a) Core spectrum, Ca−Xa represent the core. (b) Core-shift vectors of all frequency pairs. The choice of Ca−Xa cores leads to the correct direction of vectors CX and XU. (c) The power-law fit is shown with the red curve.

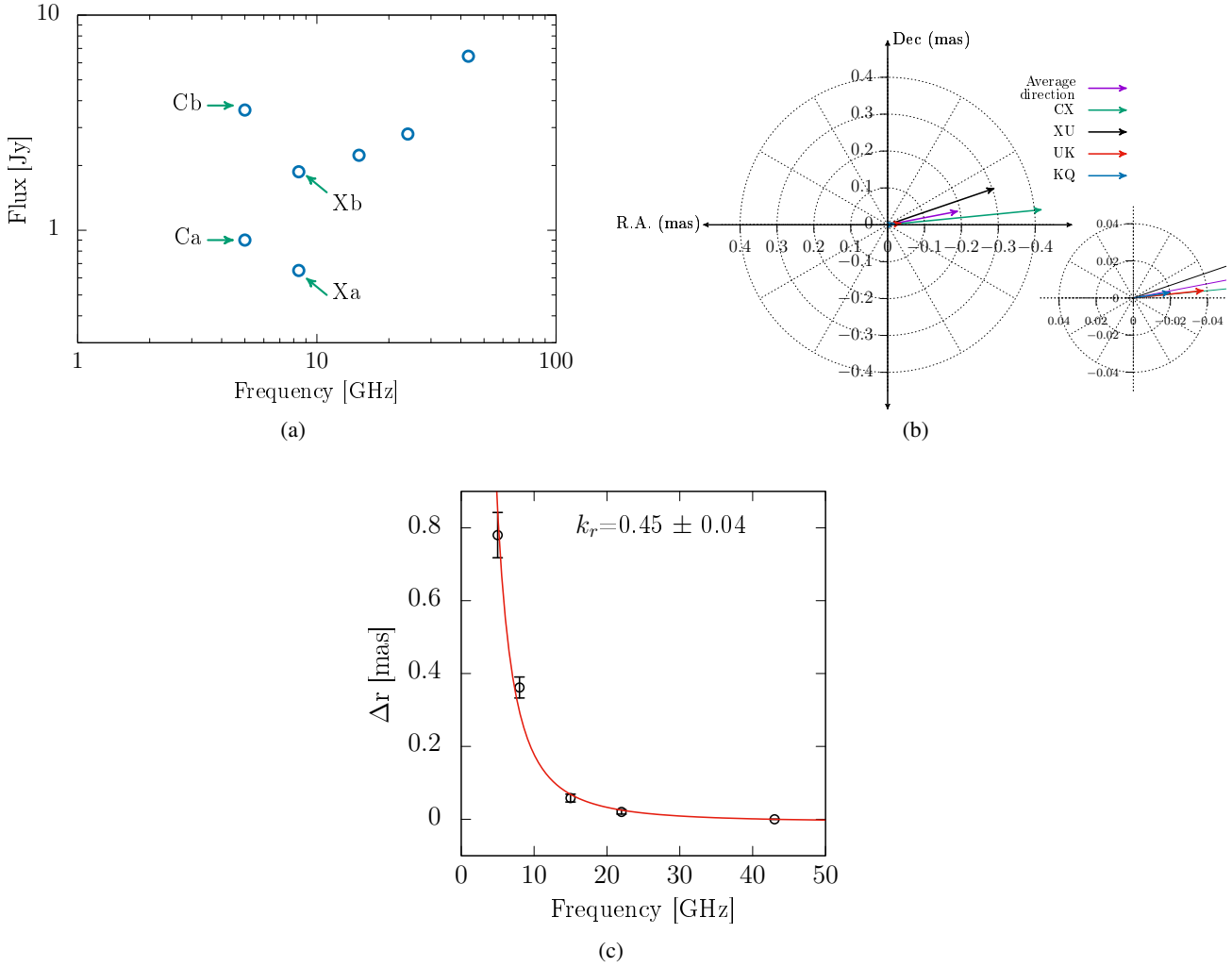


**Fig. D.2.** Epoch 2, 2005 July 14: (a) Core spectrum, Cb−Xb represent the core. (b) Core-shift vectors of all frequency pairs. The choice of Cb−Xb cores leads to the correct direction of vectors CX and XU. (c) The power-law fit is shown with the red curve.

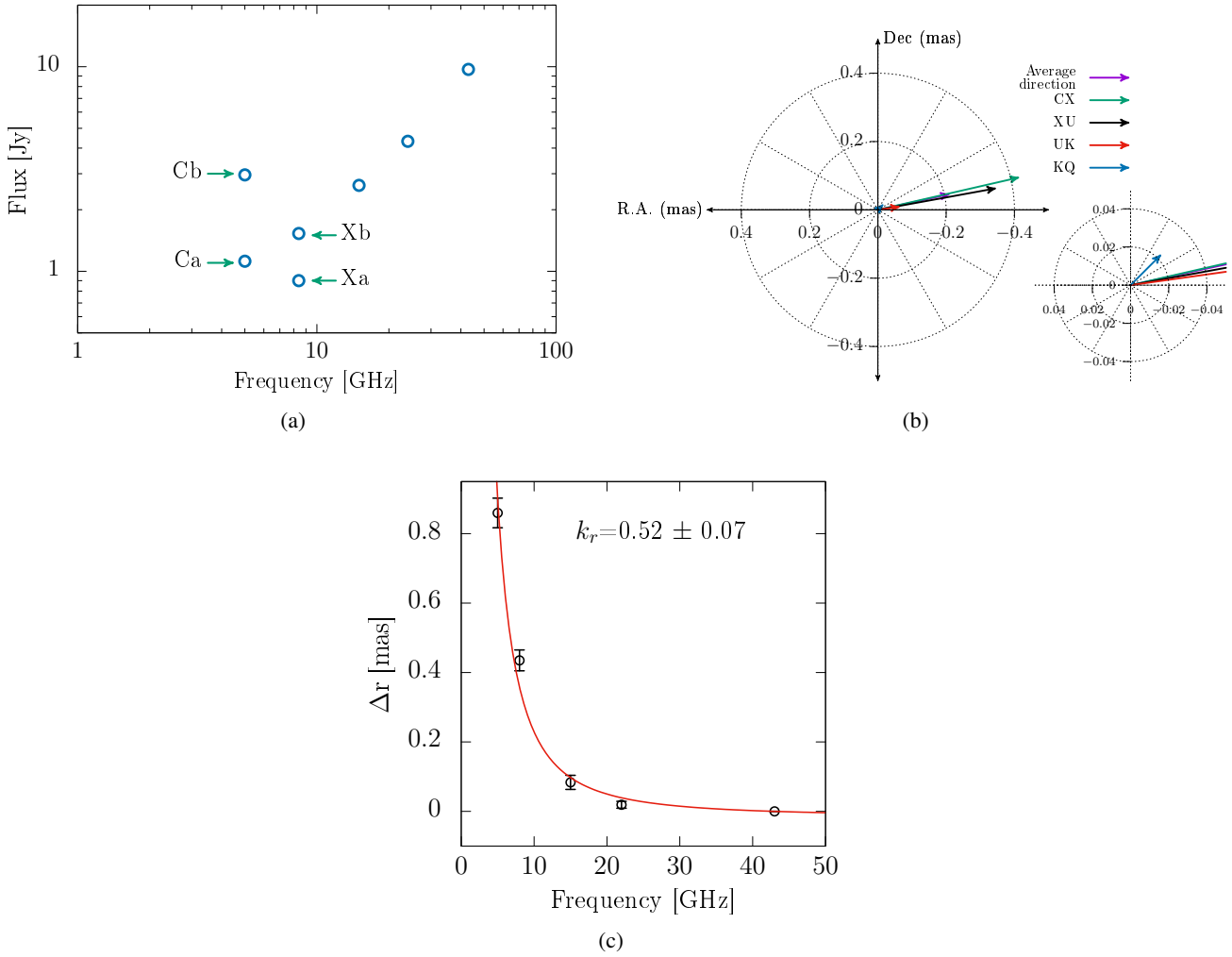


**Fig. D.3.** Epoch 3, 2005 September 01: (a) Core spectrum, Cb−Xb represent the core. (b) Core-shift vectors of all frequency pairs. The choice of Cb−Xb cores leads to the correct direction of vectors CX and XU. (c) The power-law fit is shown with the red curve.

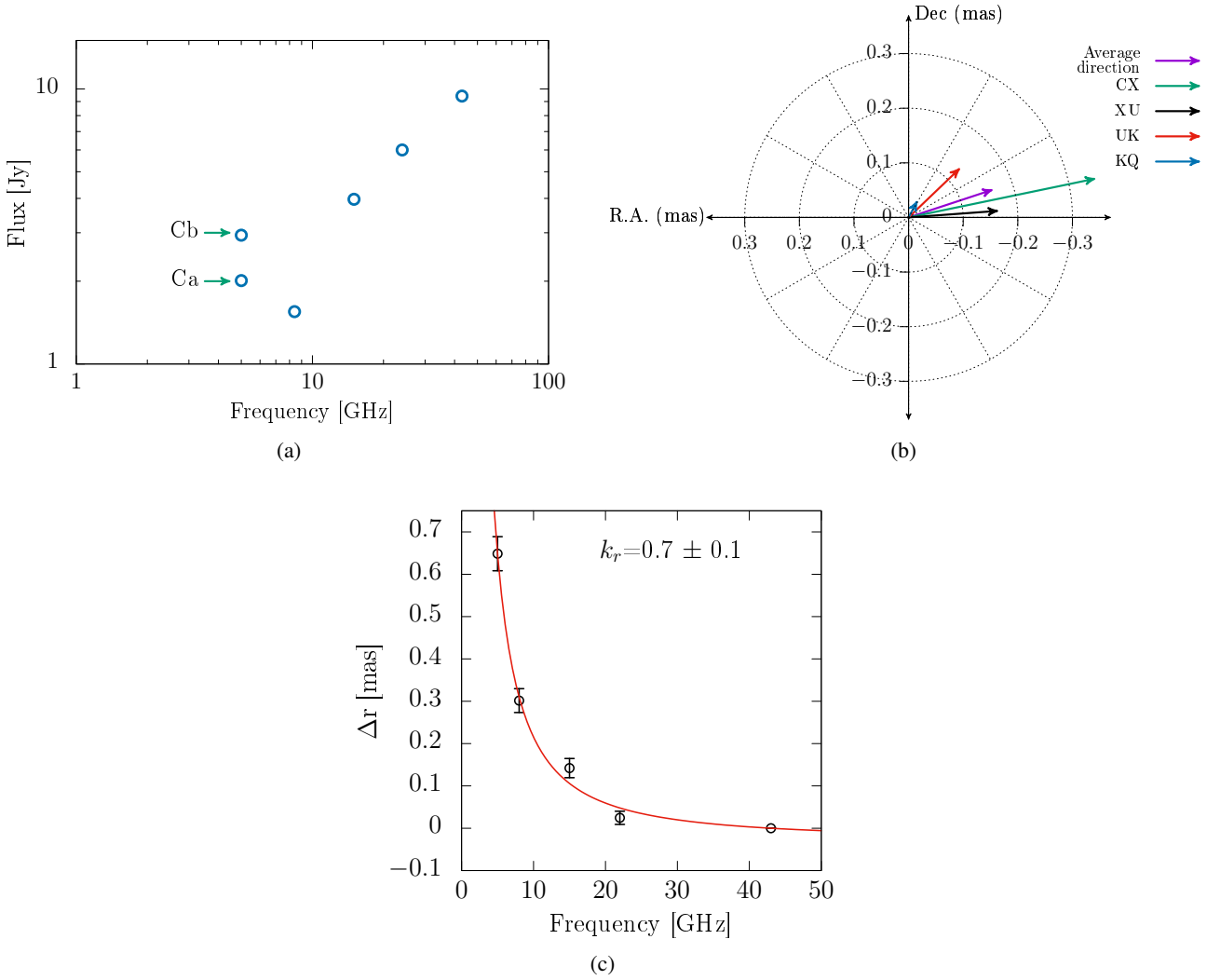


**Fig. D.4.** Epoch 4, 2005 December 04. (a) Core spectrum, Ca represents the core. (b) Core-shift vectors of all frequency pairs. The choice of Ca core leads to the correct direction of the CX vector. (c) The power-law fit is shown with the red curve.

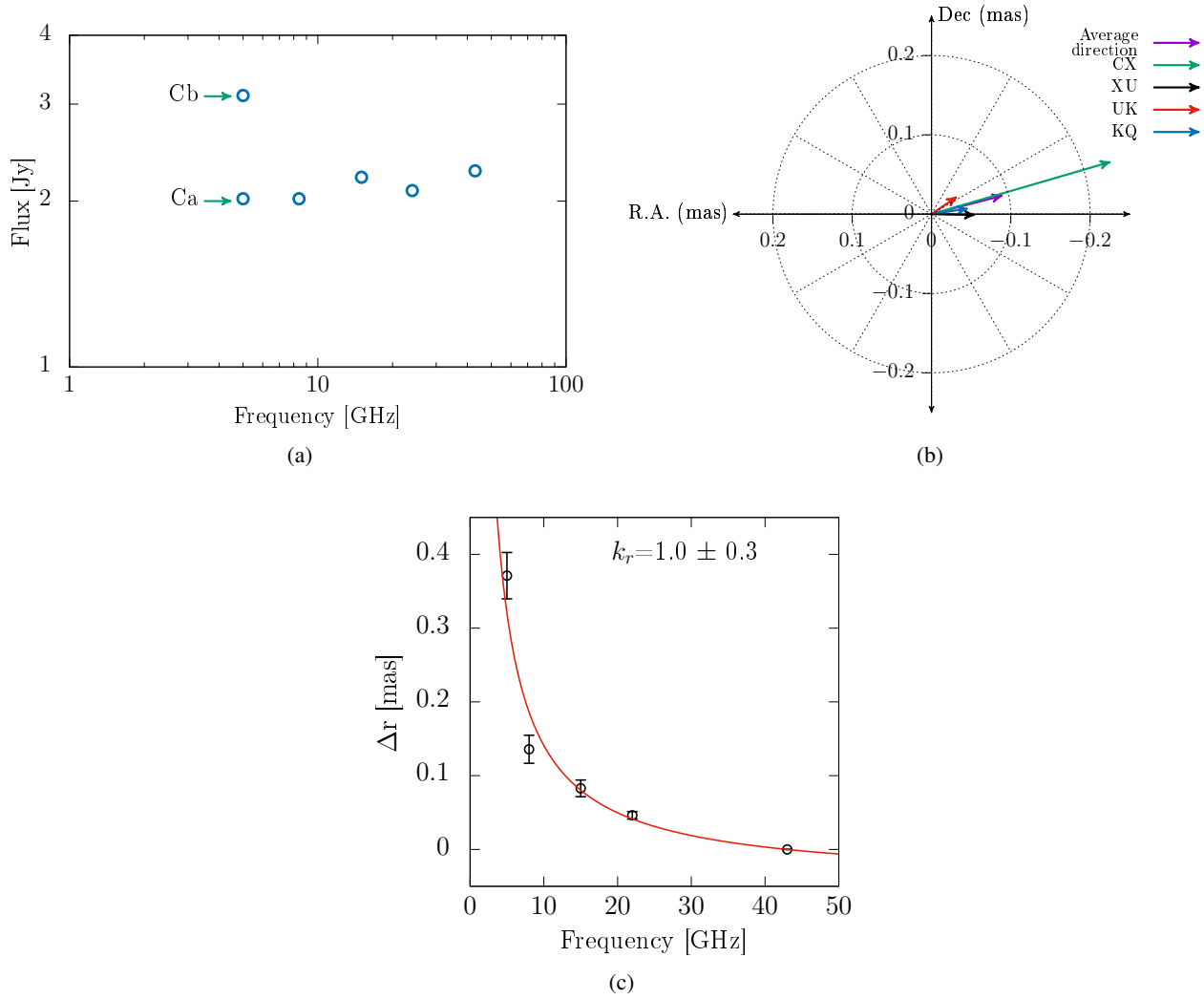


**Fig. D.5.** Epoch 6, 2006 October 02. (a) Core spectrum, Ca represents the core. (b) Core-shift vectors of all frequency pairs. The choice of Ca core leads to the correct direction of the CX vector. (c) The power-law fit is shown with the red curve.

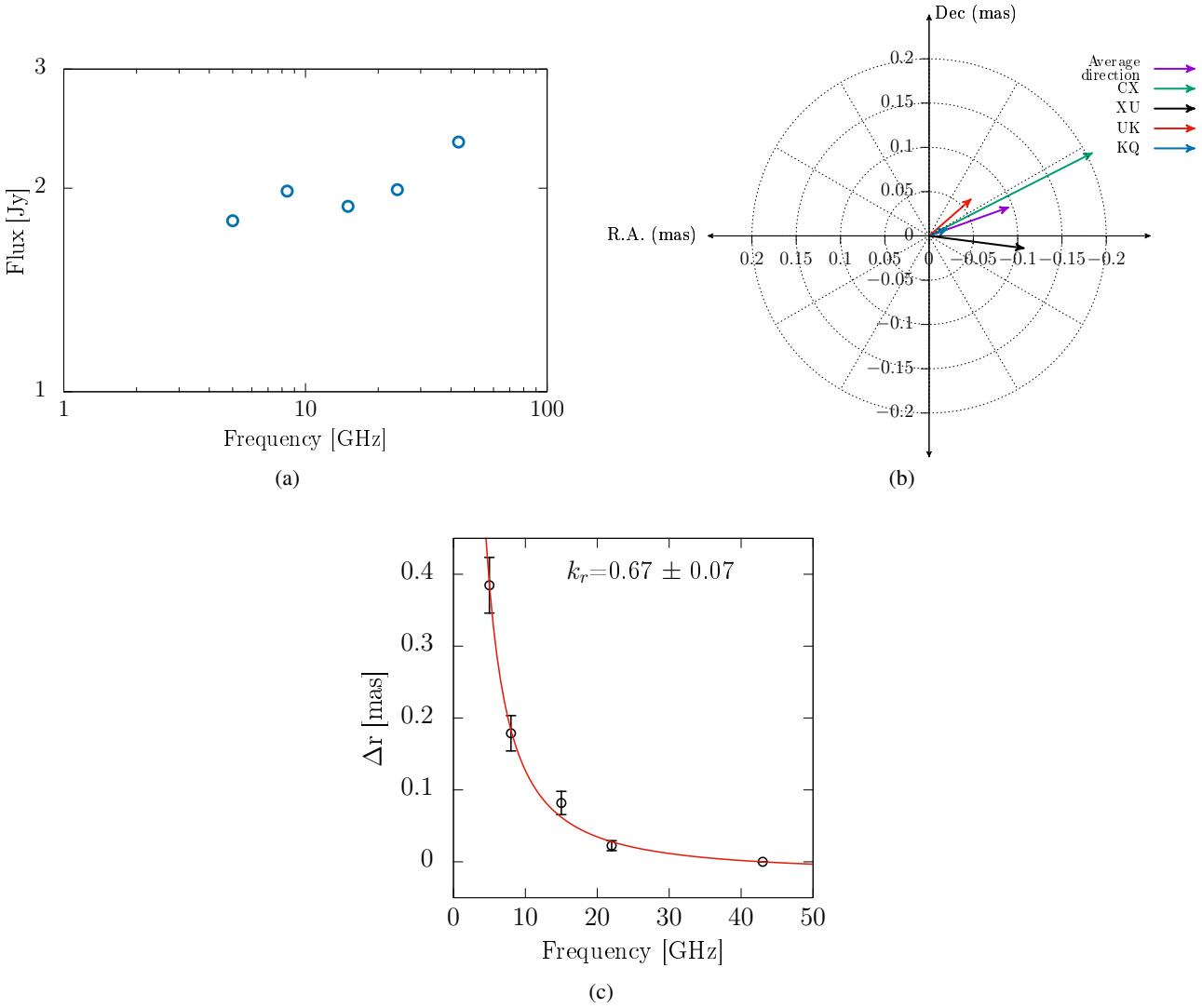


**Fig. D.6.** Epoch 7, 2006 December 04. (a) Core spectrum. (b) Core-shift vectors of all frequency pairs. (c) The power-law fit is shown with the red curve.

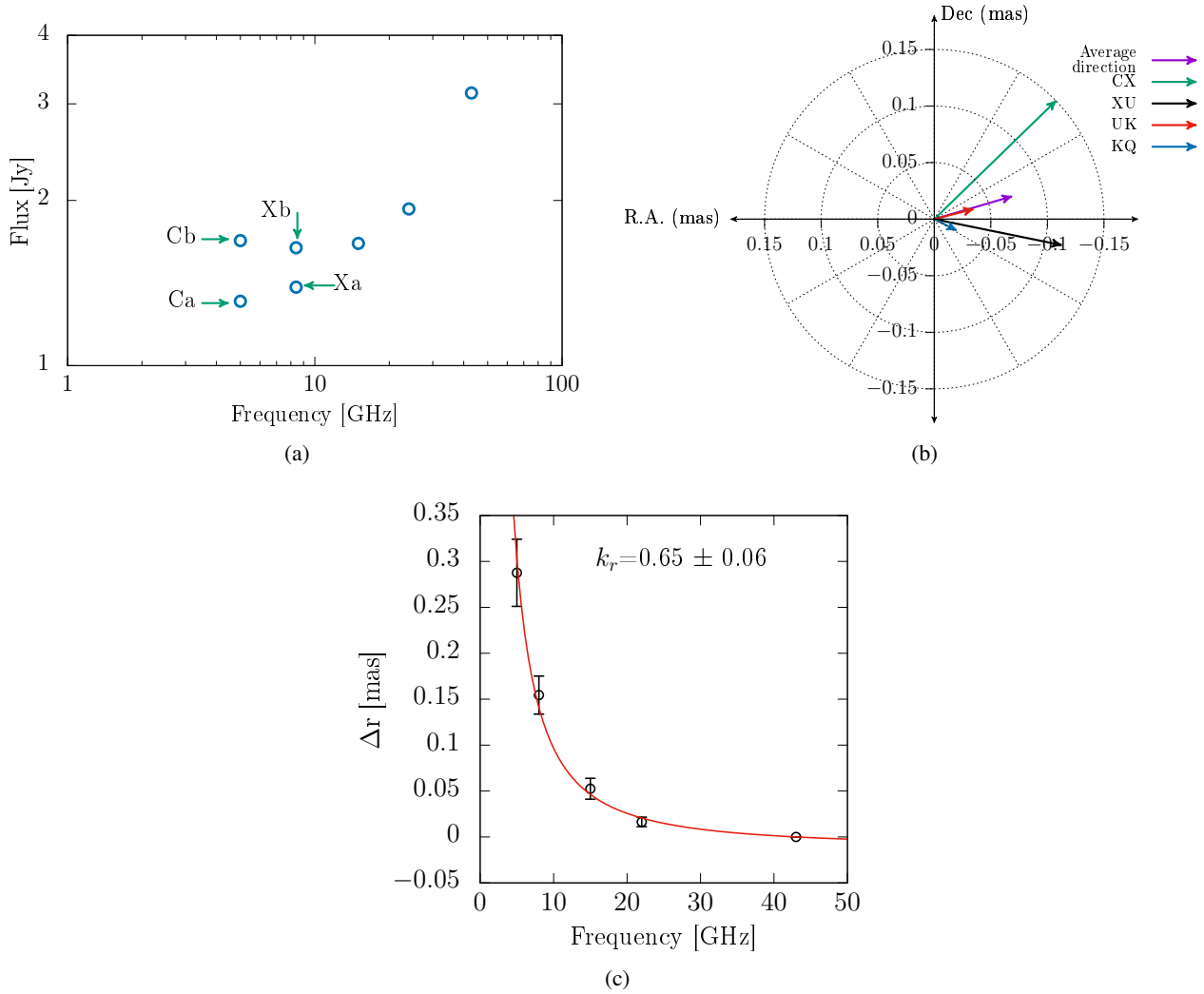


**Fig. D.7.** Epoch 8, 2007 January 26. (a) Core spectrum, Ca−Xb represent the core. (b) Core-shift vectors of all frequency pairs. The choice of Ca−Xb cores leads to the correct direction of vectors CX and XU. (c) The power-law fit is shown with the red curve.

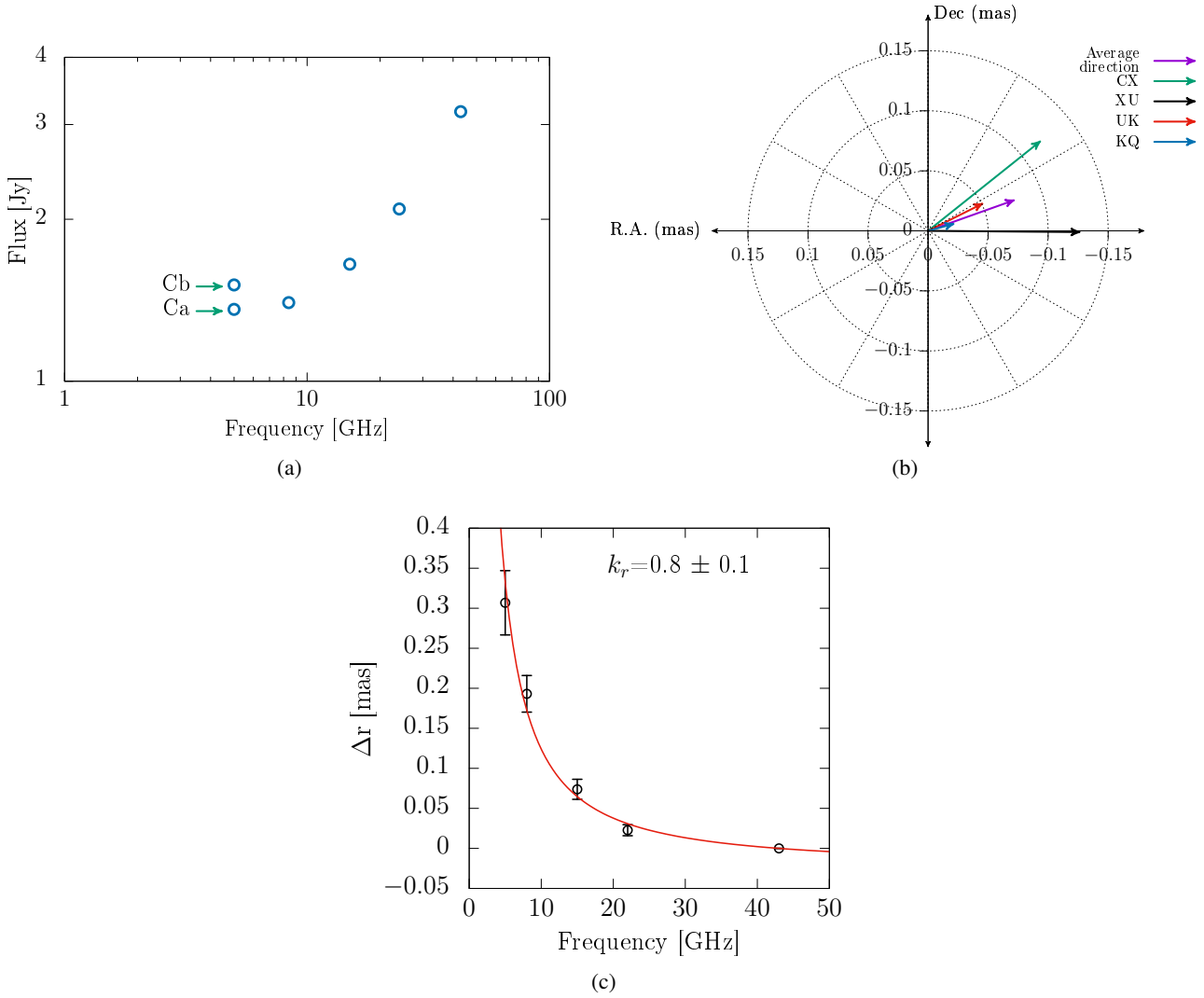


**Fig. D.8.** Epoch 9, 2007 April 26. (a) Core spectrum, Ca represents the core. (b) Core-shift vectors of all frequency pairs. The choice of Ca core leads to the correct direction of the CX vector. (c) The power-law fit is shown with the red curve.

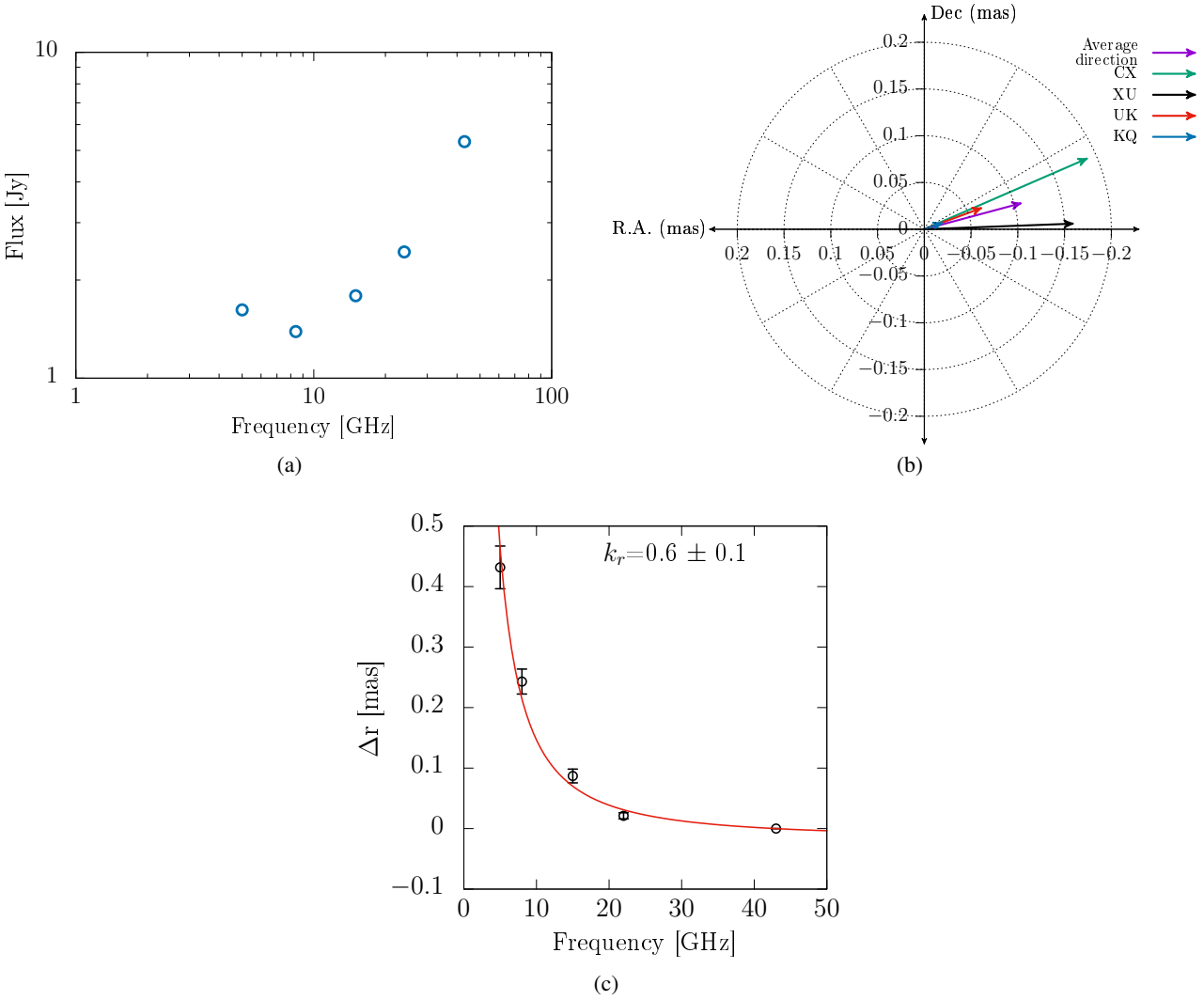


**Fig. D.9.** Epoch 10, 2007 June 16. (a) Core spectrum. (b) Core-shift vectors of all frequency pairs. (c) The power-law fit is shown with the red curve.

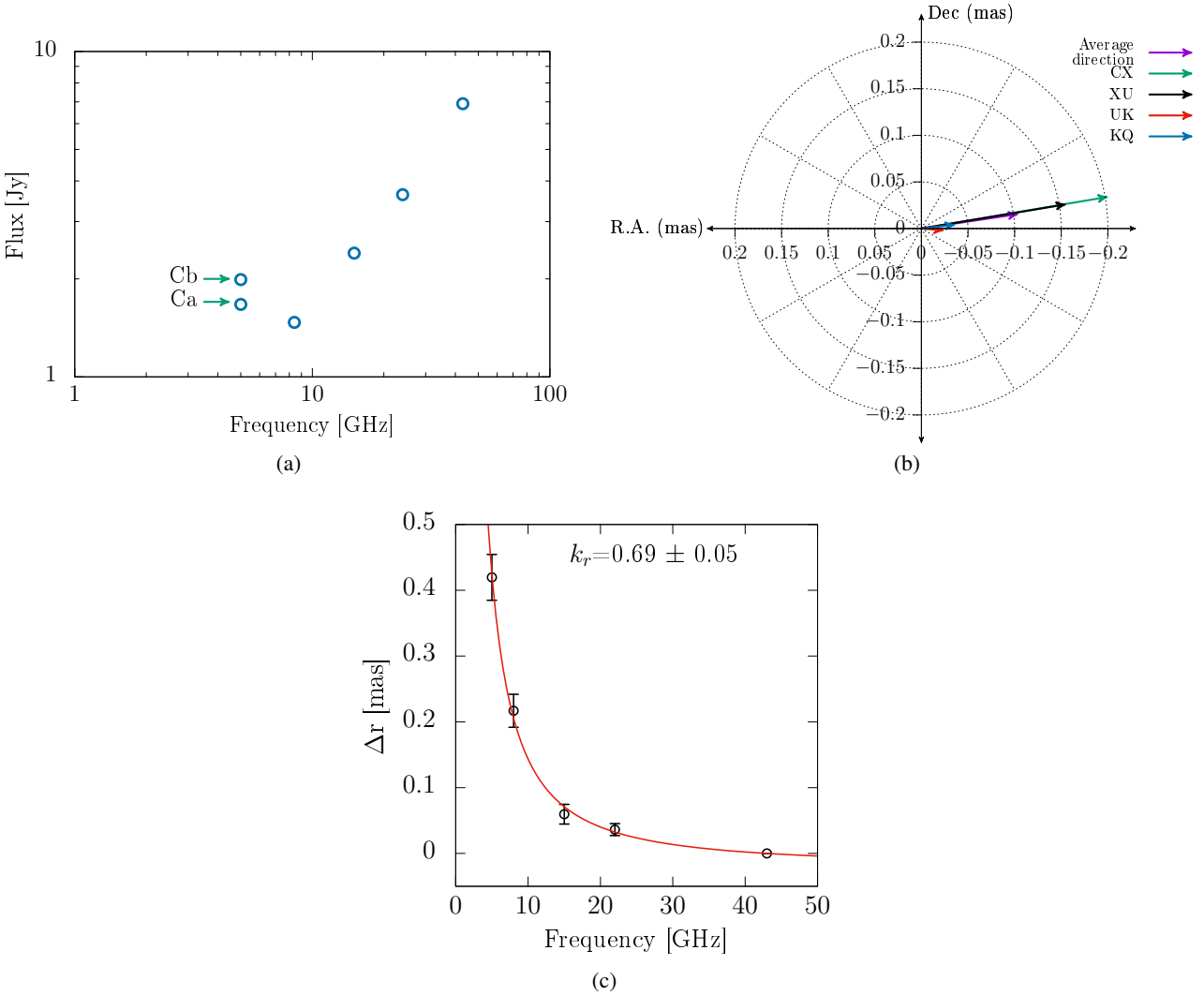


**Fig. D.10.** Epoch 11, 2007 July 25. (a) Core spectrum, Ca represents the core. (b) Core-shift vectors of all frequency pairs. The choice of Ca core leads to the correct direction of the CX vector. (c) The power-law fit is shown with the red curve.

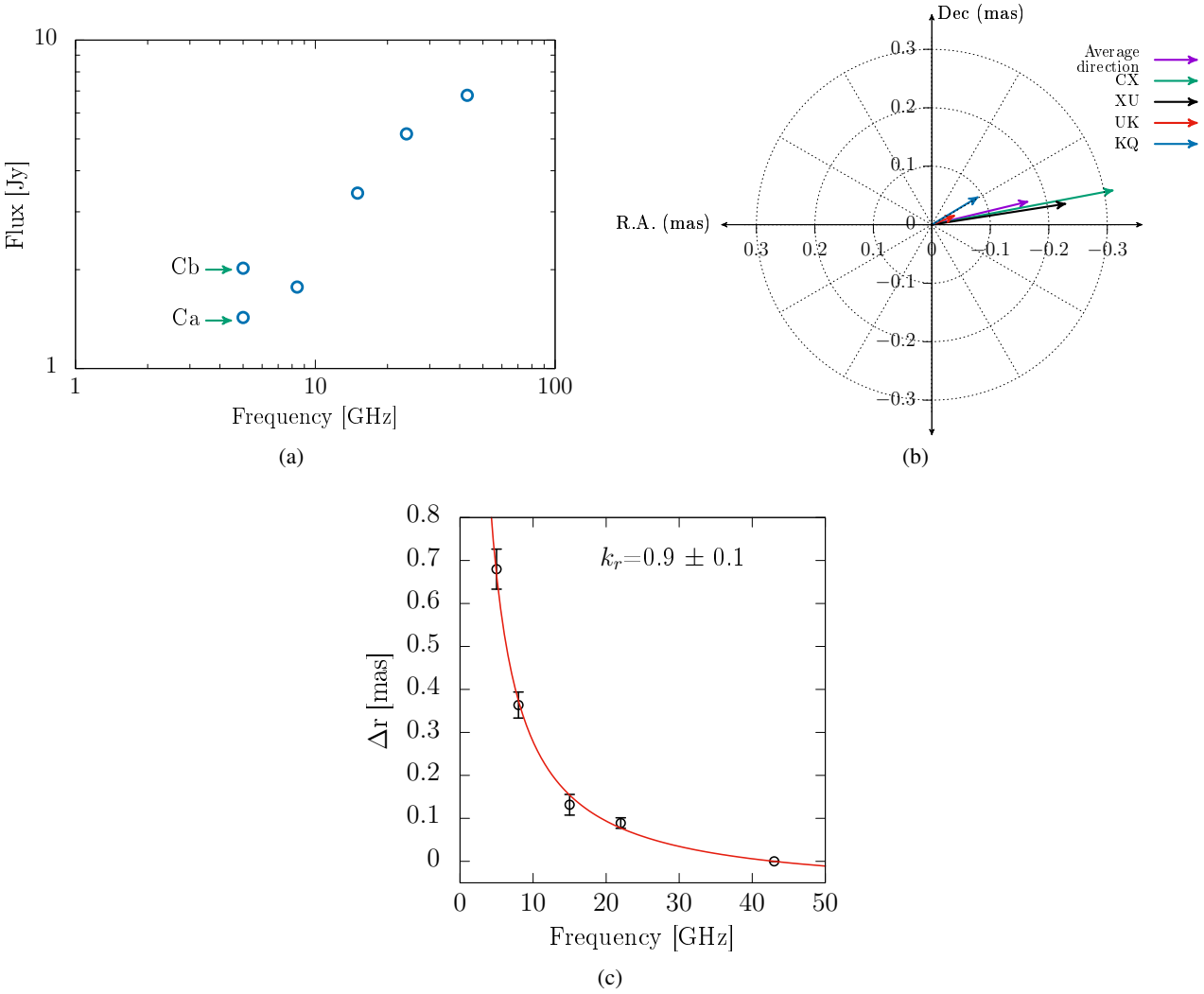


**Fig. D.11.** Epoch 12, 2007 September 13. (a) Core spectrum, Cb represents the core. (b) Core-shift vectors of all frequency pairs. The choice of Cb core leads to the correct direction of the CX vector. (c) The power-law fit is shown with the red curve.

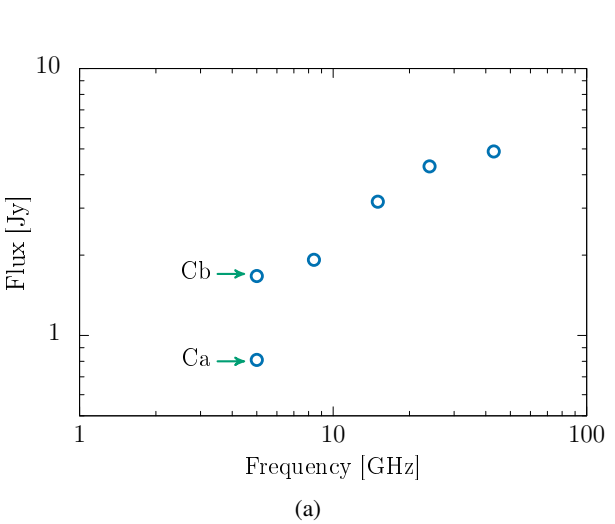


(a)

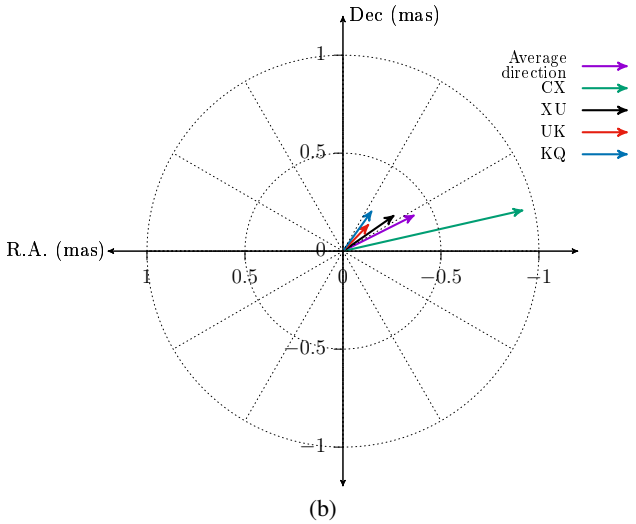


(b)

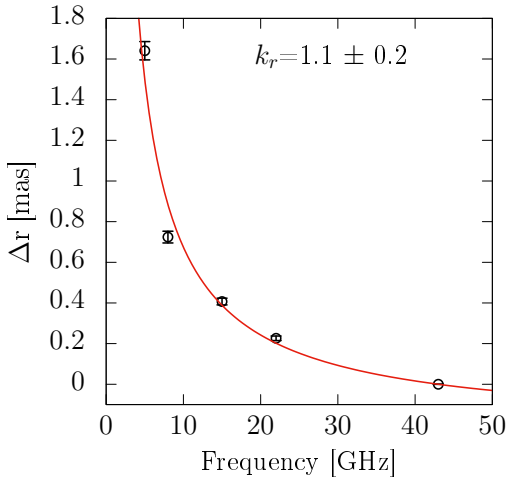


(c)

**Fig. D.12.** Epoch 13, 2008 January 03. (a) Core spectrum, Cb possibly represents the core. (b) Core-shift vectors of all frequency pairs. (c) Power-law fit is shown with the red curve. Due to the poor $(u, v)$ coverage, the core at the C band cannot be well resolved, producing ambiguities on its location. As a result, very large core-shift values above 1 mas were measured. This observation was not included in the variability analysis.

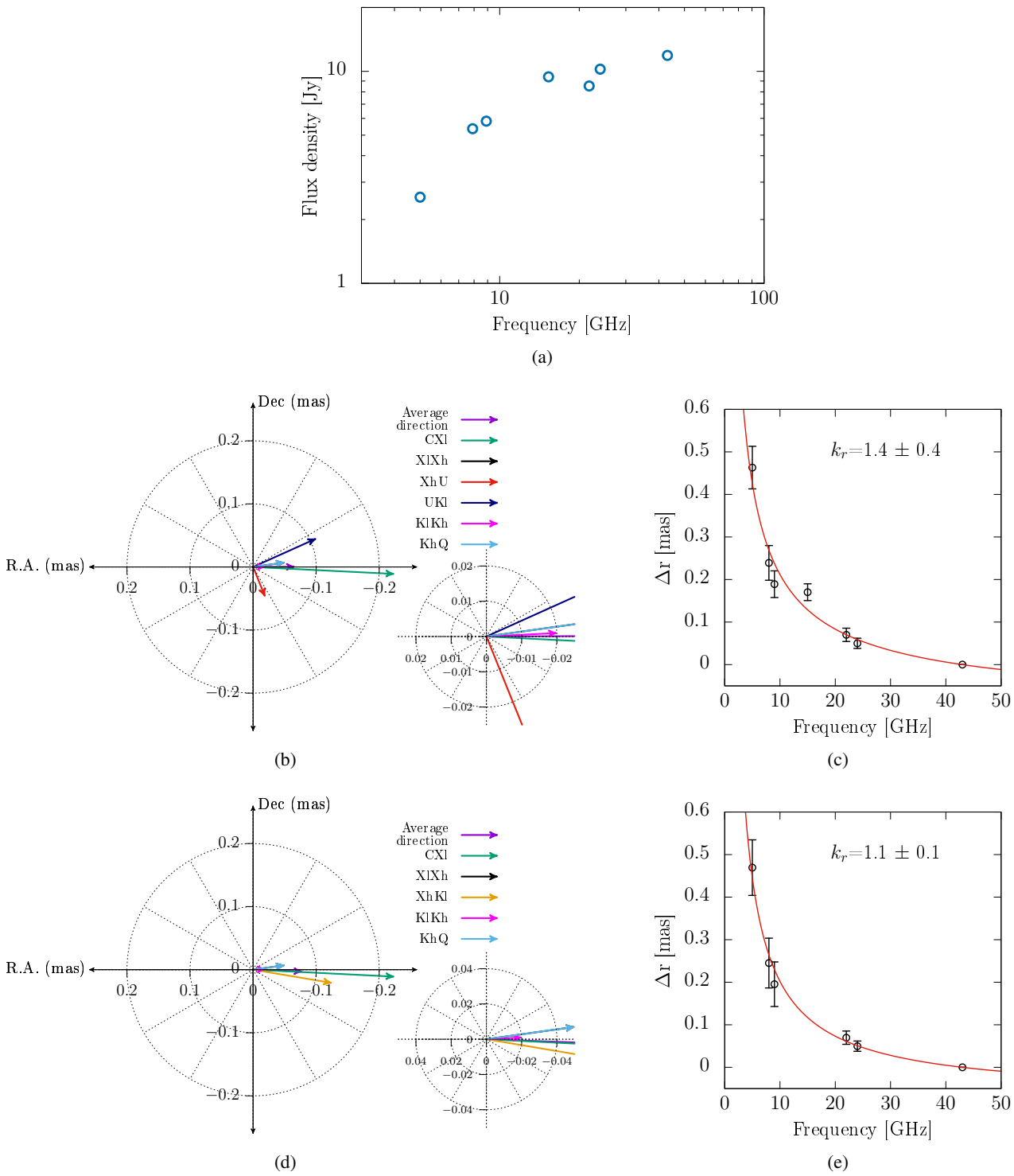


**Fig. D.13.** Epoch 14, 2008 December 07. (a) Core spectrum. (b) Core-shift vectors of all frequency pairs, including intermediate frequencies denoted by Xl (7.9 GHz), Xh (8.9 GHz), Kl (21.8 GHz) and Kh (24 GHz). (c) Power-law fit (red curve) using all bands. (d) Core-shift vectors without the U band, (e) Power-law fit (red curve) using all bands except the U band. This approach leads to a better fit.

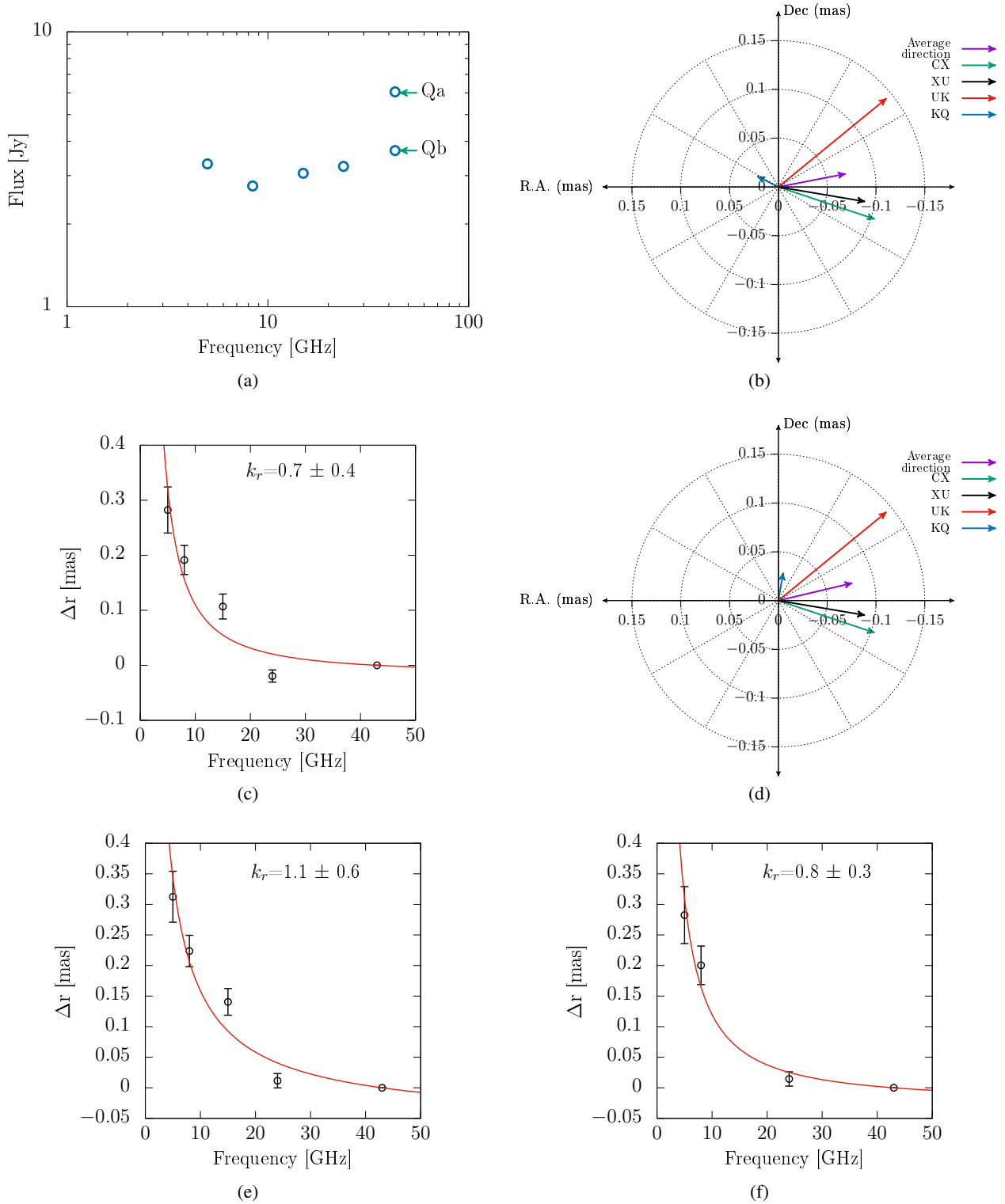


**Fig. D.14.** Epoch 15, 2009 September 22. a) Core spectrum, where Qa represents the core and Qb the feature moving downstream. For comparisons, see Figure 4a. b) Core-shift vectors of all frequency pairs. Using component Qb makes the KQ core-shift vector point in the opposite direction. c) Power-law fit (red curve) using the Qb component. d) Core-shift vectors of all frequency pairs. Using component Qa, labelled as the core, gives a reasonable direction of the KQ core-shift vector. e) Power-law fit (red curve) using Qa as the core, but a better fit is obtained f) when the U band is excluded.

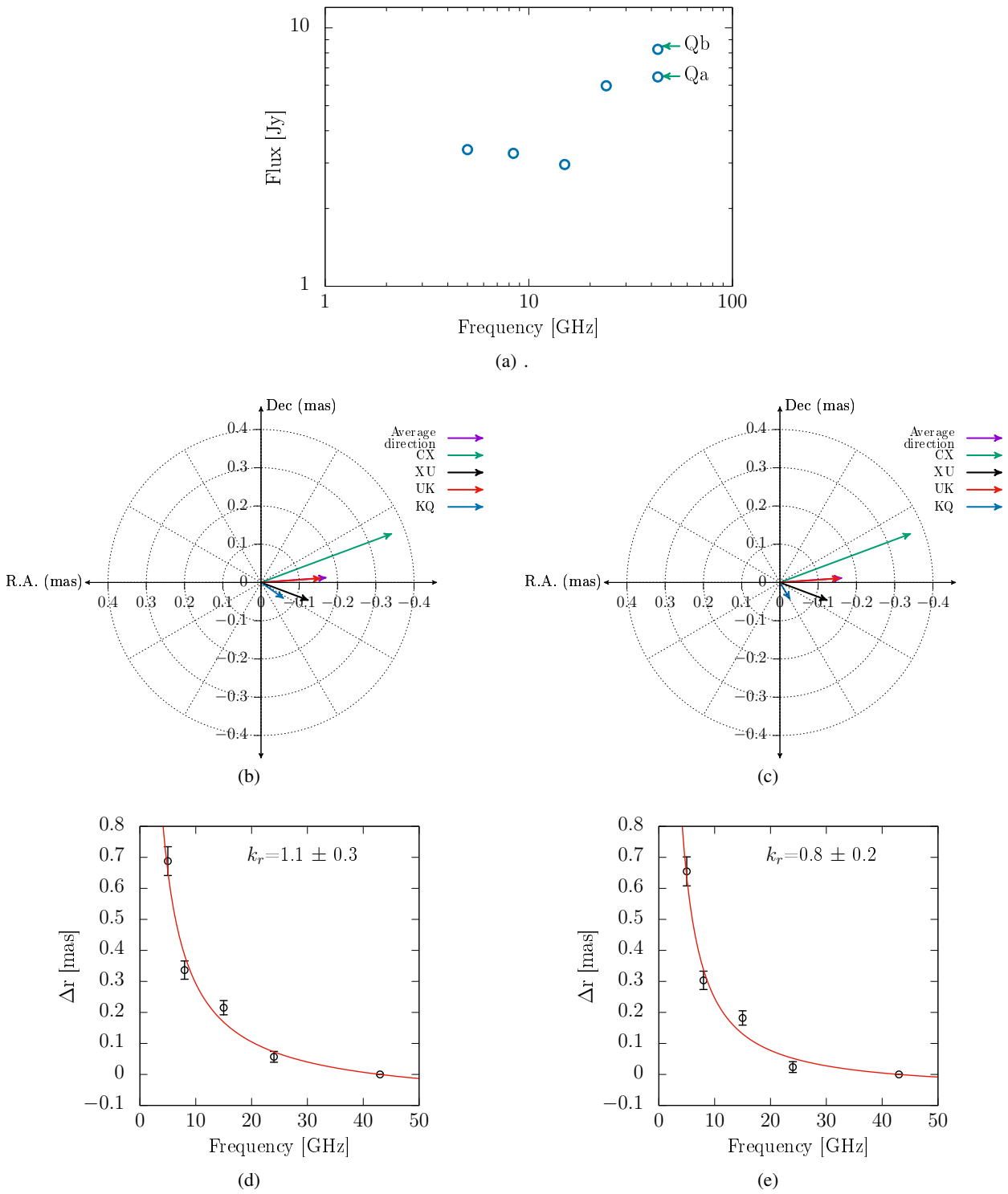


**Fig. D.15.** Epoch 16, 2009 October 22. a) Core spectrum, where Qa represents the core and Qb the feature moving downstream. For comparisons, see Figure 4b. Core-shift vectors of all frequency pairs using b) Qa and c) Qb. In this case, the two components have a similar impact on the direction of KQ core-shift vector. Power-law fits (red curve) using d) Qa and e) Qb. In this epoch, the flare appears to hinder the correct location of the core at the Q-band (43 GHz).

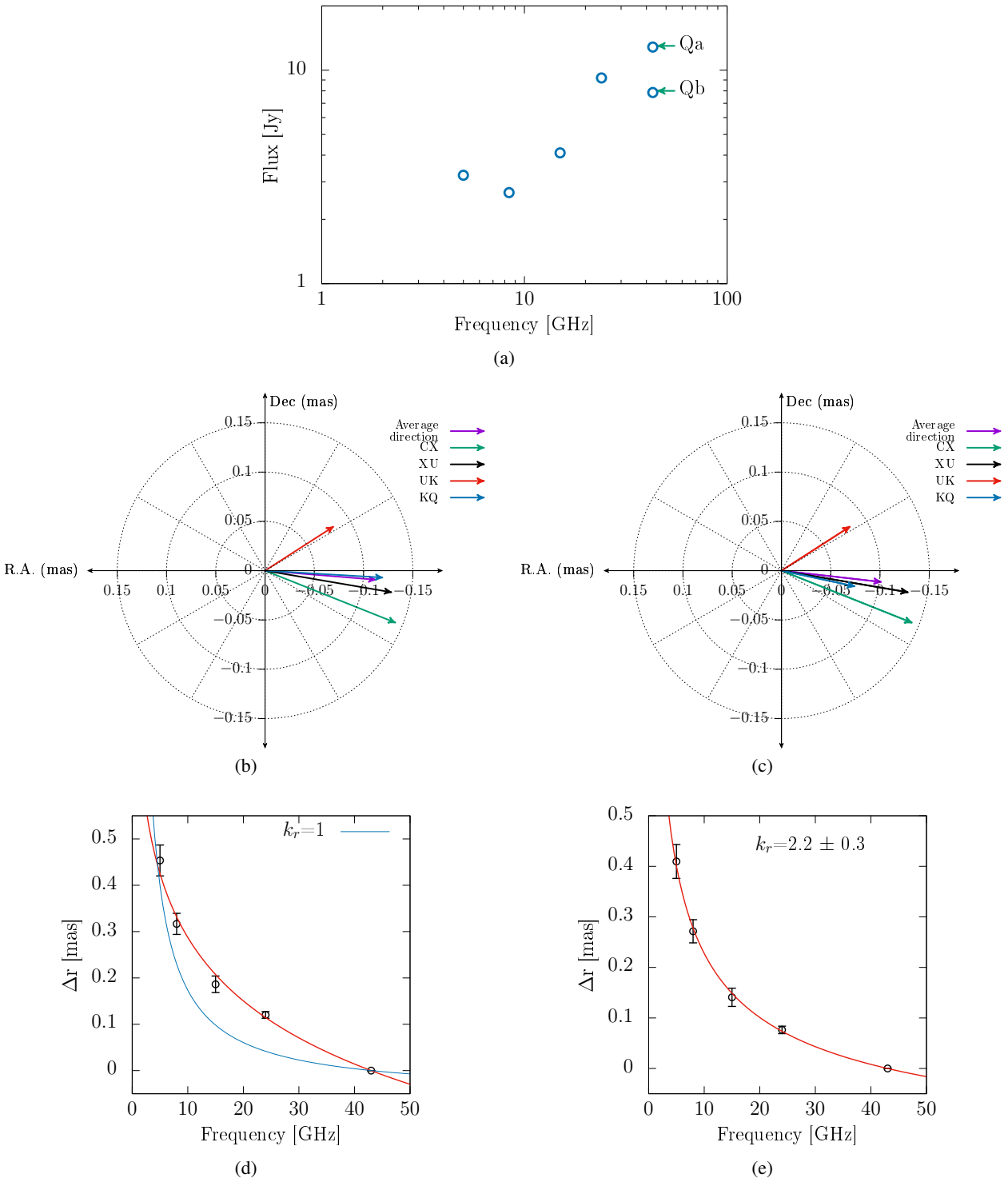


**Fig. D.16.** Epoch 17, 2009 December 03. a) Core spectrum, where Qa represents the core and Qb the feature moving downstream. For comparisons, see Figure 4c. Core-shift vectors of all frequency pairs using b) Qa and c) Qb. Similarly, as in the previous epoch, the two components have a similar impact on the direction of KQ core-shift vector. Power-law fits (red curve) using d) Qa and e) Qb. In this epoch the flare appears to hinder the correct location of the core at the Q-band (43 GHz). This ultimately disrupts the core-shift effect by increasing the core-shift values at the high frequencies, as seen in d). Therefore, this observation is not included in the variability analysis of index $k_r$.

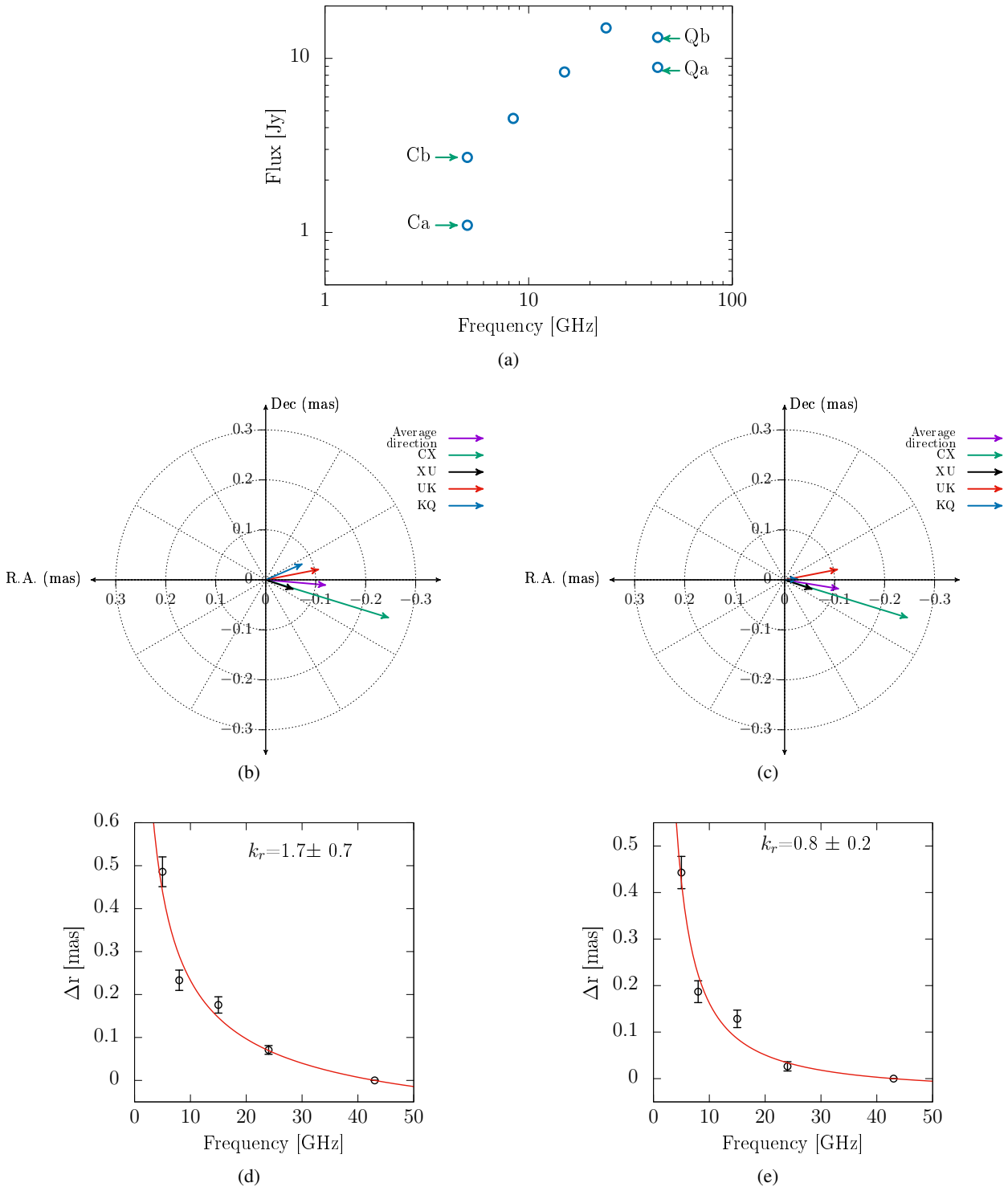


**Fig. D.17.** Epoch 18, 2010 January 18. a) Core spectrum, where Cb and Qa represent the core at the C and Q bands. Qb is the feature moving downstream. For comparisons, see Figure 4d. Core-shift vectors of all frequency pairs using b) Qa and c) Qb. Similarly, as in the previous epoch, the two components have a similar impact on the direction of KQ core-shift vector. Power-law fits (red curve) using d) Qa and e) Qb. Again, the flare appears to hinder the correct location of the core at the Q band (43 GHz). The effect is less pronounced than in the previous epoch, but it disorders the core-shift effect by increasing the core-shift values at the high frequencies, as seen in d).

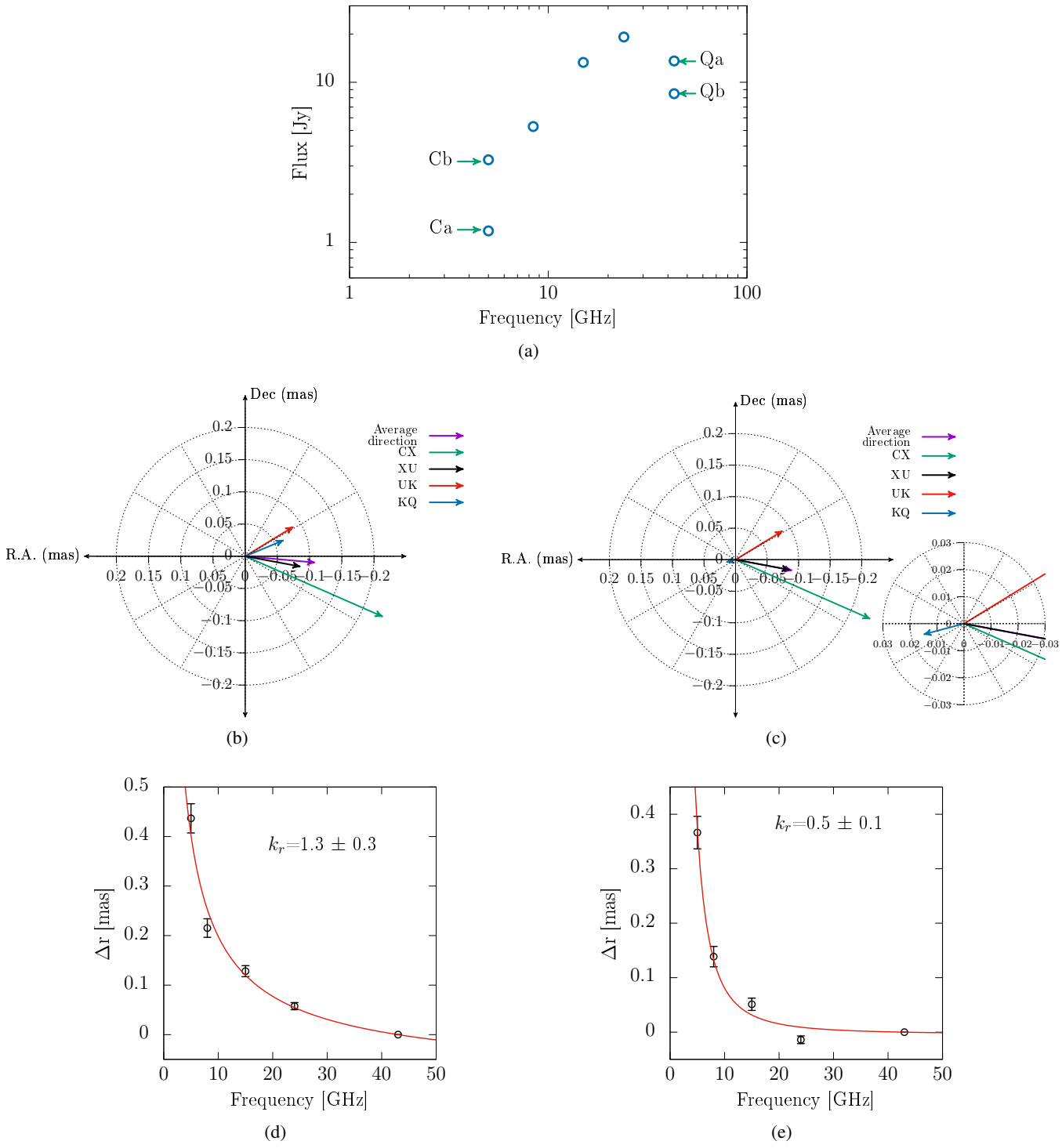


**Fig. D.18.** Epoch 19, 2010 February 21. a) Core spectrum, where Cb and Qa represent the core at the C and Q bands. Qb is the feature moving downstream. For comparisons, see Figure 4e. Core-shift vectors of all frequency pairs using b) Qa and c) Qb. In this epoch it is clear that Qa and Qb have different effects on the KQ core-shift vector direction. The use of Qb leads to the wrong core-shift direction. Power-law fits (red curve) using d) Qa and e) Qb. Similarly, as in previous epochs, the flare appears to affect the location of the core at the Q band (43 GHz). In this observation, the flare effect is less pronounced but increases the core-shift values at the high frequencies, as seen in d).

## Appendix E: VLBA multi-epoch and multi-frequency images

The CLEAN images after self-calibration in amplitudes and in phases are presented here for all epochs. C-band images are displayed in Figures E.1 and E.2, X-band images in Figures E.3 and E.4. For the U band, we present only the epochs not published in the MOJAVE website shown in Figure E.5. K-band images are shown in Figures E.6 and E.7. Finally, Q-band images are displayed in Figures E.8 and E.9.

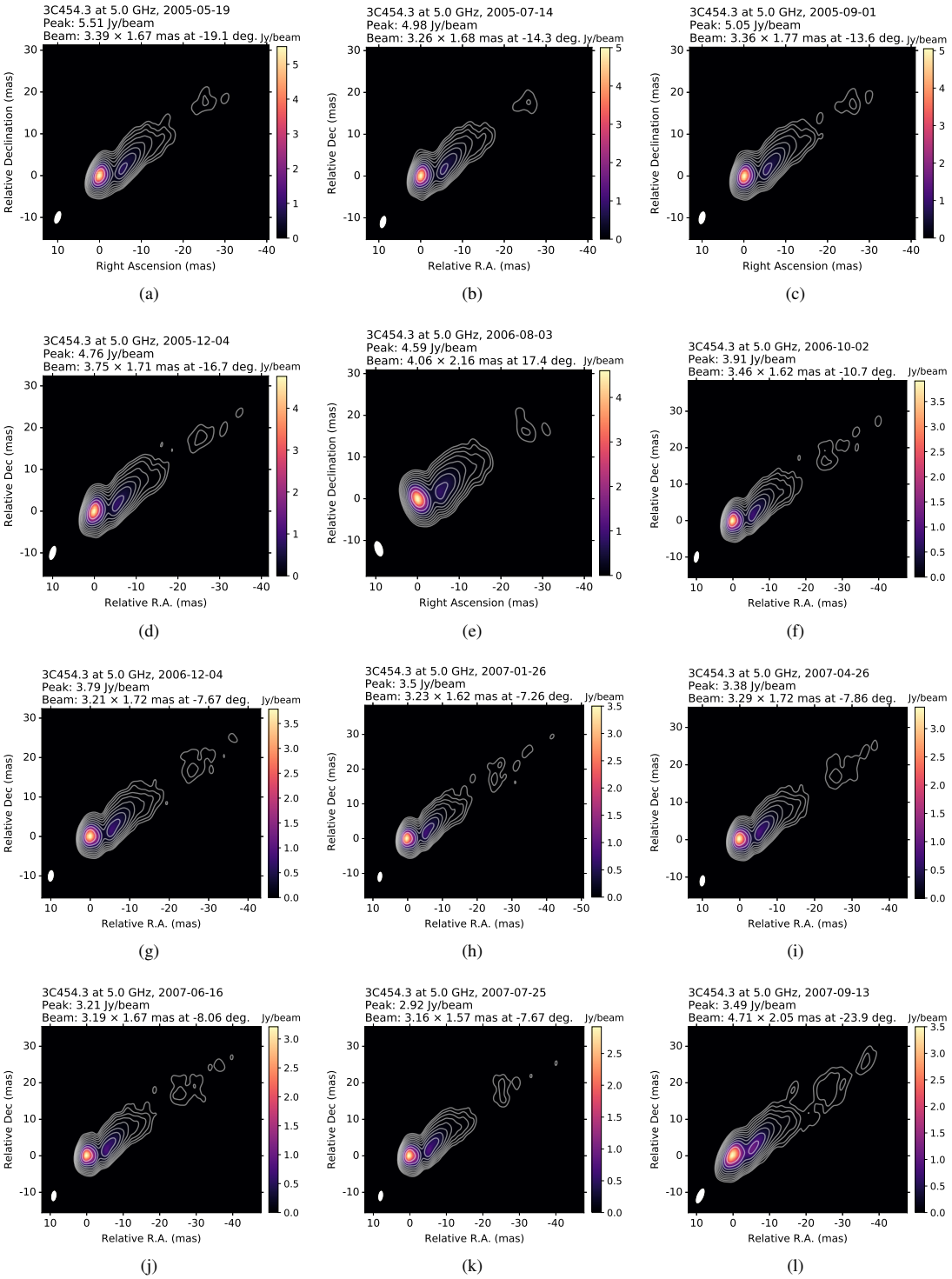


**Fig. E.1.** C-band (5 GHz) CLEAN images of 3C454.3 from 2005 May 19 to 2007 September 13 with contours at -0.1%, 0.1%, 0.2%, 0.4%, 0.8%, 1.6%, 3.2%, 6.4%, 12.8%, 25.6%, and 51.2% of the peak intensity at each image.

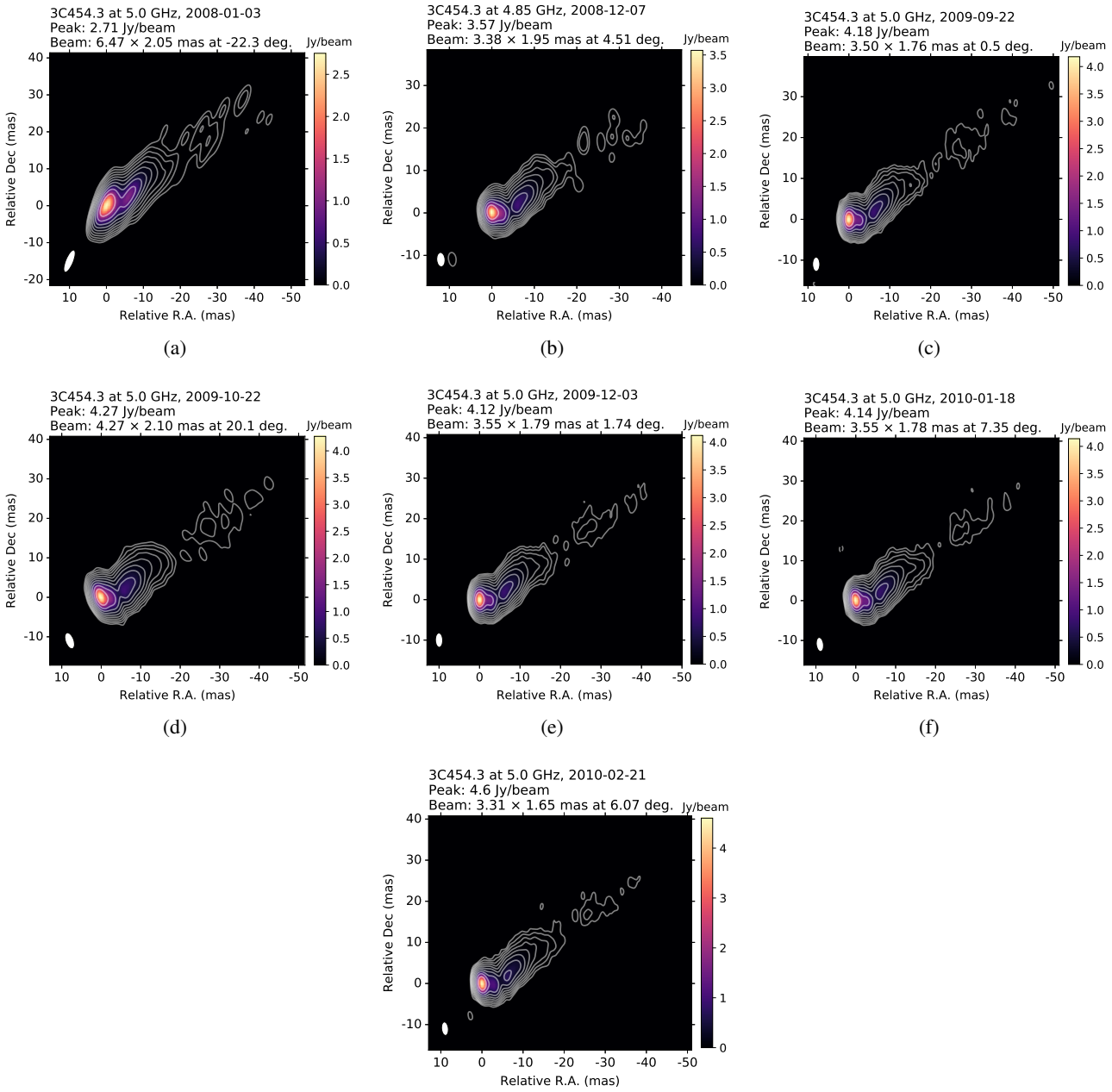


**Fig. E.2.** C-band (5 GHz) CLEAN images of 3C454.3 from 2008 January 03 to 2010 February 21 with contours at -0.1%, 0.1%, 0.2%, 0.4%, 0.8%, 1.6%, 3.2%, 6.4%, 12.8%, 25.6%, and 51.2% of the peak intensity at each image.

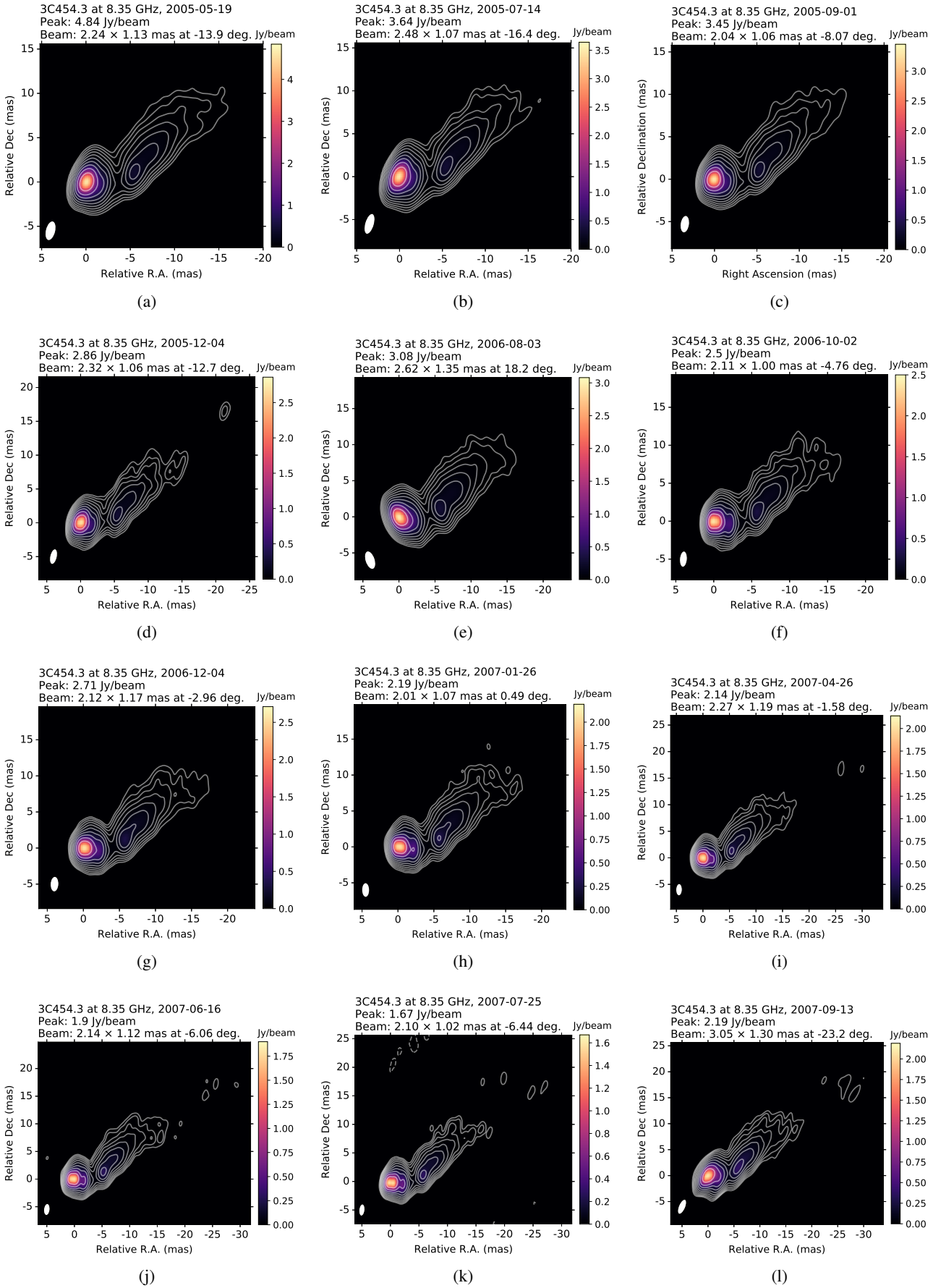


**Fig. E.3.** X-band (8 GHz) CLEAN images of 3C454.3 from 2005 May 19 to 2007 September 13 with contours at -0.1%, 0.1%, 0.2%, 0.4%, 0.8%, 1.6%, 3.2%, 6.4%, 12.8%, 25.6%, and 51.2% of the peak intensity at each image.

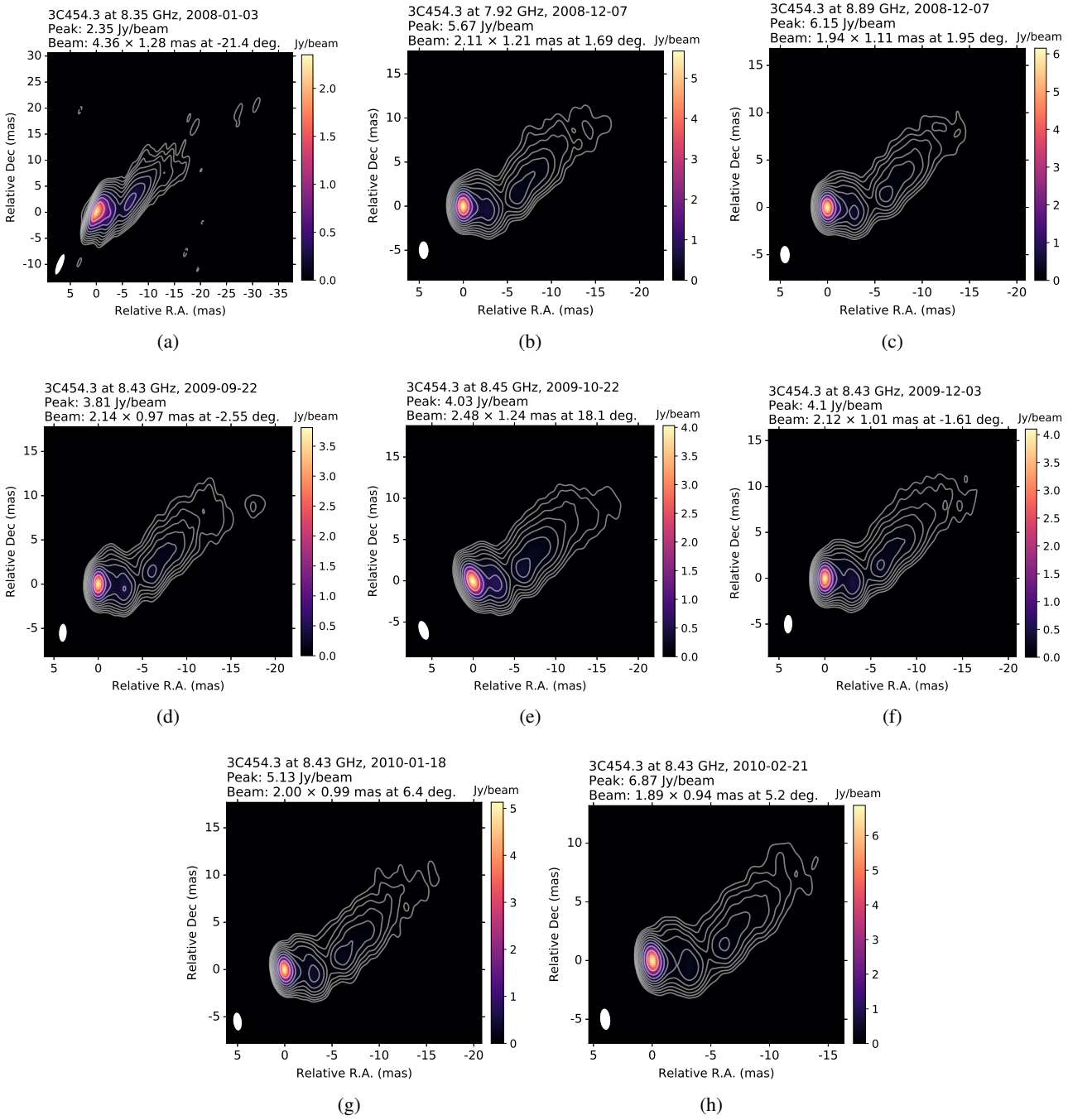


**Fig. E.4.** X-band (8 GHz) CLEAN images of 3C454.3 from 2008 January 03 to 2010 February 21 with contours at -0.1%, 0.1%, 0.2%, 0.4%, 0.8%, 1.6%, 3.2%, 6.4%, 12.8%, 25.6%, and 51.2% of the peak intensity at each image.

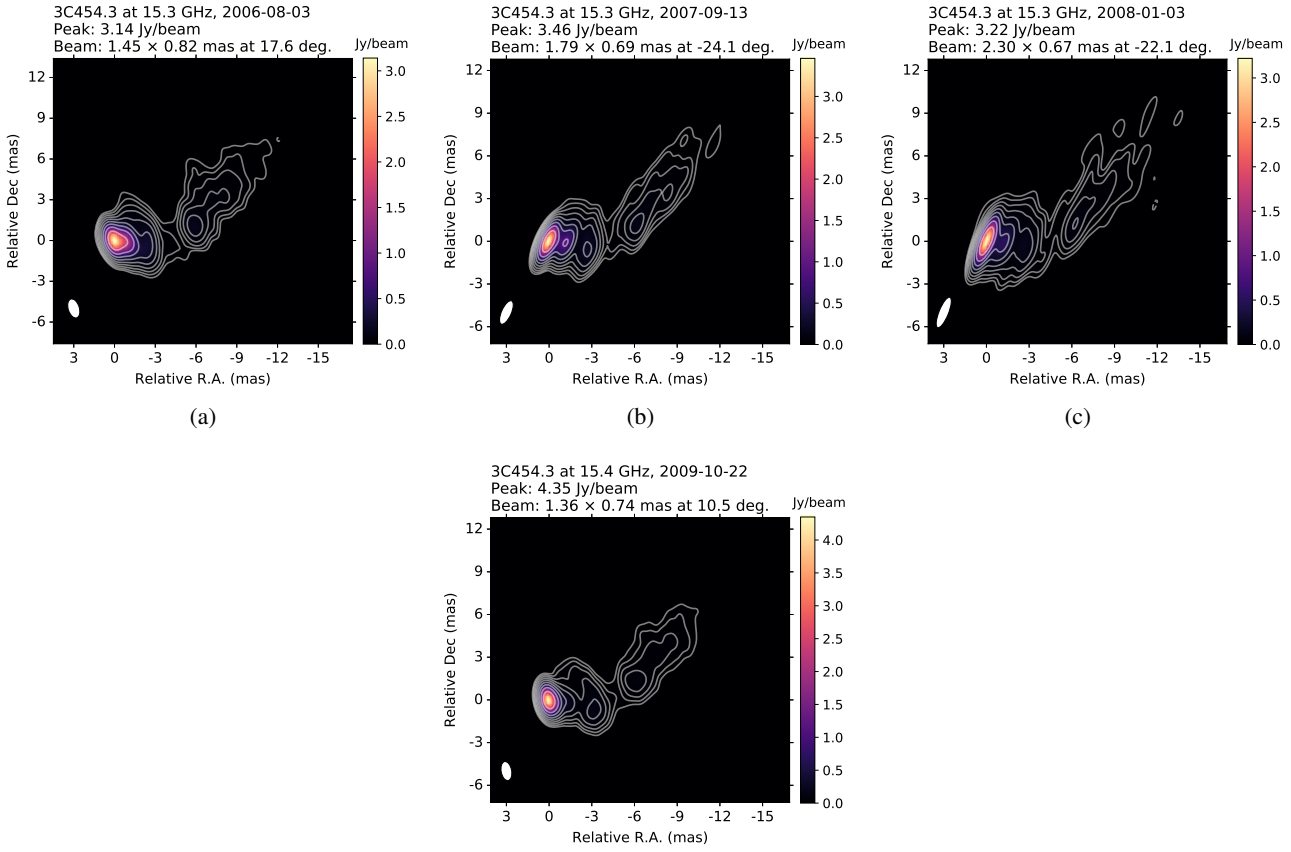


**Fig. E.5.** U-band (15 GHz) CLEAN images of 3C454.3 from 2006 August 03 to 2009 October 22 with contours at -0.2%, 0.2%, 0.4%, 0.8%, 1.6%, 3.2%, 6.4%, 12.8%, 25.6%, and 51.2% of the peak intensity at each image. The missing images for the other epochs have already been published by the MOJAVE team.

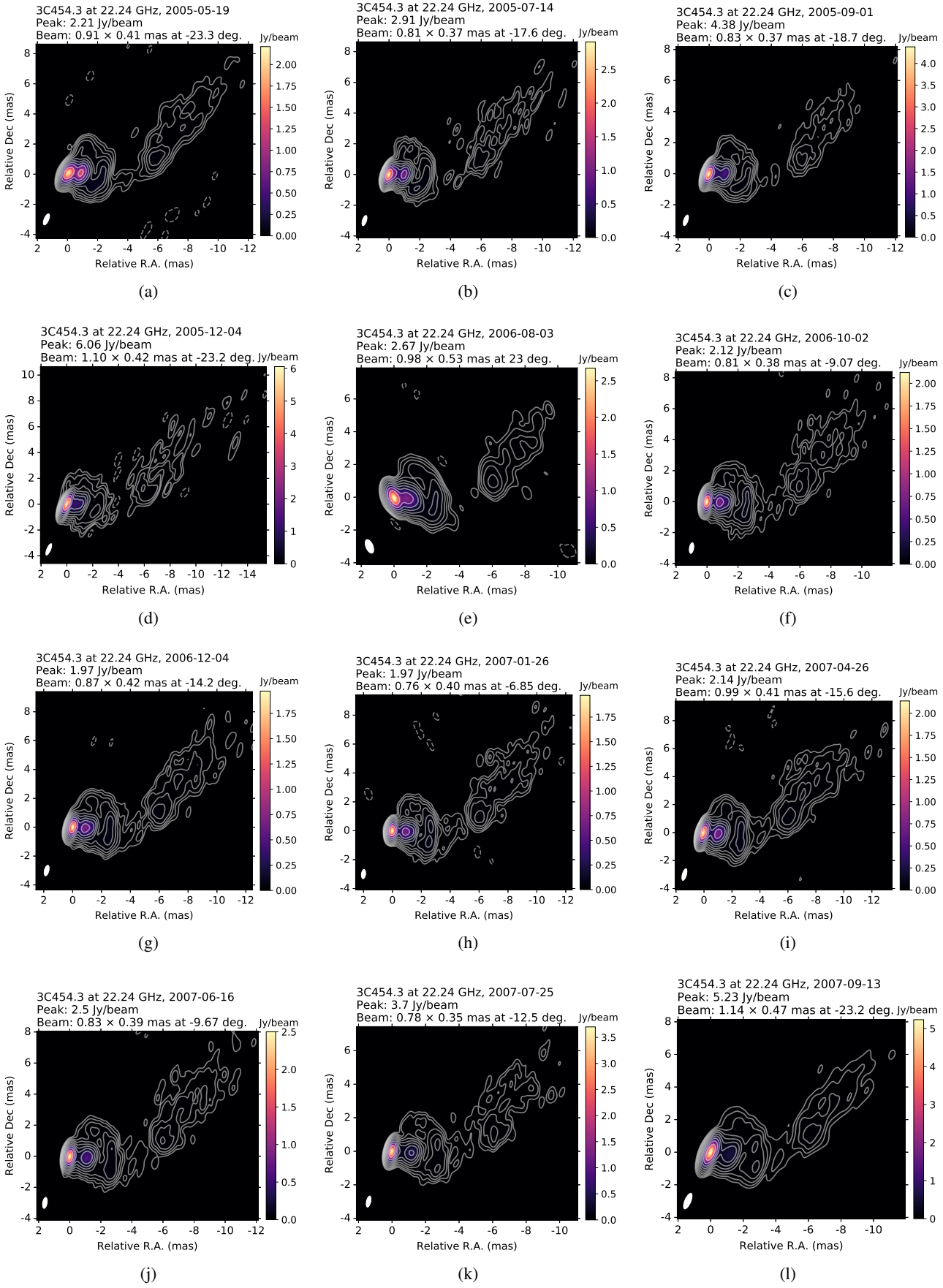


**Fig. E.6.** K-band (22−24 GHz) CLEAN images of 3C454.3 from 2005 May 19 to 2007 September 13 with contours at -0.1%,0.1%, 0.2%, 0.4%, 0.8%, 1.6%, 3.2%, 6.4%, 12.8%, 25.6%, and 51.2% of the peak intensity at each image.

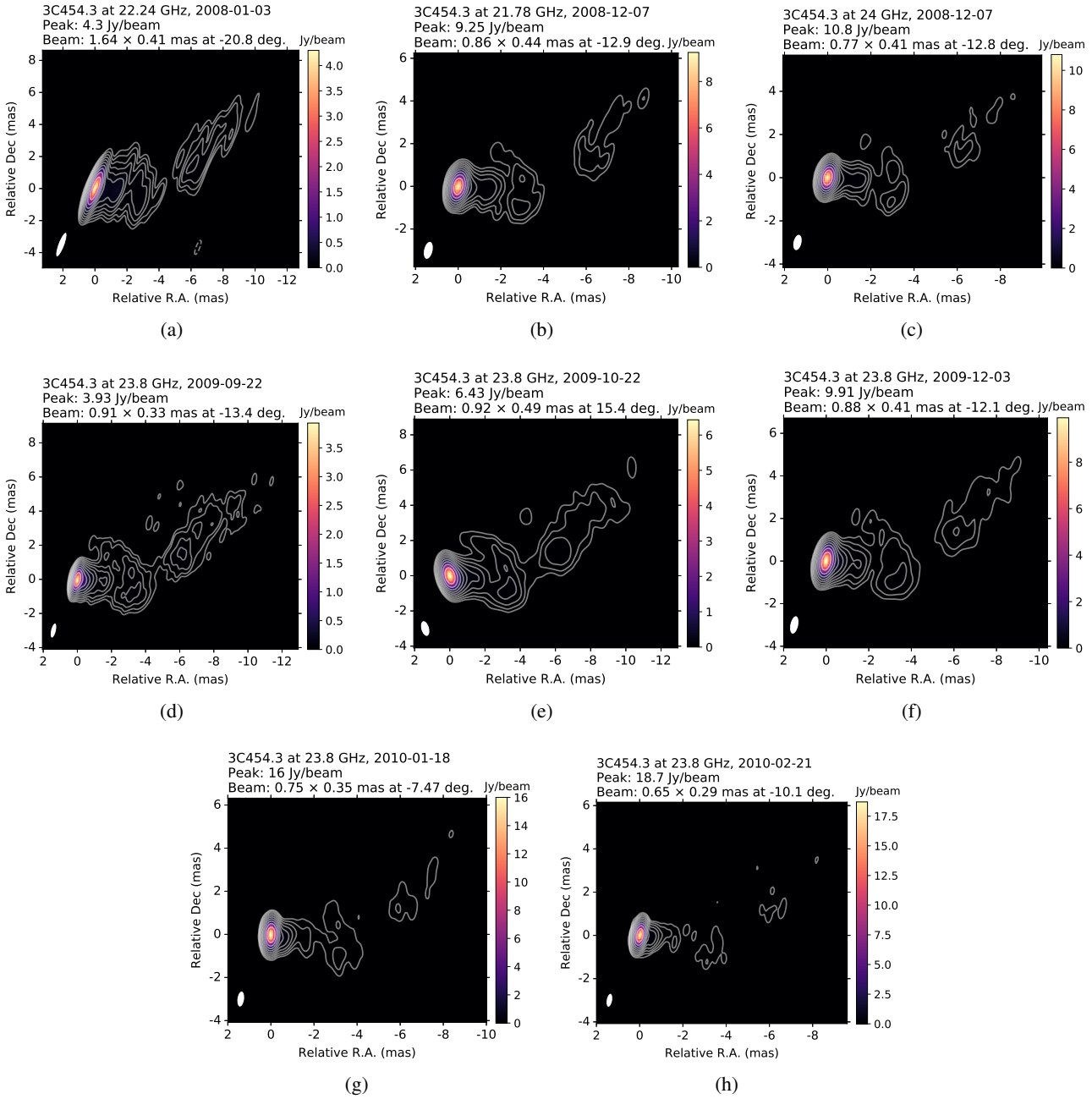


**Fig. E.7.** K-band (22−24 GHz) CLEAN images of 3C454.3 from 2008 January 03 to 2010 February 21 with contours at -0.1%, 0.1%, 0.2%, 0.4%, 0.8%, 1.6%, 3.2%, 6.4%, 12.8%, 25.6%, and 51.2% of the peak intensity at each image.

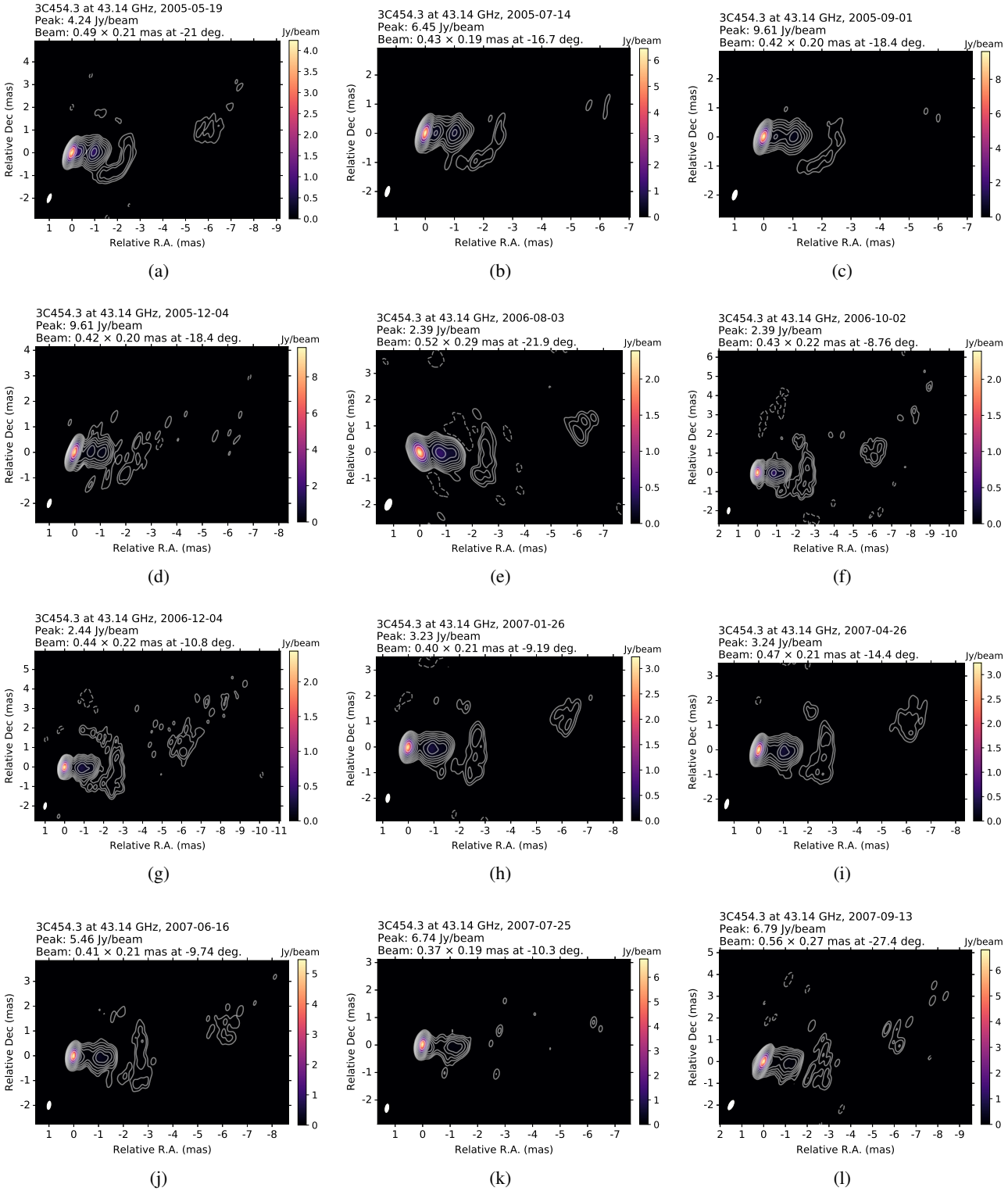


**Fig. E.8.** Q-band (43 GHz) CLEAN images of 3C454.3 from 2005 May 19 to 2007 September 13 with contours at -0.1%, 0.1%, 0.2%, 0.4%, 0.8%, 1.6%, 3.2%, 6.4%, 12.8%, 25.6%, and 51.2% of the peak intensity at each image. For 2007 September 13 the contours are at -0.05%, 0.05%, 0.1%, 0.2%, 0.4%, 0.8%, 1.6%, 3.2%, 6.4%, 12.8%, 25.6%, and 51.2% of the peak intensity.

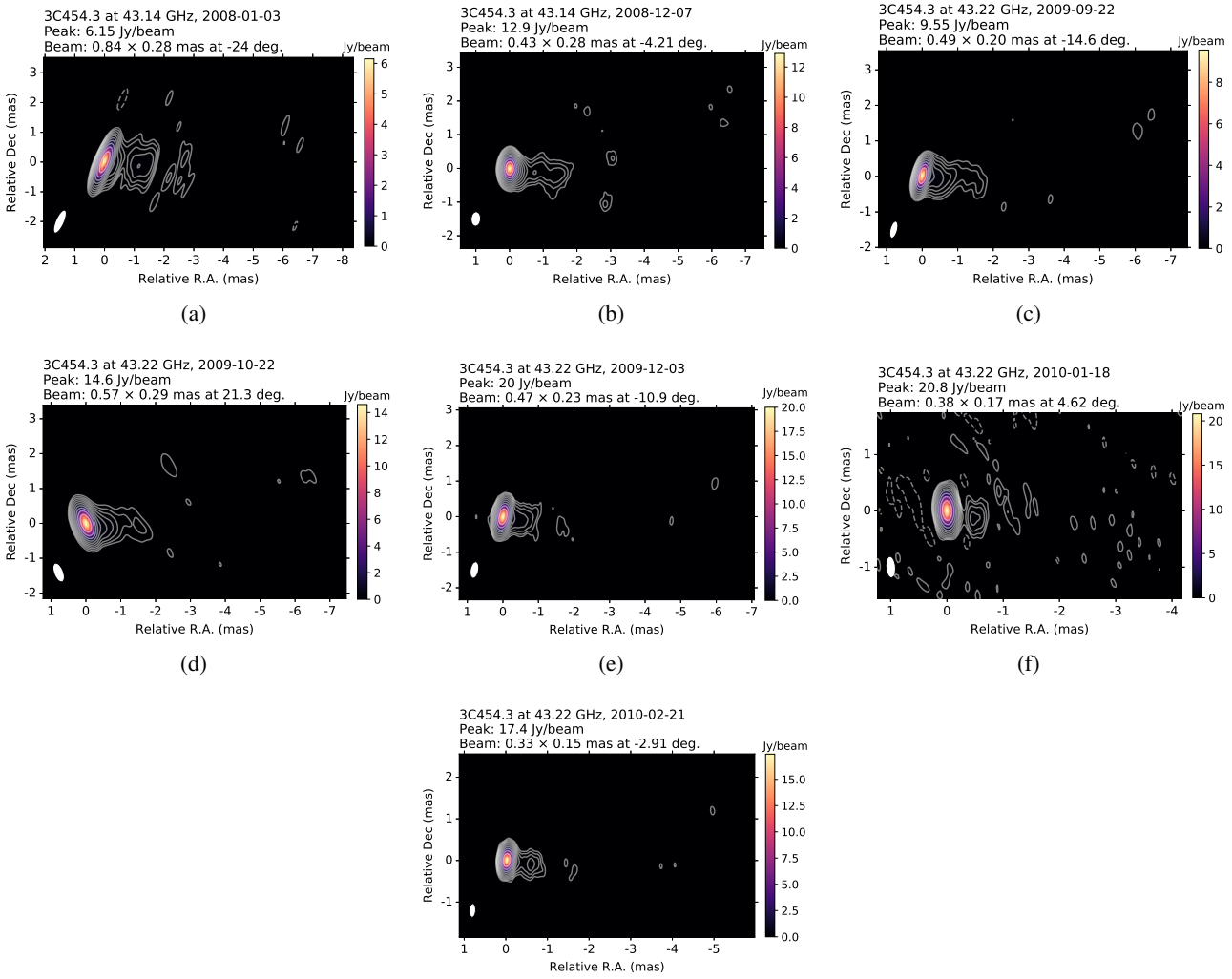


**Fig. E.9.** Q-band (43 GHz) CLEAN images of 3C454.3 from 2008 January 03 to 2010 February 21. The contours are given at -0.1%, 0.1%, 0.2%, 0.4%, 0.8%, 1.6%, 3.2%, 6.4%, 12.8%, 25.6%, and 51.2% of the peak intensity at each image. For 2008 December 7 the contours are at -0.05%, 0.05%, 0.1%, 0.2%, 0.4%, 0.8%, 1.6%, 3.2%, 6.4%, 12.8%, 25.6%, and 51.2% of the peak intensity.

## Appendix F: Spectral index maps

Spectral index maps are obtained after alignment using matched common-uvrange images per frequency pair at all epochs. CX spectral index maps are displayed in Figures F.1 and F.2. XU spectral index maps are displayed in Figures F.3 and F.4. UK spectral index maps are displayed in Figures F.5 and F.6, and KQ spectral index maps are displayed in Figures F.7 and F.8.

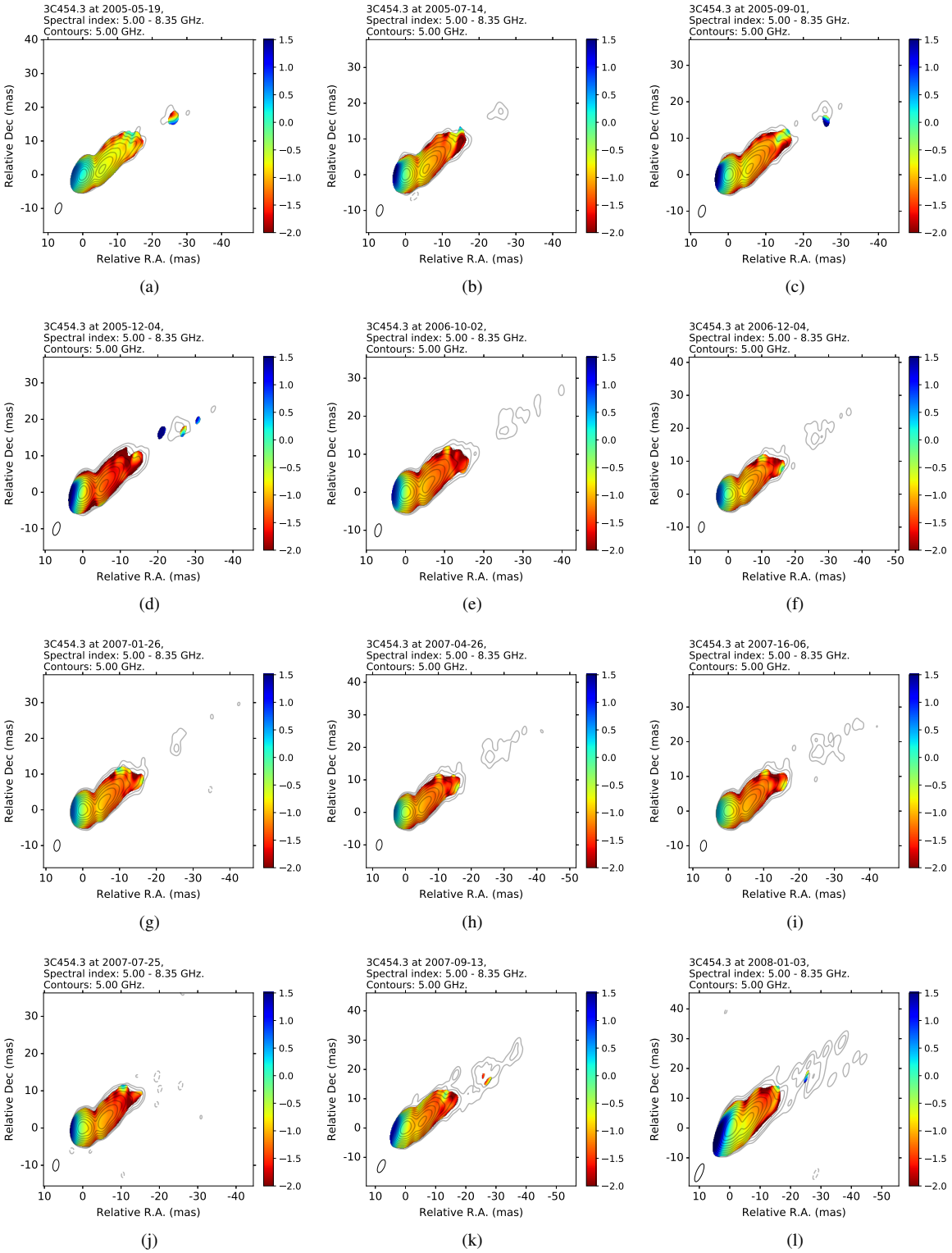


**Fig. F.1.** Spectral index maps for the frequency pair CX (5 - 8 GHz). The colour bar indicates the spectral index. The ellipse in the bottom left corner represents the interferometric beam. The contour lines are given at -0.1%, 0.1% 0.2%, 0.4%, 0.8%, 1.6%, 3.2%, 6.4%, 12.8%, 25.6%, and 51.2% of the peak intensity at each image.

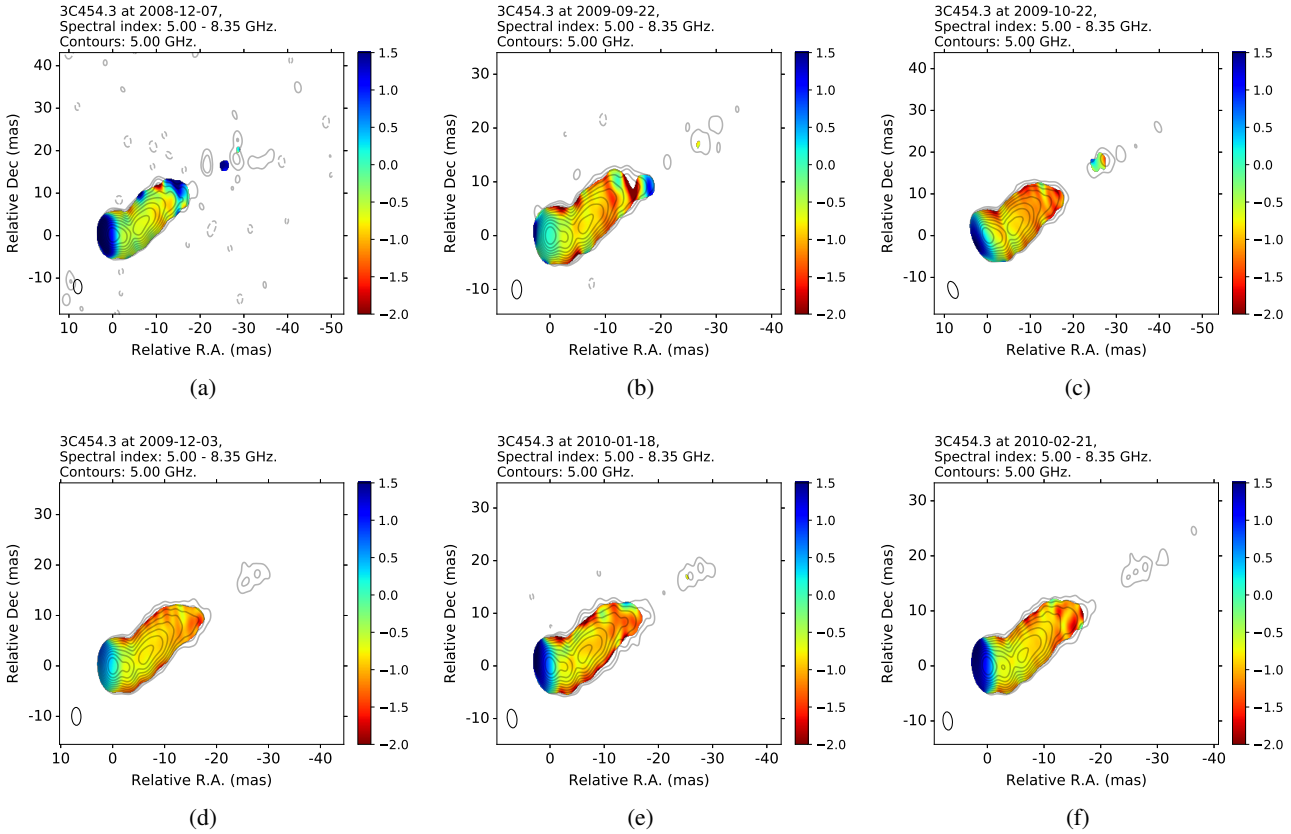


**Fig. F.2.** Continuation of Figure F.1.

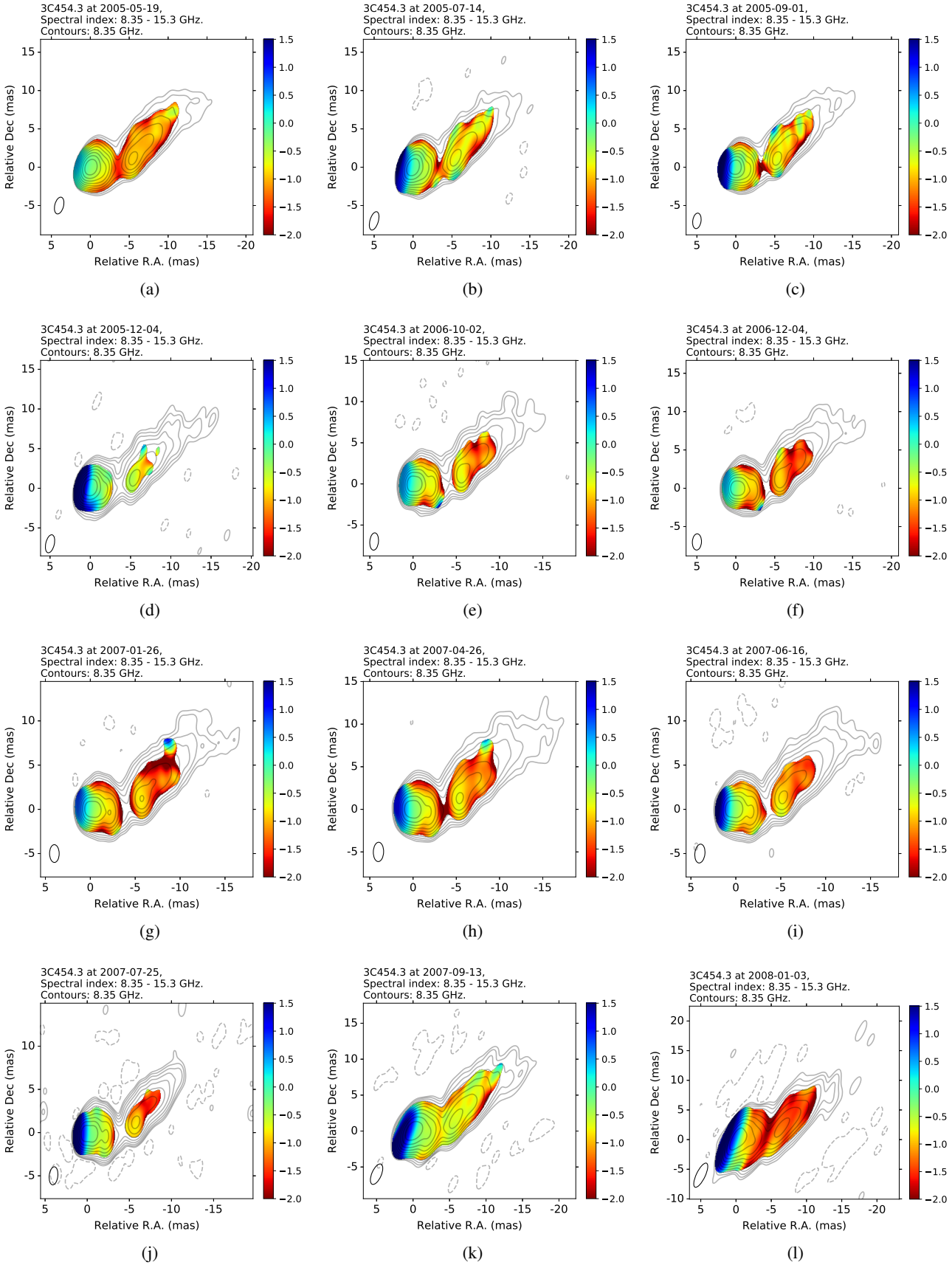


**Fig. F.3.** Spectral index maps for the frequency pair XU (8 - 15 GHz). The colour bar indicates the spectral index. The ellipse in the bottom left corner represents the interferometric beam. The contour lines are given at -0.1%, 0.1% 0.2%, 0.4%, 0.8%, 1.6%, 3.2%, 6.4%, 12.8%, 25.6%, and 51.2% of the peak intensity at each image.

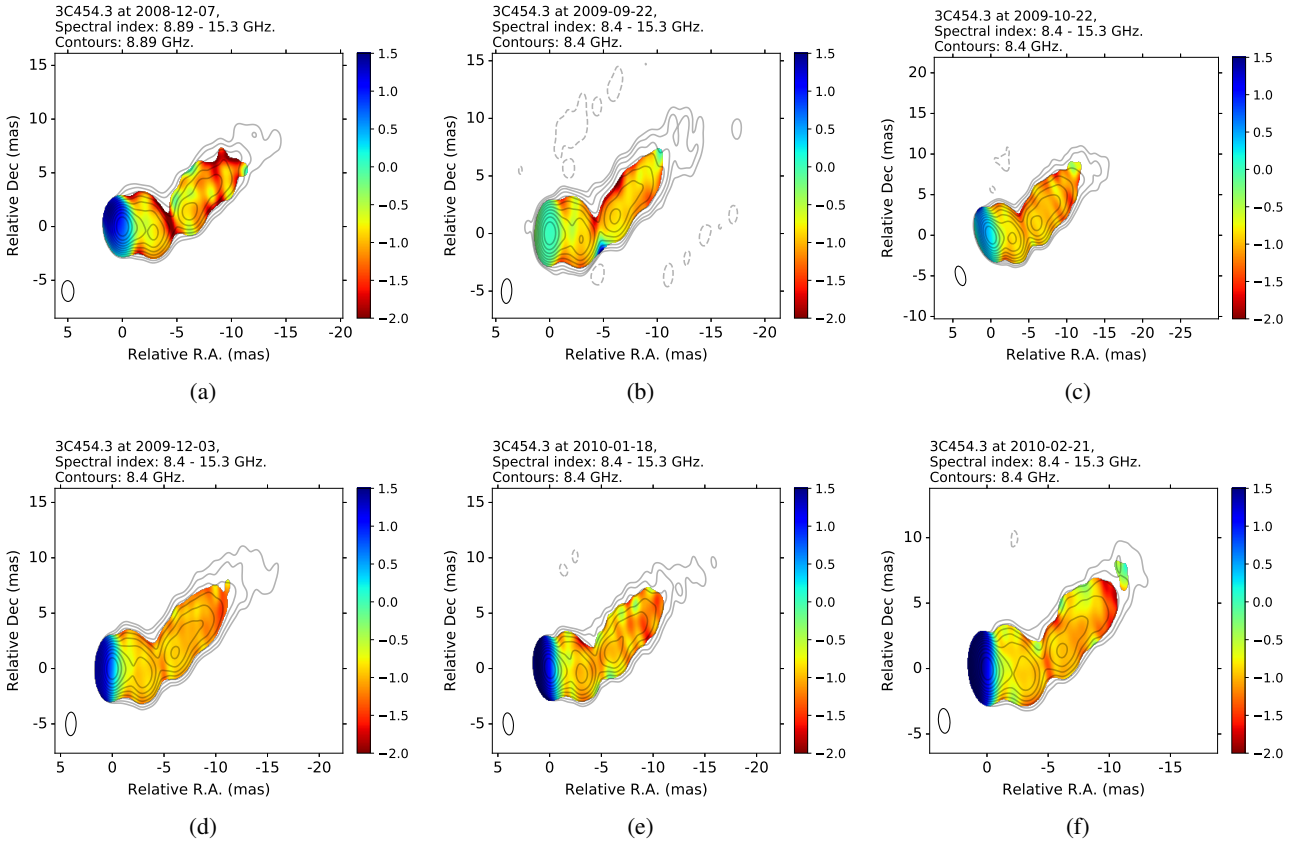


**Fig. F.4.** Continuation of Figure F.3.

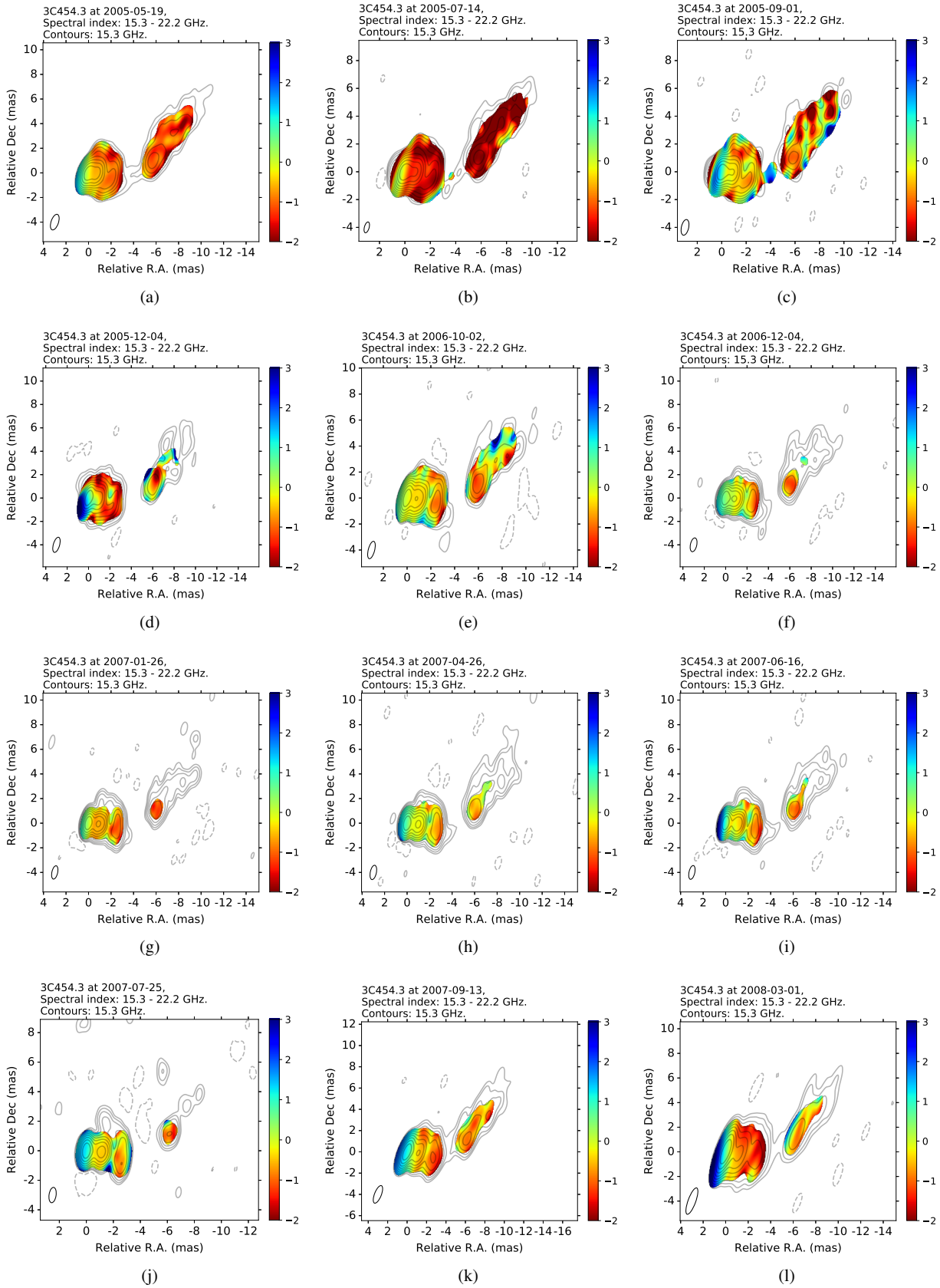


**Fig. F.5.** Spectral index maps for the frequency pair UK (15 − 22) GHz. The colour bar indicates the spectral index. The ellipse in the bottom left corner represents the interferometric beam. The contour lines are given at -0.1%, 0.1% 0.2%, 0.4%, 0.8%, 1.6%, 3.2%, 6.4%, 12.8%, 25.6%, and 51.2% of the peak intensity at each image.

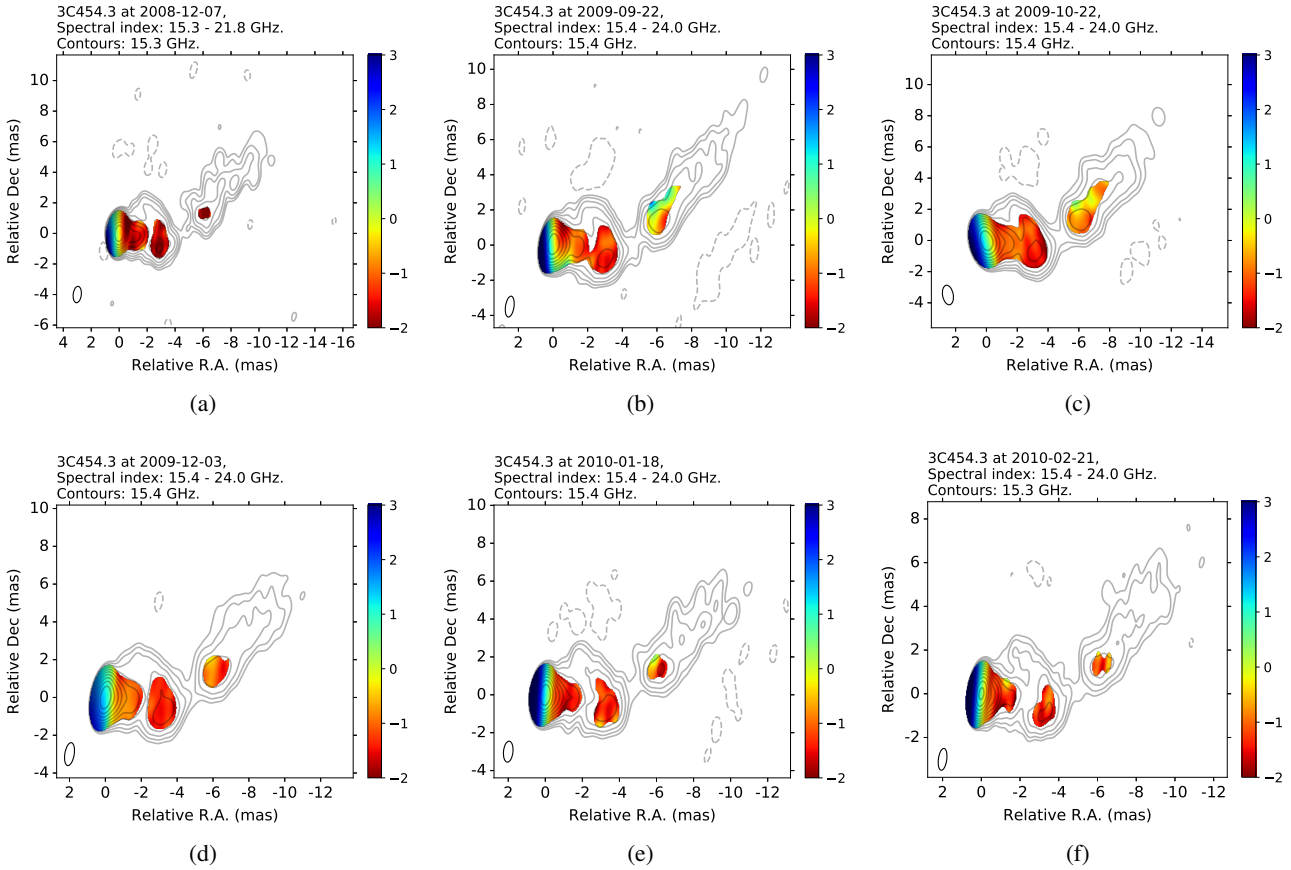


**Fig. F.6.** Continuation of Figure F.5. Spectral index maps for the frequency pair UK (15 − 24) GHz.

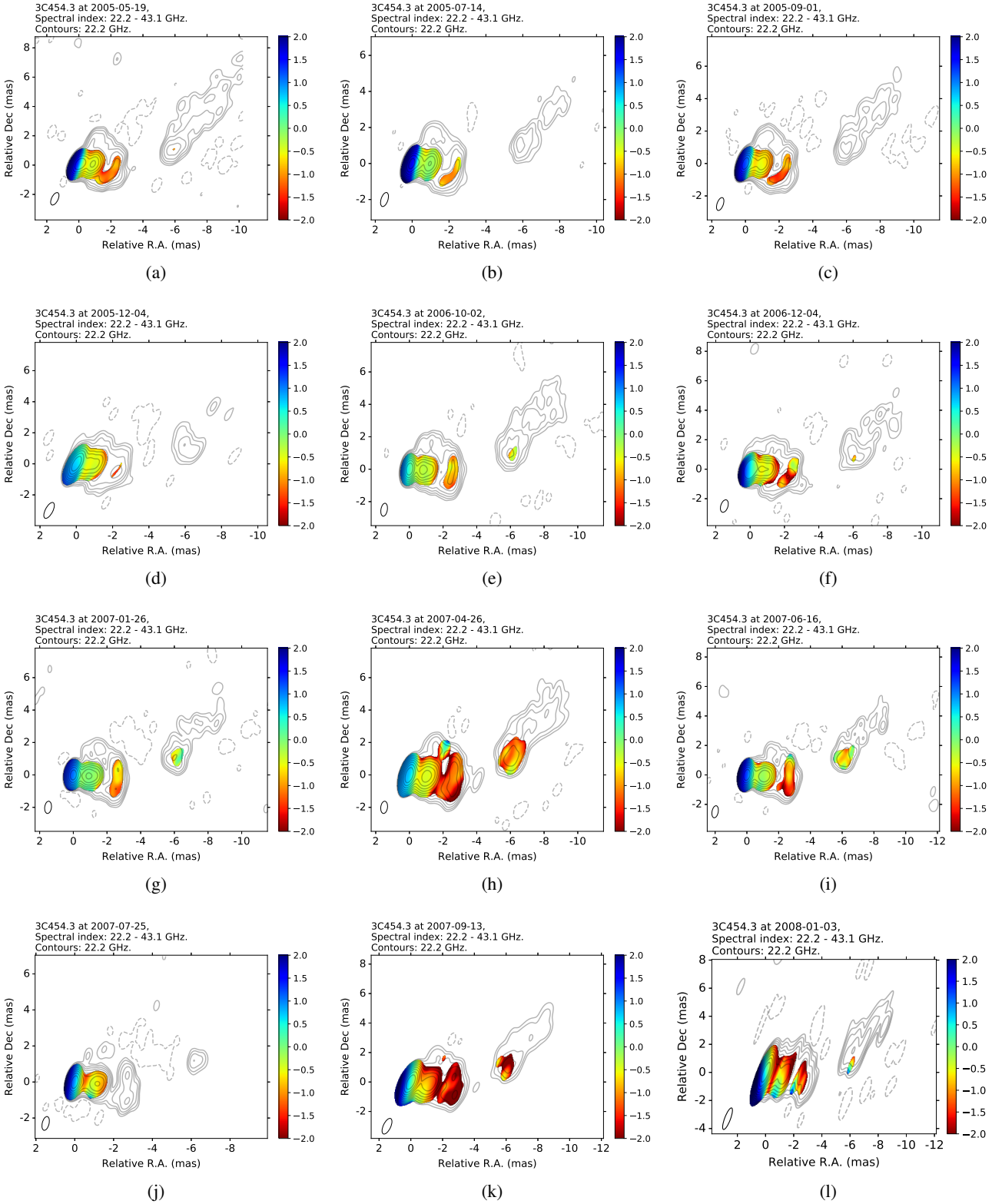


**Fig. F.7.** Spectral index maps for the frequency pair KQ (22−43 GHz). The colour bar indicates the spectral index. The ellipse in the bottom left corner represents the interferometric beam. The contour lines are given at -0.1%, 0.1% 0.2%, 0.4%, 0.8%, 1.6%, 3.2%, 6.4%, 12.8%, 25.6%, and 51.2% of the peak intensity at each image.

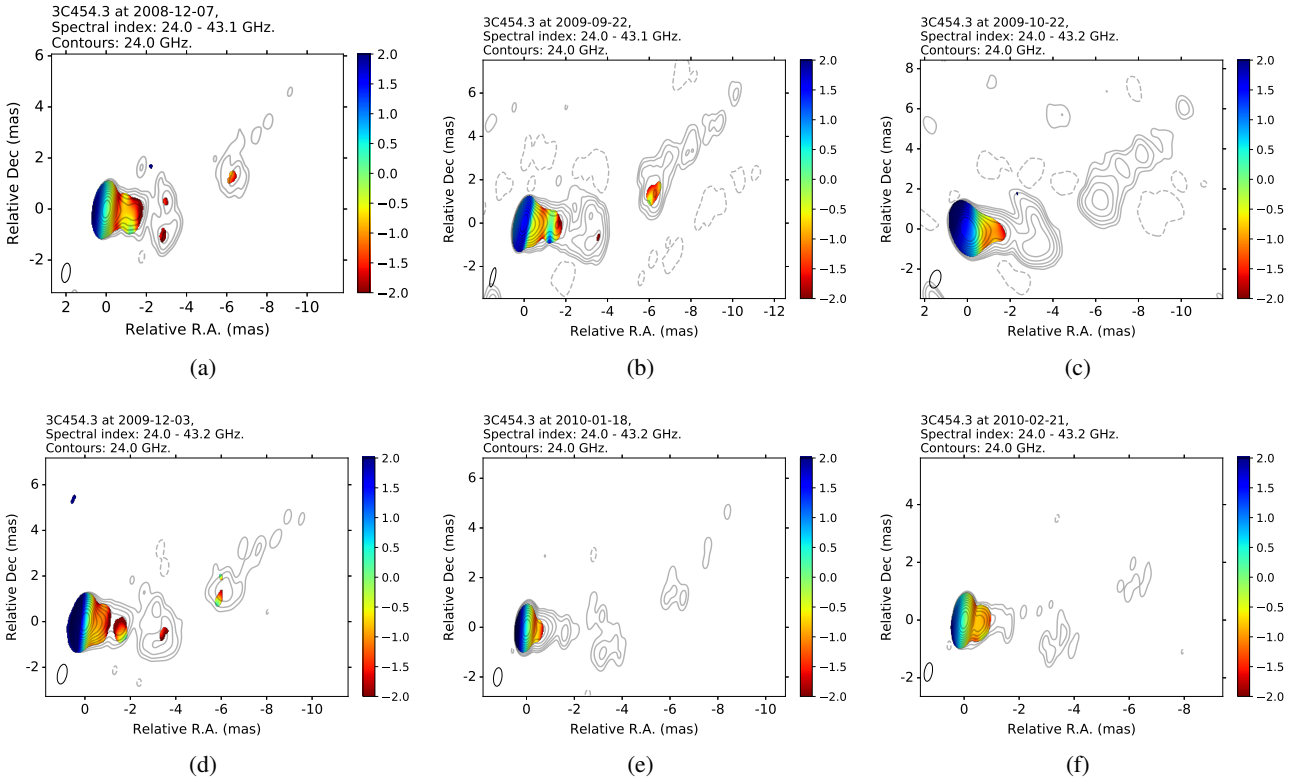


**Fig. F.8.** Continuation of Figure F.7. Spectral index maps for the frequency pair KQ (24−43 GHz).